Phase Dependent Atom Optics

Aline Vernier

Submitted in fulfilment of the requirements
for the Degree of Doctor of Philosophy

Department of Physics & Astronomy
Faculty of Physical Sciences
University of Glasgow

April 23, 2011

Author's declaration

The work described in this Thesis was carried at the University of Glasgow under the supervision of Dr. Sonja Franke-Arnold, Department of Physics and Astronomy, in the period October 2006 to September 2010. The author hereby declares that the work described in this Thesis is her own, except where specic references are made. It has not been submitted in part or in whole to any other university for a degree.

Author's signature:

.....

Aline Vernier
Glasgow, October 2010

Abstract

Quantum interference in atomic media has elicited interest for a very wide range of investigations and applications. As well as being a fascinating effect in itself, it also found applications in spectroscopy, nonlinear optics and has recently been drawing attention in the field of quantum optics for the realisation of sources of entangled photons, optical switching, and quantum information storage.

The work presented in this thesis consists of two main projects centred around the theme of quantum interference in atomic processes. As cooled atomic vapours provide favourable conditions for the investigation of coherent phenomena, a magneto-optical trap was built for the future study of quantum interference in four-level linkages. The number of trapped atoms is estimated to be $\approx 8 \times 10^8$, and the density to be $\approx 10^9$ atoms per cubic centimetre. This represents the first stage of an ongoing study of quantum interference in four-level linkages.

However, coherent effects can also be observed in hot vapours. A spontaneous, highly efficient, frequency up-conversion arising from four-wave mixing can indeed be observed in Rubidium. This complex phenomenon was investigated experimentally and theoretically so as to improve the conversion efficiency, and understand the underlying physics. The optimum conditions found in this study yield 1 mW of converted light for 40 mW of pumping light.

As part of the study of the phase coherence of the process, the conversion of spatial modes in the four-wave mixing process was also examined. The observation of the transfer of orbital angular momentum in the process is reported, and a preliminary theoretical interpretation is presented.

Acknowledgements

First and foremost, I wish to thank my supervisor Sonja Franke-Arnold for embarking on an atom optics project and taking me onboard! Working with you was great fun, and I am grateful for your enthusiasm, as well as your ability to always understand what I mean even when I'm so unclear that I'm not even sure what I mean myself. If you see what I mean... :)

The fascinating work on the blue light would obviously not have been possible without Aidan Arnold, whom I acknowledge for his very own thesis, as a certain file named "ASAThesis.pdf" was undoubtedly my favourite read during these 4 years! Many thanks to Erling Riis for the enlightening atom optics discussions, and for all the guidance in the blue light project in general.

I also wish to acknowledge Ken Strain from IGR for his help with electronics issues.

Miles Padgett's help with laser locking was invaluable. Thanks for the really nice phase sensitive detectors, and also for the outstanding group chemistry which I believe has a lot to do with your bearing with the whole group having lunch in your office every day!

The Optics group was indeed a fun and supportive environment to work in, and there was always someone to give you a hand or lend a friendly ear when things weren't doing so well. The skills I learnt go beyond the physics, as Ken introduced me to the world of science shows and of

outreach, and Jonathan got me to enjoy the combination of bikes and mud. I am very pleased to thank Claire, Laura, Kevin, Steve, Alasdair, John, Lesley, Graham and Johannes who welcomed me so warmly in the group, and Arran, Richard, Jacqui, Chris, Ryan, Maria and Martin, who arrived later, but would have done just the same... Thanks to Daryl and Gail for being around when things were stormy out there.

Alison, Barry, I am infinitely grateful for your kindness and friendship.

Merci infiniment à mon Papa et ma Mémé pour leur soutien inconditionnel, et leur sagesse.

Contents

List of Figures

List of Tables

CHAPTER 1

Introduction

> "For an object to be red is thus for it to emit films of atoms of such a nature that, when those films collide with a [...] perceiver, the object will look red to that perceiver. Now, what kind of atoms constitute films which prompt the perception of red? According to Theophrastus, the answer is 'large, round atoms'. [Tay99]"
>
> — C.C.W. Taylor

1.1 What is atom optics?

In the early ages of natural philosophy, five centuries B.C., Leucippus, his more famous pupil Democritus and the first western school of atomists, attempted to answer the question of what the world is made of

by speculating that matter is made of indivisible corpuscles interacting mechanically, and which movement is allowed by the existence of a void. The elementary corpuscles, or atoms, were thought to be of different shapes and sizes, and could assemble to form larger structures: the substances and materials whose "secondary qualities" (relative to the observer's senses) an observer can perceive. In their view, colour, unlike shape, size, orientation or arrangement, is a secondary quality prompted by "a stimulus constituted by a continuous bombardment of a series of arrays of atoms" [Tay99]. It follows that an atom cannot have any colour, not because they are too small to be perceived, but because "no atom emits films of atoms". Their view on the nature of light as "arrays of atoms" is particularly interesting: Aristotle's theory of light whereby colour arises from the conjunction of rays travelling from the eyes to the object and light emitted by the object [Sam58] was only refuted in the X$^{\text{th}}$ century. Around 965 A.D., Alhazen proposed that some bodies could shine by themselves, but that opaque and transparent bodies had the power to receive light, and respectively reflect and refract it. He also rejected the existence of rays travelling from the eye of the observer [Sam75].

Newton's investigation of chromatic dispersion in prisms (1704) for the study of light, and Dalton's table of the ultimate particles and their relative weights (1805) proved crucial to the birth of spectroscopy, and indeed the study of light-matter interaction beyond mere refraction and reflection.

In 1814 Fraunhofer ascribed the origin of the dark lines in the Sun's spectrum to absorption of some wavelengths in the Sun's colder atmosphere. Although these dark bands had been observed by Wollaston before him, Fraunhofer was the first to perform absolute wavelength measurement of the spectral lines of different planet and stars. Atom optics as such could be attributed to Kirchhoff and Bunsen who interpreted Fraunhofer's study arguing that each element and compound had its unique spectrum [Lab10] (1859).

The discovery of the electronic structure of the atom in the first decade of the twentieth century, marked by the publication of Bohr's model of the atom in 1913 [Boh13], and the parallel development of the theory of quanta initiated by Planck [Pla14], were the precursors of a scientific revolution. The theoretical works of Schrödinger and Heisenberg laid the mathematical foundations of quantum mechanics which introduced some element of indeterminism in the description of physical processes. Schrödinger proposed an undulatory model of the internal states of atoms and molecules as vectors of complex numbers called wavefunctions [Sch26] which do not represent observable quantities (e.g. position, momentum) but the probability amplitude of these quantities. This description, as well as Heisenberg's which is mathematically different but physically equivalent, has been central to the work on atom-field interaction for the past 100 years.

Coherence is a property of waves that is fairly common for mechanical waves (a pure A from a tuning fork, or the waves created from throwing a

stone in water), but that is unusual for optical waves. The coherence time of an optical wave is measured by the inverse of its frequency spread, so a purely single-frequency wave $E = E_0 e^{i\omega t}$ (zero frequency spread) has a coherence length that tends to infinity, which results in a constant intensity output $I = E^* E = |E_0|^2$. The opposite case, i.e. a random sum of various frequencies across the whole spectrum results in an aperiodic intensity output whose coherence time tends to zero. The concept of coherence is meaningful for all waves, and in particular for the wavefunctions describing atomic quantum behaviour. As we shall see, the coherence of atomic excitations is central to the work presented in this thesis.

Most optical phenomena occurring in nature (with the exception of laser-like emission on Mars and Venus [MBC+81]) stem from the interaction of the medium with incoherent light. The absorption of red and blue by chlorophyll giving the lush greenness of the Scottish countryside, Rayleigh scattering making the sky blue, refraction in water droplets producing rainbows, even the interference effects in the feathers of the magpie or the shell of the beetle, all result from the incoherent interaction of matter with sunlight. The first observation of a coherent light-induced effect in an atomic medium was that of stimulated emission encountered unintentionally in the spectrum of hydrogen by W. E. Lamb and R. C. Retherford in 1947 in their experiment on the Lamb shift [WLR50]. In 1955 J. P. Gordon, H. J. Zeiger, and C. H. Townes engineered an experiment for the amplification of stimulated emission at the frequency of 24 GHz in ammonia molecules,

effectively building the first Microwave laser (MASER) [GZT55].

The generation of intense, collimated and monochromatic (i.e. coherent) optical wavelength radiation with the first lasers dramatically extended the possibilities of exploration of the internal states of matter. Atom optics is one of the many areas of science that benefited from the availability of laser sources. Indeed, the subsequent discovery of coherent effects in atoms was only made possible by the existence of coherent optical radiation.

1.2 Phase-dependent atom optics

The wave nature of the atomic internal states implies the existence of a phase associated with atomic excitation. Phase is however only meaningful relative to a reference, and can only affect atomic behaviour in particular circumstances that this section describes at a basic level.

1.2.1 The two-level atom

Understanding light-atom interaction starts with a two-level atom with dipole moment d and upper state energy $\hbar\omega$, resonantly driven by an electric field $E(t) = E_0 e^{i\omega t}$. It can be derived from the time dependent Schrödinger equation that in the absence of spontaneous decay or collisions the system behaves as a simple harmonic oscillator: the probability for the system to occupy its excited state oscillates with the frequency $\Omega = dE_0/\hbar$ called the Rabi frequency (Figure 1.1).

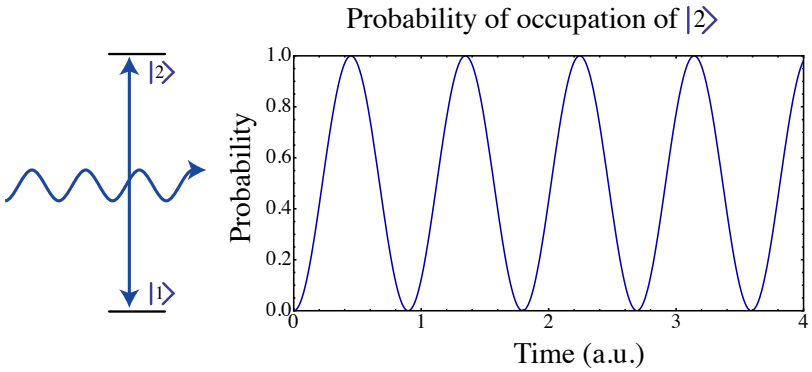

Figure 1.1: Undamped Rabi oscillations of the two-level atom.

The undamped model shows a purely coherent behaviour that gets washed out to an average value when the spontaneous decay γ is introduced (Figure 1.2). This approximation is correct in the limit $\Omega \gg \gamma$, or $E_0 \gg \frac{\hbar\Omega}{d}$, that is thus called the strong coupling regime. This regime is particularly important for the study of atomic coherent behaviour. For a clear derivation and helpful qualitative discussions, see Ref. [Ste05].

The population of the states does not however give the full description of the coupled atom and field. It is clear that there is a qualitative difference between the two states marked by a plus on Figure 1.2 though they exhibit the same upper state population. This difference is quantified by what is called the coherence between the two states and is a measure of the susceptibility χ of the transition. χ is a complex number whose real and imaginary parts correspond respectively to the refractive index and to the absorption/gain.

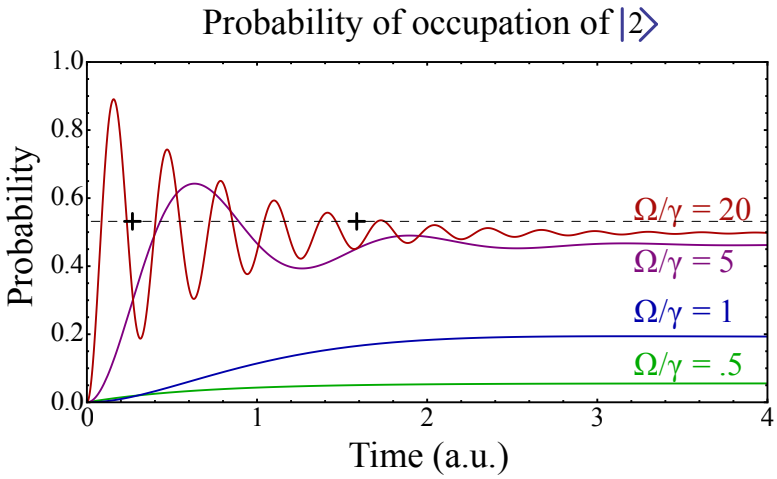

Figure 1.2: Rabi oscillations of the two-level atom: driving an atom with a coherent field gives rise to oscillations of the atomic population from the ground state to the excited state and back. The frequency of these oscillations is proportional to the amplitude of the excitation field and the dipole moment of the transition.They are damped by spontaneous decay and like mechanical oscillators, they can be overdamped (green), critically damped (blue) and underdamped (purple, red).

The refractive index of a single atom is not easy to picture, and considering an atomic vapour instead is useful: in the presence of the atomic medium, the field can be written as $E(t) = E_0 e^{-i(nkz-\omega t)}$, with $n = 1 + \chi$. n can be decomposed into its real and imaginary parts. This yields $E(t) = E_0 e^{-\Im(n)kz} e^{-i(\Re(n)kz-\omega t)}$ where the role of the imaginary part as a decay/gain in the medium and that of the real part as refraction is obvious.

For two levels it is clear that the phase of the light itself plays no role whatsoever in the behaviour of the atom. In that sense, the two-level atom differs

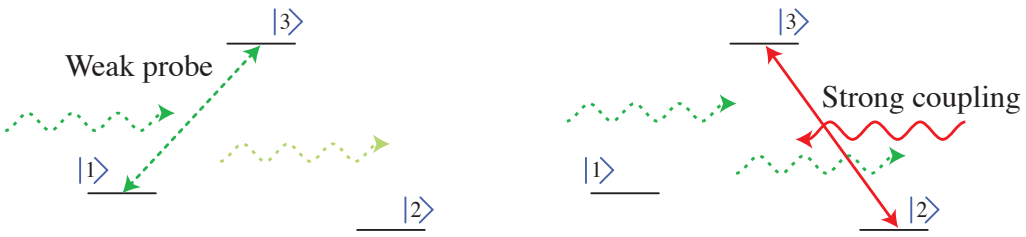

a) Absorption of a weak probe b) Inhibition of the absorption by EIT

Figure 1.3: Driving scheme for Electromagnetically Induced Transparency. a) A resonant weak probe is absorbed by an atom in the ground state. b) The absorption of resonant light can be inhibited by the presence of a coupling strong field.

greatly from a forced mechanical oscillator whose position as a function of time depends on the phase of the driving force.

1.2.2 Beyond the two-level atom

Driving two transitions simultaneously, according to the scheme shown in Figure 1.3 gives rise to a phenomenon called Electromagnetically Induced Transparency (EIT) [BIH91, FHH91] whereby the absorption of a weak field resonant with the $|1\rangle \rightarrow |3\rangle$ transition can be inhibited by a strong coupling of levels $|3\rangle$ with $|2\rangle$. This effect is counterintuitive if the atomic levels and the field are considered to be independent. Although this assumption is realistic in the case of a weak field, increasing the Rabi frequency above the decay rate results in a shift of the atomic energy levels. This shift is

accompanied in the case of EIT by the inhibition of the absorption and the enhancement of the nonlinear susceptibility of the medium due to quantum interference. This will be returned to later in this chapter.

Nonlinear susceptibility $\chi^{(n)}$ is central to phenomena such as second harmonic generation, sum-frequency generation ($\chi^{(2)}$) or four-wave mixing ($\chi^{(3)}$), which as well as being interesting for their own sake are also technologically relevant since they can lead to the generation of coherent light at high frequency. Large $\chi^{(n)}$ are commonly found in atomic media near resonance where the absorption of the driving fields is also large, which limits the efficiency of the nonlinear process. It is thus the coexistence of the transparency and the large nonlinear susceptibility that makes EIT interesting. The experimental demonstration of the enhancement of nonlinear phenomena by EIT is reported in Refs. [BBG+04, JXY+96, BHTW96]. Another property that arises from EIT is what is referred to as "slow light", characterised by a very low group velocity of the light in the medium. L. Vestergaard Hau's group observed light group velocities down to 17 m/s [HHDB99], and halted pulses of light in a gas of ultra cold atoms [LDBH01]. Work on EIT was pioneered by K. Boller, S. Harris and A. Imamoğlu in an optically opaque Strontium vapour [BIH91] and aroused a lot of interest for optical switching and for light storage in atomic vapours [PFM+01] using slow light. For a review of the underlying physics of EIT and its applications see Refs. [FIM05, Har97, Luk03].

The observation of EIT or slow light does not depend on the relative phase

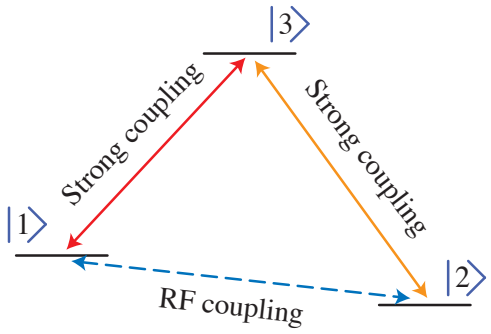

Figure 1.4: Three-level closed loop.

of the two driving lasers, however it was shown in Ref. [BBK+86] that cyclically coupling a three level atom (see Figure 1.4) results in a time-dependent level occupation that depends on the relative phase of the three driving fields $\Phi = \phi_{12} - \phi_{13} - \phi_{32}$. In practice, such three-level linkages were studied using two non-degenerate hyperfine magnetic sub-levels as ground states $|1\rangle$ and $|2\rangle$ coupled together by a radio frequency, and driven to an excited state $|3\rangle$ with an optical field [SH90, oA07].

1.2.3 Phase dependence in a four-level link

Just like three-level loops, four-level linkages exhibit behaviours which depend on the phase of the driving fields. The phase dependence of the occupancy of the upper excited state of a four-level linkage was shown theoretically in 1886 by Buckle et al. [BBK+86]. This behaviour was observed experimentally in 1999, in a Sodium vapour by Korsunsky et

al. [KLH+99, HKW02]. Very recently, in August 2010, the observation of phase-dependent population dynamics was observed in the pulsed regime by Weinacht et al. [CW10].

An interesting theoretical result is that of G. Morigi et al. [MFAO02], who showed that in a simplified case the transfer of population from ground to excited state follows the simple relationship: $P_{1\to4} \propto \cos^2(\Phi)$. This result illustrates that some level of understanding of quantum interference can be gained by comparing the two paths leading from the ground to the excited state to the two paths of a Mach-Zehnder interferometer (Figure 1.5): provided the two paths are indistinguishable, they result in interference. An equivalent way of interpreting the effect is to consider excitation of the atom as an oscillation of the electron to which a probability amplitude is associated. In the presence of two paths, two probability amplitudes have to be added to describe the electronic excitation. If those two probability amplitudes are out of phase, they cancel out, thus inhibiting the excitation. Conversely, when the two probability amplitudes are in phase, they interfere constructively, which enhances the transfer of population to the upper state $|4\rangle$.

1.3 The work in this thesis

Quantum interference in atomic media has elicited interest for a very wide range of investigations and applications involving the control of the absorp-

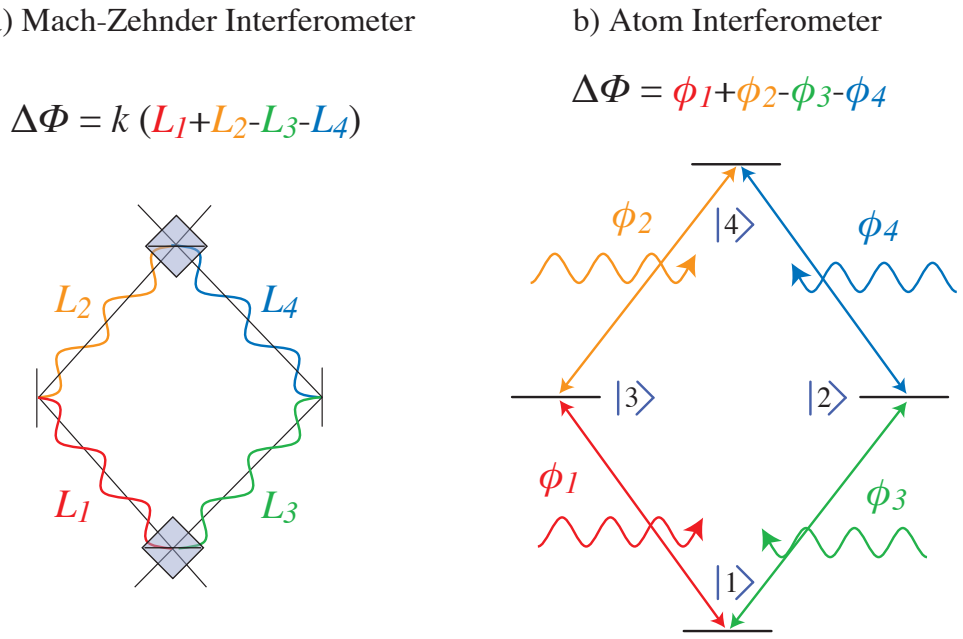

Figure 1.5: Quantum interference in a four-level atom: the two paths the atom can take on the way to the upper state can be assimilated to the two interfering paths of a Mach-Zehnder interferometer. a) In a Mach-Zehnder interferometer, the output is determined by the phase difference between the two paths. b) In an atom interferometer, the probability of excitation is determined by the difference between the phases of the two excitation paths.

tive and refractive properties of atoms. It found several applications soon after its discovery, notably in spectroscopy [ZS96, LFZ+97] and nonlinear optics [Scu91, LHL+98]. Recently, it has been drawing particular attention in the field of quantum optics for the realisation of sources of entangled photons [LI00] and in quantum information processing for optical switch-

ing [HY98] or storage [LDBH01].

My PhD was conducted in the atom optics section of the Optics group at the University of Glasgow. I joined Dr. Franke-Arnold to work on the application of quantum interference in four-level linkages to information storage. The project to which we endeavoured was an investigation of how quantum information may be stored in the atomic populations using spatial modes of light [FA10]. Spatial mode storage has recently been realised in atomic vapours [PSF+07], but cold atoms offer longer diffusion times as well as reduced collision rates which may make them more suitable.

Clouds of atoms can be cooled using magneto-optical traps (MOTs), which combine near-resonant laser light and magnetic fields to slow and spatially confine up to a few billion atoms. MOTs commonly achieve temperatures around $100\,\mu$K and densities of about $10^9\,\mathrm{cm}^{-3}$. Working with Dr. Franke-Arnold, I built a magneto-optical trap in the "six-beam" configuration to cool and trap a cloud of a billion Rubidium atoms. The processes leading to atom cooling as well as a mathematical description of the measurements that can be made to characterise the number of trapped atoms and the atomic density and temperature are explained in Chapter 2. Chapter 3 then presents the experimental realisation of the scheme.

In the context of a study of the interaction of four waves with an atomic sample, a four-wave mixing process in a Rubidium vapour was also investigated as a collaboration between the group of Optics at Glasgow University and the group of Photonics from the University of Strathclyde. Chapter 4

details the experimental investigation of the efficient generation of 420 nm light from 780 nm and 776 nm pumping via four-wave mixing. This experiment, affectionately called "the blue light experiment" due to the distinctive colour of the emitted radiation, showed a variety of puzzling effects that we attempted to understand. The theoretical analysis performed to understand the experimental results is shown in Chapter 5.

We were also interested in the possible conversion of phase structures in the four-wave mixing process mentioned above. Chapter 6 shows the experimental results of a study of the conversion of Laguerre-Gaussian beams from the 780 nm and 776 nm beams to the 420 nm beam. Here again the system exhibited intricate behaviours which we attempted to interpret.

Finally, an overview of the results of this work will be given in the Conclusion, followed by a summary of the questions yet to be answered.

1.4 References

[BBG+04] D.A. Braje, V. Balić, S. Goda, G.Y. Yin, and S.E. Harris. Frequency mixing using electromagnetically induced transparency in cold atoms. Physical Review Letters, 93:183601, 2004.

[BBK+86] S.J. Buckle, S.M. Barnett, P.L. Knight, M.A. Lauder, and D.T. Pegg. Atomic interferometers. Optica Acta, 33:1129–1140, 1986.

[BHTW96] S. Babin, U. Hinze, E. Tiemann, and B. Wellegehausen. Continuous resonant four-wave mixing in double Λ level configurations of Na_2. Optics Letters, 21:1186–1188, 1996.

[BIH91] K.-J. Boller, A. Imamoğlu, and S.E. Harris. Observation of electromagnetically induced transparency. Physical Review Letters, 66:552555, 1991.

[Boh13] N. Bohr. On the constitution of atoms and molecules. Philosophical Magazine, 26:1–25, 1913.

[CW10] S. Clow and T. Weinacht. Four-level atomic interferometer driven by shaped ultrafast laser pulses. Physical Review A, 82:023411, 2010.

[FA10] S. Franke-Arnold. A toolbox for photon orbital angular momentum technology. CORDIS: Information and Communication Technologies Call FP7-ICT-2009-C, July 2010.

[FHH91] J.E. Field, K.H. Hahn, and S.E. Harris. Observation of electromagnetically induced transparency in collisionally broadened lead vapor. Physical Review Letters, 67:30623065, 1991.

[FIM05] M. Fleischhauer, A. Imamoğlu, , and J.P. Marangos. Electromagnetically induced transparency: Optics in coherent media. Reviews of Modern Physics, 77:633, 2005.

[GZT55] J.P. Gordon, H.J. Zeiger, and C.H. Townes. The MASER: New Type of Microwave Amplifier, Frequency Standard, and Spectrometer. Physical Review, 99:1264–1274, 1955.

[Har97] S. Harris. Electromagnetically induced transparency. Physics Today, 50, 1997.

[HHDB99] L. Vestergaard Hau, S.E. Harris, Z. Dutton, and C.H. Behroozi. Light speed reduction to 17 metres per second in an ultra cold atomic gas. Nature, 397:594–598, 1999.

[HKW02] A.F. Huss, E.A. Korsunsky, and L. Windholz. Phase control of electromagnetically induced transparency in a double-Λ, system. Journal of Modern Optics, 49:141–155, 2002.

[HY98] S.E. Harris and Y. Yamamoto. Photon switching by quantum interference. Physical Review Letters, 81:36113614, 1998.

[JXY+96] M. Jain, H. Xia, G. Y. Yin, A. J. Merriam, and S.E. Harris. Efficient nonlinear frequency conversion with maximal atomic coherence. Physical Review Letters, 77:43264329, 1996.

[KLH+99] E.A. Korsunsky, N. Leinfellner, A. Huss, S. Baluschev, and L. Windholz. Phase-dependent electromagnetically induced transparency. Physical Review A, 59:23022305, 1999.

[Lab10] MIT Spectroscopy Lab. The era of classical spectroscopy. http://web.mit.edu/spectroscopy/history/history-classical.html, August 2010.

[LDBH01] C. Liu, Z. Dutton, C.H. Behroozi, and L. Vestergaard Hau. Observation of coherent optical information storage in an atomic medium using halted light pulses. Nature, 409:490–493, 2001.

[LFZ+97] M.D. Lukin, M. Fleischhauer, A.S. Zibrov, H. G. Robinson, V.L. Velichansky, L. Hollberg, and M.O. Scully. Spectroscopy in dense coherent media: Line narrowing and interference effects. Physical Review Letters, 79:2959–2962, 1997.

[LHL+98] M.D. Lukin, P.R. Hemmer, M. Lffler, , and M.O. Scully. Resonant enhancement of parametric processes via radiative interference and induced coherence. Physical Review Letters, 81:2675–2678, 1998.

[LI00] M.D. Lukin and A. Imamoğlu. Nonlinear optics and quantum entanglement of ultraslow single photons. Physical Review Letters, 84:14191422, 2000.

[Luk03] M.D. Lukin. Colloquium: Trapping and manipulating photon states in atomic ensembles. Review of Modern Physics, 75:457472, 2003.

[MBC+81] M.J. Mumma, D. Buhl, G. Chin, D. Deming, F. Espenak, T. Kostiuk, and D. Zipoy. Discovery of natural gain amplification in the 10-micrometer carbon dioxide laser bands on Mars - a natural laser. Science, 212:45–49, 1981.

[MFAO02] G. Morigi, S. Franke-Arnold, and G.-L. Oppo. Phase-dependent interaction in a four-level atomic configuration. Physical Review A, 66:053409, 2002.

[oA07] Optical Society of America, editor. Phase Dependent EIT, 2007. Frontiers in Optics, OSA Technical Digest; paper FWT2.

[PFM+01] D.F. Phillips, A. Fleischhauer, A. Mair, R. L. Walsworth, and M.D. Lukin. Storage of light in atomic vapor. Physical Review Letters, 86:783786, 2001.

[Pla14] M. Planck. Neue bahnen der physikalischen erkenntnis. Philosophical Magazine, 28, 1914. Trad. F. d'Albe.

[PSF+07] R. Pugatch, M. Shuker, O. Firstenberg, A. Ron, and N. Davidson. Topological stability of stored optical vortices. Physical Review Letters, 98:203601, 2007.

[Sam58] S. Sambursky. Philoponus' interpretation of aristotle's theory of light. Osiris, 13:114–126, 1958.

[Sam75] S. Sambursky. Physical thought, from the presocratics to the quantum physicists : an anthology / selected, introduced, and edited by Shmuel Sambursky. Pica Press, New York, 1975.

[Sch26] E. Schrödinger. An undulatory theory of the mechanics of atoms and molecules. Physical Review, 28:1049–1070, 1926.

[Scu91] M.O. Scully. Enhancement of the index of refraction via quantum coherence. Physical Review Letters, 67:18551858, 1991.

[SH90] M.S. Shahriar and P.R. Hemmer. Direct excitation of microwave-spin dressed states using a laser-excited resonance Raman interaction. Physical Review Letters, 65:1865–1868, 1990.

[Ste05] S. Stenholm. Foundations of Laser Spectroscopy. Dover Publications inc., Mineola, New York, 2005.

[Tay99] C.C.W. Taylor. The atomists Leucippus and Democritus : fragments : a text and translation / with a commentary by C. C. W. Taylor. University of Toronto Press, Toronto ; London, 1999.

[WLR50] Jr. W.E. Lamb and R.C.Retherford. Fine structure of the hydrogen atom. Physical Review, 79:549–572, 1950.

[ZS96] P. Zhou and S. Swain. Ultranarrow spectral lines via quantum interference. Physical Review Letters, 77:3995–3998, 1996.

CHAPTER 2

Magneto Optical Trapping: elements of theory

The Magneto-Optical Trap (MOT), first demonstrated in 1987 [RPC+87], has become an essential tool for the experiments requiring low temperature, long lived atomic coherences or high phase space density. This development has had major repercussions, both in fundamental and applied research, leading to the observation of Bose-Einstein condensates (BEC) in 1995 [AEM+95] and to the improvement of optical clocks using atomic fountains by an order of magnitude [LHJ07].

Magneto-optical trapping offers a both a long coherence time compared to hot vapours due to a reduced collision rate and Doppler width, and a longer interaction time with the excitation fields. Although the study of phase dependent phenomena in atomic processes does not require cold

atomic samples, as demonstrated in Ref. [PSF+07], cooling is particularly relevant for atomic population manipulation or in experiments in which the coherence time is particularly sensitive to collisions [CDBH01, LMK01].

Radiation pressure is at the base of magneto-optical trapping: it provides a velocity-dependent force which decelerates atoms travelling in the opposite direction to a red-detuned light beam. This mechanism called Doppler cooling is independent of space, hence it is insufficient to generate a confining potential. As the level structure of Rubidium is sensitive to magnetic fields, the spatial dependence of the cooling force can be ensured by a spatially varying magnetic field. It should be emphasised that due to the multitude of physical phenomena that take place within the cold atoms (cold collisions, multiple scattering and spatially dependent energy shifts due to polarisation gradients [DCT89]), the magneto-optical trap is a complex system, and the limitations of this cooling scheme in terms of phase space density (number of atoms in a volume of sides λ_{dB}) are difficult to assess theoretically. An interesting investigation of this topic, joining theoretical perspective to experimental evidence can be found in Ref. [TEC+95].

The scope of this chapter is the presentation of a one-dimensional model of the magneto-optical trap, as well as the derivation of some simple descriptions used to fit the experimental data in the next chapter.

2.1 How a MOT works

The processes underlying magneto-optical trapping can be separated into two parts: cooling, and trapping. In the absence of any external magnetic field, the simple pressure of red-detuned laser fields is sufficient to cool the atoms to 1 mK. The system made of the atoms and the radiation is called optical molasses due to the viscous damping force the atoms undergo [CHB+85]. Imposing a magnetic field gradient then traps the atoms in an effective potential well, the minimum of which corresponds to zero of the the magnetic field. In this section we will present a one dimensional description of the physical effects underlying the cooling and trapping processes.

2.1.1 Doppler cooling

Doppler cooling stems from the conservation of momentum in an absorption-emission cycle. This phenomenon can be easily modeled in one dimension, giving qualitative insight and fairly accurate quantitative agreement with experimental results.

Upon the absorption of a photon, a momentum of $\underline{\mathbf{p}} = \hbar\underline{\mathbf{k}}$ is imparted to the atom. Spontaneous re-emission of the absorbed radiation is isotropic, therefore the atom undergoes a recoil of $\hbar k$ in a random direction. Over a large number of cycles, this results in a net transfer of momentum to the atoms in the direction of the beam.

Due to the Doppler effect, the probability of absorption of a photon is

directional: an atom with velocity **v** travelling within a beam with frequency ω_0 experiences an effective frequency $\omega = \omega_0 (1 + \underline{\mathbf{v}}.\underline{\mathbf{k}}./c)$. For the beam to be resonant with this atom it must be detuned by $\omega_0 v/c$, as shown in Figure 2.1. To slow an atom, the beam must be red-detuned so that it is more resonant with counter-propagating photons. Applying two identical, red-detuned, counterpropagating beams to an atomic vapour generates a force that can keep the atoms' velocity within a few centimetres per second.

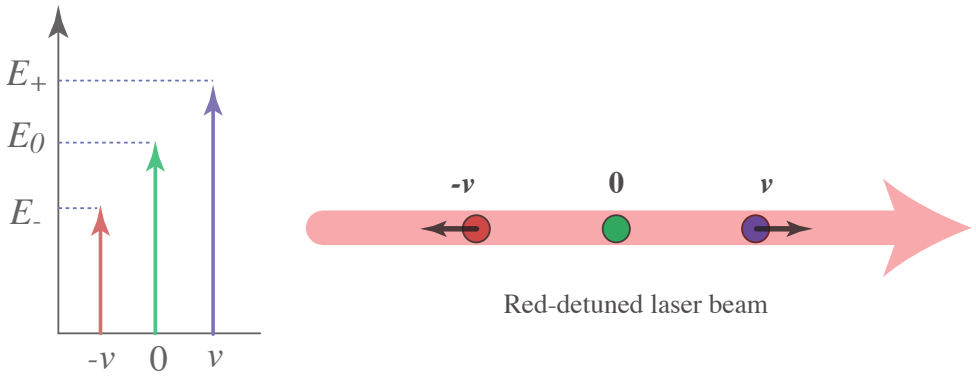

Figure 2.1: Doppler shifted transition: An atom travelling in the opposite direction of a quasi-resonant laser beam "sees" photons with a higher frequency, which is equivalent to the atom having its energy levels lowered with respect to the laser beam. Using red-detuned light allows the increase of the probability of absorption by counter-propagating atoms.

The radiation pressure force on the atom as a function of the scattering rate f/τ is given by:

$$F = \frac{\Delta p}{\Delta t} = \frac{\hbar k}{\tau / f}, \tag{2.1}$$

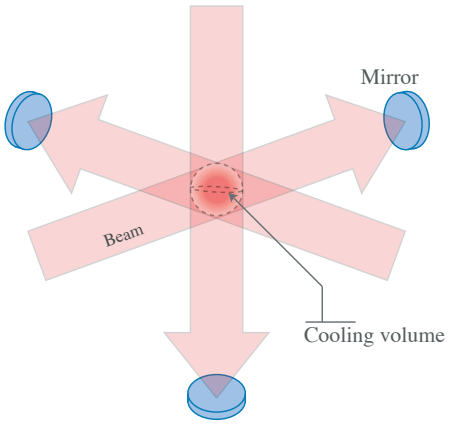

Figure 2.2: Cooling scheme with three retro-reflected beams

where τ is the excited state lifetime and f the steady state fraction of excited atoms.

Consider the the one-dimensional case, where two counterpropagating red-detuned beams are absorbed according to a power-broadened Lorenzian. The total force applied on the atoms is thus given by [AR97, LPR+89]:

$$F(v) = \hbar k \frac{\Gamma}{2} \left[\frac{I/I_{sat}}{4(\delta - kv)^2/\Gamma^2 + (1 + 2I/I_{sat})} \right] - \hbar k \frac{\Gamma}{2} \left[\frac{I/I_{sat}}{4(\delta + kv)^2/\Gamma^2 + (1 + 2I/I_{sat})} \right], \quad (2.2)$$

where $\delta = \omega_L - \omega_0$ is the detuning and I_{sat} is the saturation intensity (intensity for which a resonant atom spends 1/4 of its time in the excited state). The value of $|v|$ for which $F(v)$ is maximum is called the capture velocity.

The velocity-dependent acceleration that ensues is shown for Rubidium

on Figure 2.3 with the commonly used values $I/I_{sat} \approx 1$ and $\delta \approx -\Gamma/2$, set to optimise the steady state temperature (Figure 2.6).

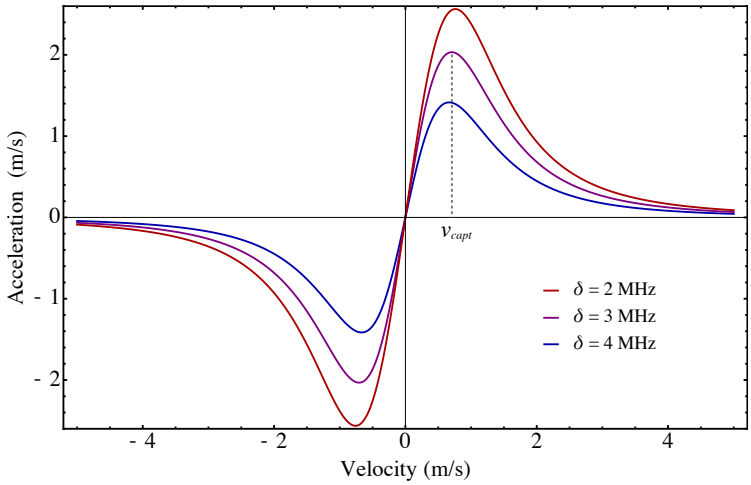

Figure 2.3: Velocity-dependent acceleration: as the beam detuning is increased, the capture velocity and the maximum deceleration decreases.

Around $v = 0$, this acceleration is linear with v. It is equivalent to a damping force $F = -\alpha v$. For $2kv/\delta \ll 1$:

$$\alpha \approx -k\frac{\delta}{\Gamma}\frac{1}{4\left(\delta/\Gamma\right)^2 + 1/3} \tag{2.3}$$

This cooling scheme is commonly implemented in three dimensions by applying six laser beams with equal power as shown in Figure 2.2. It was also demonstrated that the beams can be arranged in a tetrahedron [CLdO+94].

In this regime the atoms behave as a viscously damped medium which is thus called optical molasses. As the speed of the atoms decreases, their

transition becomes less resonant with the incoming beam, thus reducing the scattering rate. A spatially dependent magnetic field can then produce a confining potential well due to the Zeeman effect.

2.1.2 Magneto-optical slowing and trapping

Optical molasses generates a cloud of atoms with a speed centered around 0.5 m/s, corresponding to a temperature of about 1 mK. It can be shown that adding a linearly varying magnetic field whose zero is centred at the crossing point of the cooling beams yields a potential well. The atoms accumulate and slow, reaching higher densities ($10^{10}\,\mathrm{cm}^{-3}$) and temperatures down to a few hundreds of μK [LPR+89].

Alkali metals possess a nonzero nuclear spin angular momentum which couples with the total angular momentum J of the electron. This gives them a hyperfine structure, as shown for Rubidium in Appendix A. The degeneracy of the hyperfine magnetic sub-levels m_F is removed in the presence of a magnetic field. Indeed, each m_F corresponds to a projection of the total angular momentum F on the quantisation axis whose direction is defined by the orientation of the magnetic field.

Each hyperfine sub-level of magnetic number m_F and Landé g-factor g_f [CT05] possesses an effective magnetic moment $g_f m_F \mu_B$ that precesses around a magnetic field $B_o(r)$ at the Larmor frequency $\omega_l(r) = g_f m_f \mu_B B_o(r)/\hbar$ where μ_B is the Bohr magneton. The interaction between the magnetic field and the magnetic moment removes the degeneracy be-

tween the m_F, which are shifted by $\Delta E\,(r) = g_f m_f \mu_B B_o\,(r)$. Applying a magnetic field gradient is equivalent to having a spatially dependent energy shift and quantisation axis. In one dimension, the energy shift is linear and can be visualised as shown in Figure 2.4 b).

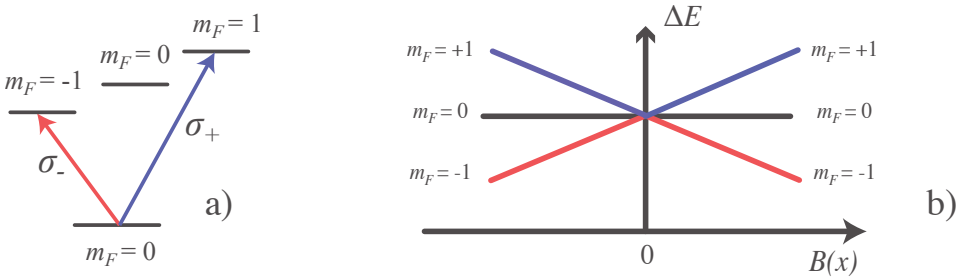

Figure 2.4: Hyperfine level shifts: the level shift is proportional to the magnetic field and to the magnetic number m. In order to drive the transition $m_F = 0 \rightarrow m_{F'} = +1$ according to the selection rules (conservation of angular momentum) the light must be polarised with positive angular momentum with respect to the direction of the magnetic field, as shown in a) and b). The light thus polarised is called σ_+.

Applying a magnetic field removes the degeneracy of the ground state hyperfine levels, as a result there are multiple ground states into which the atom can decay. In order to have a trapping system as close to a two-level atom as possible, the trapping lasers must be circularly polarised and carry angular momentum with respect to the quantisation axis (Figure 2.5). One can then to a first approximation consider that all atoms are pumped to the

highest angular momentum states and that only the largest m_F contributes to the slowing cycle.

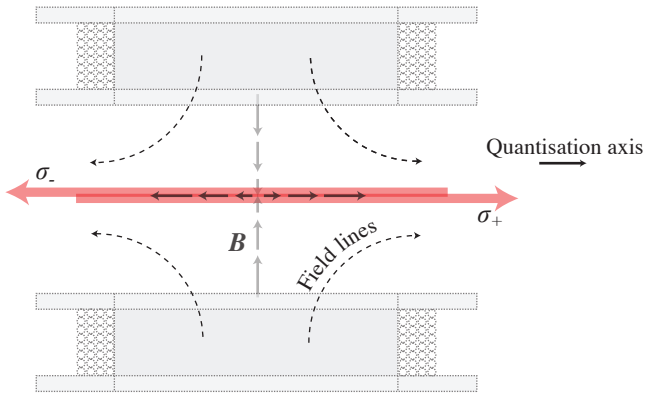

Figure 2.5: Quantisation axis convention: in the case of a spatially varying magnetic field direction, one direction is conventionally chosen as the main quantisation axis. In a magneto-optical trap, the sign of the magnetic field is spatially dependent and the quantisation axis is chosen to be along the positive magnetic field vector. The incoming beam and the reflected beam have the same polarisation, but opposite handedness with respect to the quantisation axis, leading to the convention depicted above

The force exerted on the atoms can be expressed as:

$$F(v) = \hbar k \frac{\Gamma}{2} \left[\frac{I/I_{sat}}{4\left(\delta - kv + \Delta E/\hbar\right)^2/\Gamma^2 + (1 + 2I/I_{sat})} \right] - \hbar k \frac{\Gamma}{2} \left[\frac{I/I_{sat}}{4\left(\delta + kv + \Delta E/\hbar\right)^2/\Gamma^2 + (1 + 2I/I_{sat})} \right] \quad (2.4)$$

Experimentally, a detuning of $-13\,\mathrm{MHz}$, and a field gradient of $10\,\mathrm{gauss/cm}$ (for comparison, the Earth's magnetic field is about $0.3\,\mathrm{gauss}$)

[LSW92] yielded the lowest temperature and highest density. This gives a capture velocity of about 10 m/s 1 cm away from the centre of the trap. It might seem a very small velocity compared to the room temperature average of about 100 m/s, but it was experimentally demonstrated in 1990 that the fraction of atoms in the tail of the Maxwell-Boltzmann distribution of a Rb vapour is sufficient to ensure a substantial loading rate into the MOT [MSRW90] .

This scheme combining electromagnetic radiation pressure with magnetic field gradients was predicted to reach the Doppler temperature [LPR+89] T_D (Equation 2.5), plotted in Figure 2.6.

$$T_D = \frac{\hbar\Gamma}{4k_B}\frac{1 + I_T/I_{Sat} + (2\delta/\Gamma)^2}{-2\delta/\Gamma} \tag{2.5}$$

In the limit of $I_T/I_{Sat} \ll 1$, the Doppler temperature reaches its minimum $\hbar\Gamma/2k_B$ for a beam detuning $\delta = -\Gamma/2$. With a decay rate $\Gamma = 2\pi \times 6\,\mathrm{MHz}$, the Doppler temperature of Rubidium is $145\,\mu\mathrm{K}$.

Historically, the experimental conditions were refined empirically from the ballpark figures found by the two-level atom models given above. More refined descriptions were attempted later to explain the experimental findings [LPR+89, DCT89, GM94, LSW92]. Interestingly, the first experiments on sodium vapours revealed that optical molasses worked better than predicted by the theory. Phillips' group in NIST found in 1988 that the temperature of their sodium optical molasses was not the predicted $240\,\mu\mathrm{K}$ but

$43\pm20\,\mu$K [LWW+88]. In 1989, Dalibard and Cohen-Tannoudji developed a theory to understand this surprising outcome. Their model was based on the dressed-atom picture [DCT85] considering all hyperfine magnetic sublevels and the polarisation gradient resulting from the overlap of the two circularly polarised beams.

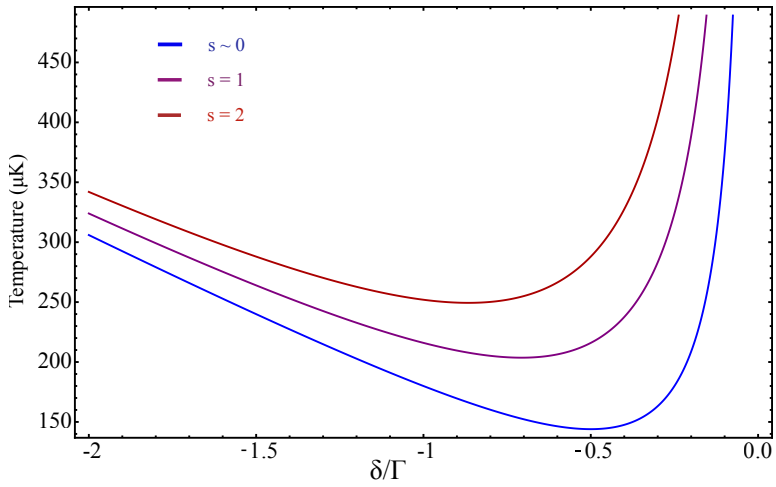

Figure 2.6: Temperature vs. beam detuning: $s \ll 1$ minimises the residual scattering of the trapped atoms and yields the Doppler temperature for $\delta = \Gamma/2$

2.2 Measurements

The properties we will examine here are the temperature, the density of the cloud, and the atomic collisional cross-section. The latter is particularly important to evaluate the lifetime of coherent behaviour. Experimentally, one can measure the trap loading rate, the atomic density and the velocity

spread. This section presents some simple models to estimate the collisional cross-section and the temperature of the atoms from the measurements.

2.2.1 Collisional cross-section of trapped atoms

The collisional cross-section of the atoms is particularly relevant when studying coherent effects that can be washed out by collisions with the thermal background. It will be shown here that this property can be estimated directly from a measurement of the steady state number of trapped atoms.

First, let us consider the time dependence of the number of atoms in the trap, which is the result of the balance between the loading rate R_+ and the loss rate R_- :

$$\frac{dN}{dt} = R_+ - R_- \tag{2.6}$$

We assume that the vacuum is very high and that only a small fraction of the Rubidium vapour is trapped. To a first approximation the losses are mainly due to the collision rate $1/\tau$ with the background Rubidium which is proportional to the Rb density n_{Rb}, the collisional cross-section σ_{Rb} and the mean thermal velocity v_{th} of the background gas relative to the trapped atoms:

$$R_- = N\frac{1}{\tau} = N n_{Rb}\sigma_{Rb}v_{th} \tag{2.7}$$

The loading rate can be estimated from a two level system in the absence of magnetic field as the flux of atoms with velocity smaller than the capture velocity v_c that enter the trapping area here approximated by a sphere of area $A = 4\pi r^2$, as shown on Figure 2.7.

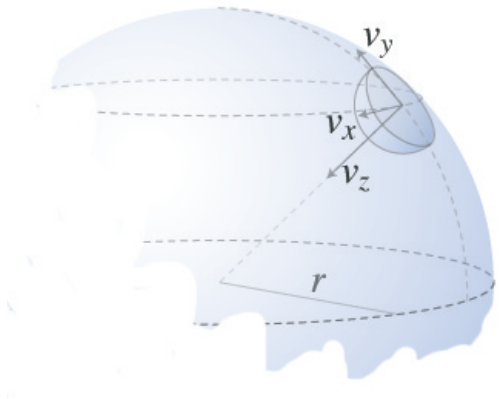

Figure 2.7: The loading rate is estimated from the number of atoms that enter the trapping area $A = 4\pi r^2$ with a velocity smaller than the capture velocity

In the simplest case where the velocity of all atoms is perpendicular to the area A, the flux is given by $\Phi = nA\bar{v}_n$ where $\bar{v}_n$ is the mean velocity of the atoms, and n the atomic density. In our system, the velocities are randomly distributed in all directions and their modulus follows a Maxwell-Boltzmann distribution:

$$f_B(v) = \left(\frac{3}{2}\right)^{3/2} \frac{1}{\pi^{3/2} v_{th}^3} \exp\left(-\frac{3}{2}\frac{|v|^2}{v_{th}^2}\right), \tag{2.8}$$

where $v_{th} = \sqrt{\frac{3k_B T}{m_{Rb}}}$ is the mean thermal velocity.

Only the velocity component that is normal to the surface and directed towards the inside of the sphere contributes to the loading rate (see Figure 2.7), so the mean velocity $\bar{v}$ is calculated from the sum of all projections of v on $\hat{n}$ over the half sphere shown on Figure 2.8:

$$\bar{v} = \int_0^{v_c} dv \int_0^{2\pi} d\phi \int_0^{\frac{\pi}{2}} d\theta v^2 \sin\theta \left(v\cos\theta\right) f_B\left(v\right) \tag{2.9}$$

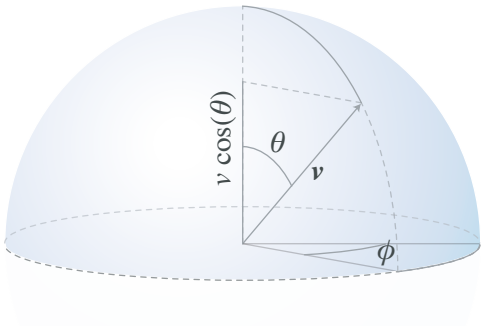

Figure 2.8: Volume of integration for the calculation of the mean value of the normal component of the atomic velocity

With $\exp\left(-\frac{3}{2}\frac{|v|^2}{v_{th}^2}\right) \approx 1 - \frac{3}{2}\frac{|v|^2}{v_{th}^2}$ for $v_c \ll v_{th}$:

$$\bar{v} \approx \frac{3v_c^4}{4\sqrt{\pi}v_{th}^3} \tag{2.10}$$

The loading rate R_+ is then:

$$R_+ = n_{Rb}\bar{v}A\frac{3v_c^4}{4\sqrt{\pi}v_{th}^3} \tag{2.11}$$

The time dependence of the atoms is thus given by:

$$N = \frac{3}{4}\left(\frac{v_c}{v_{th}}\right)^4 \frac{A}{\sigma_{Rb}}\left(1 + e^{-n_{Rb}\sigma_{Rb}v_{th}t}\right) \tag{2.12}$$

N is thus independent of the background thermal density (although the lifetime within the trap is), and the collisional cross-section of Rubidium σ_{Rb} can simply be deduced from the number of atoms in the trap. This figure can be cross-checked by comparing the measured to the calculated loading rate $n_{Rb}\sigma_{Rb}v_{th}$ (replacing σ_{Rb} with the calculated value and n_{Rb} with the measured atomic density).

2.3 References

[AEM+95] M.H. Anderson, J.R. Ensher, M.R. Matthews, C.E. Wieman, and E.A. Cornell. Observation of Bose-Einstein condensation in a dilute atomic vapor. Science, 269:198–201, 1995.

[AR97] C.S. Adams and E. Riis. Laser cooling and trapping of neutral atoms. Progress in Quantum Electronics, 21:1–79, 1997.

[CDBH01] C.Liu, Z. Dutton, C.H. Behroozi, and L. Vestergaard Hau. Observation of coherent optical information storage in an atomic medium using halted light pulses. Nature, 409:490–493, 2001.

[CHB+85] S. Chu, L. Hollberg, J.E. Bjorkholm, A. Cable, and A. Ashkin. Three-dimensional viscous confinement and cooling of atoms by

resonance radiation pressure. Physical Review Letters, 55:48–51, 1985.

[CLdO+94] C. Chesman, E.G. Lima, F.A.M. de Oliveira, S.S. Vianna, and J.W.R. Tabosa. Two- and four-beam magneto-optical trapping of neutral atoms. Optics Letters, 19:1237–1239, 1994.

[CT05] C. Cohen-Tannoudji. Quantum Mechanics. Wiley-VCH, 2005.

[DCT85] J. Dalibard and C. Cohen-Tannoudji. Dressed-atom approach to atomic motion in laser light: the dipole force revisited. Journal of the Optical Society of America B, 2:1707–1720, 1985.

[DCT89] J. Dalibard and C. Cohen-Tannoudji. Laser cooling below the Doppler limit by polarization gradients: simple theoretical models. Journal of the Optical Society of America B, 6:2023–2045, 1989.

[GM94] M. Gajda and J. Mostowski. Three-dimensional theory of the magneto-optical trap: Doppler cooling in the low-intensity limit. Physical Review A, 49:4864–4875, 1994.

[LHJ07] M.A. Lombardi, T.P. Heavner, and S.R. Jefferts. NIST primary frequency standards and the realization of the S.I. second. The Journal of Measurement Science, 2(4):74–89, 2007.

[LMK01] G. Labeyrie, C. Miniatura, and R. Kaiser. Large Faraday rotation of resonant light in a cold atomic cloud. Physical Review A, 64:1050–2947, 2001.

[LPR+89] P.D. Lett, W.D. Phillips, S.L. Rolston, C.E. Tanner, R.N. Watts, and C.I. Westbrook. Optical molasses. Journal of the Optical Society of America B, 6:2084–2107, 1989.

[LSW92] K. Lindquist, M. Stephens, and C. Wieman. Experimental and theoretical study of the vapor-cell Zeeman optical trap. Physical Review A, 46:4082–4090, 1992.

[LWW+88] P.D. Lett, R.N. Watts, C.I. Westbrook, W.D. Phillips, P.L. Gould, and H.J. Metcalf. Observation of atoms laser cooled below the doppler limit. Physical Review Letters, 61:169–172, 1988.

[MSRW90] C. Monroe, W. Swann, H. Robinson, and C. Wieman. Very cold trapped atoms in a vapor cell. Physical Review Letters, 65:1571–1574, 1990.

[PSF+07] R. Pugatch, M. Shuker, O. Firstenberg, A. Ron, and N. Davidson. Topological stability of stored optical vortices. Physical Review Letters, 98:203601, 2007.

[RPC+87] E.L. Raab, M. Prentiss, A. Cable, S. Chu, and D.E. Pritchard.

Trapping of neutral sodium atoms with radiation pressure. Physical Review Letters, 59:26312634, 1987.

[TEC+95] C.G. Townsend, N.H. Edwards, C.J. Cooper, K.P. Zetie, C.J. Foot, A.M. Steane, P. Szriftgiser, H. Perrin, and J. Dalibard. Phase-space density in the magneto-optical trap. Physical Review A, 52:14231440, 1995.

CHAPTER 3

Experimental Realisation

Performing experiments using a MOT generally requires a stable number of atoms and low thermal fluctuations, which is ensured by a narrow laser linewidth compared to that of the trapping transition. With a D2 natural linewidth of 6.07 MHz, Rubidium can be trapped reliably with a 3 MHz wide laser, corresponding to a frequency precision $(\Delta\omega)/\omega = 3 \times 10^{-9}$. Such precision is well within reach of commonly used Extended Cavity Diode Lasers (ECDLs) locked on atomic transitions, which typically have a linewidth of 1 MHz. ECDLs can be sourced commercially, but an inexpensive and sufficiently reliable option consists in a home-built design [MSW92, AWB97, WH91] that is detailed in the first section of this chapter.

Due to mechanical vibrations and thermal variations, the frequency of a free running, temperature and current controlled ECDL fluctuates by a

few 100 MHz over timescales of minutes. It is therefore necessary to lock the lasers to a fixed, narrow reference. For atom trapping, the most obvious reference is the atomic transition itself. Doppler broadening at room temperature can be overcome by using saturated absorption spectroscopy. The optical saturated absorption setup and the locking mechanism are presented in Section 3.1.2.

As shown in Section 2.2.1 an ultra high vacuum is important to ensure a low inter-species collision rate. The assembly, baking, and pumping of a system reaching a pressure down to 10^{-9} mbar (gauge-limited measurement of our vacuum system) requires care and method. Section 3.2 gives an account of the steps that were taken to build the vacuum enclosure.

Magneto-optical trapping requires the use of spatially controlled magnetic fields, both for trapping and for compensation of stray fields. This is achieved using electromagnets, whose design (radius, number of turns, wire thickness) is discussed in Section 3.3. The stability of the magnetic field generated by the electromagnets was ensured by a servo loop which schematic is given in Appendix **??**.

The trap was built using the standard setup of three retroreflected beams at right angles to one another, crossing at the magnetic field zero defined by the trapping coils. The first atoms were trapped in May 2008 (Figure 3.1).

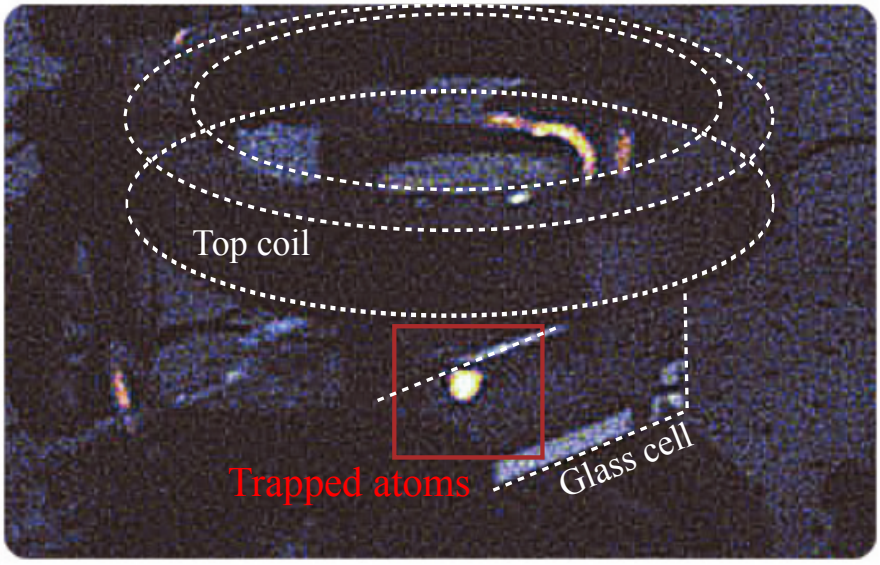

Figure 3.1: Picture of the first observed trapped atoms

3.1 Laser design and control

3.1.1 Laser design

A bare laser diode has a linewidth of a few hundreds of MHz which is too broad to suit our purpose. The extension of the cavity with a diffraction grating allows a frequency-selective feedback that reduces the linewidth to about 3 MHz over a timescale of hours when the laser is locked (3.1.2). The distance L between the grating and the diode determines the frequency selectivity of the feedback: a large L yields a fine linewidth but also makes the cavity more difficult to stabilise as mechanical vibrations and refractive index fluctuations in the extended cavity are inevitable. A compromise

between the two is found for $L \approx 1\,\text{cm}$ to $L \approx 2\,\text{cm}$. The emitting frequency of the laser is then defined by a combination of the grating angle, the external and internal cavity length (the length of the diode itself). It was shown that the mode-hop free scanning range can be optimised by choosing the pivot point of the piezo scan [NDA99]. Provided the grating angle and cavity length are not working against one another, a scanning range of a few GHz can easily be achieved.

The design of the extended cavity is inspired from [MSW92] and [AWB97], which both use a modified commercial mirror mount to adjust the grating angle. Three designs were tried, with various sizes of mirror mounts and piezoelectric transducers, each with its advantages and drawbacks. In the first two versions, only the laser diode was temperature controlled and the external cavity was mounted on a large stainless steel block (Figure 3.12). This was a practical design for collimating the laser, but as the external cavity temperature drifted during the day, the laser required regular readjusting. The mirror mount of the first design was small and stable but difficult to tune as the knobs were also quite small. The following version had a longer transducer which was convenient to compensate for the thermal drift, but made the laser much more sensitive to vibrations resulting in a shorter locking time. Eventually the last design, taken directly from [AWB97], provided the required stability and ease of adjustment.

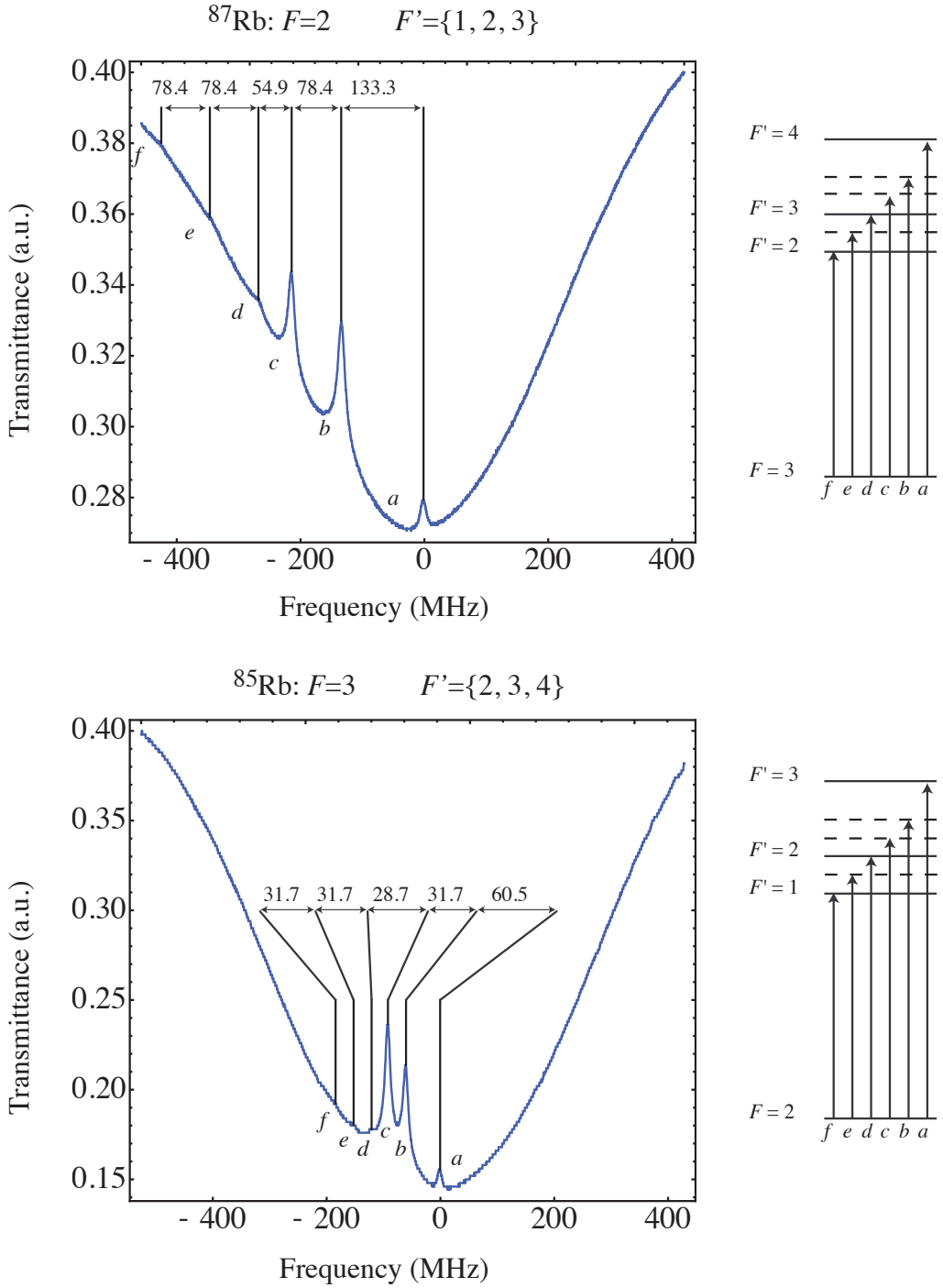

Figure 3.2: Saturated absorption spectrum, upper hyperfine. Top: ^{87}Rb, Bottom: ^{85}Rb

3.1.2 Frequency control

Both the temperature and current are controlled by a commercial Thorlabs laser diode driver and the frequency is fine tuned by adjusting the grating with a piezo-electric transducer (PZT). In order to lock the frequency of the laser, an electronic signal from a frequency reference is required. For our application, a natural oscillator is the Rubidium atomic transition itself which can be turned into an electric signal using the photodiode signal from a saturated absorption spectroscopy setup, as shown on Figure 3.3. Some laser light is picked-off near the Brewster's angle from the beam with a glass blank and sent into a Rb gas glass cell at room temperature. The weak beam is then back-reflected into the cell and deflected to a photodiode using a 70/30 beamsplitter. Frequency scans of the laser across the absorption lines show the four Doppler-broadened transitions corresponding to the two hyperfine ground state doublets (one for each isotope) as well as the hyperfine structure of the atom. The spectra of the lower and upper hyperfine levels of both isotopes are plotted respectively on Figure 3.4 and Figure 3.2. Well resolved hyperfine peaks can then be used as a reference to lock the lasers.

In practice, the lasers are locked on the hyperfine features using the method that follows. The frequency of the laser light is modulated via the piezoelectric transducer (PZT) at ω_m by applying a small modulation depth δ compared to the width of the hyperfine dip. This frequency modu-

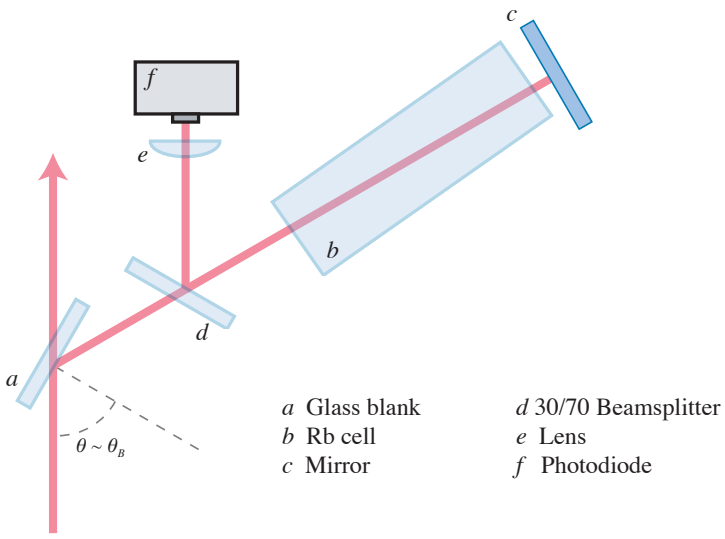

Figure 3.3: Saturated absorption spectroscopy setup

lation is turned into an amplitude modulation by the saturated absorption setup, and the amplitude of this signal is roughly proportional to the local gradient, as schematically depicted on Figure 3.5. The signal is then demodulated to convert the amplitude to a DC signal which can then be used as an error signal, thus making the top of the hyperfine peak the stable position of the servo loop. Figure 3.6 shows a scan of the error signal for the ground state hyperfine doublet of ^{87}Rb. This error signal is finally integrated over the relevant time constant (typically 1 ms) and sent to the PZT.

A simplified mathematical approach is helpful to understand the locking method. First, consider an input beam with electric field $E(t)$ at frequency

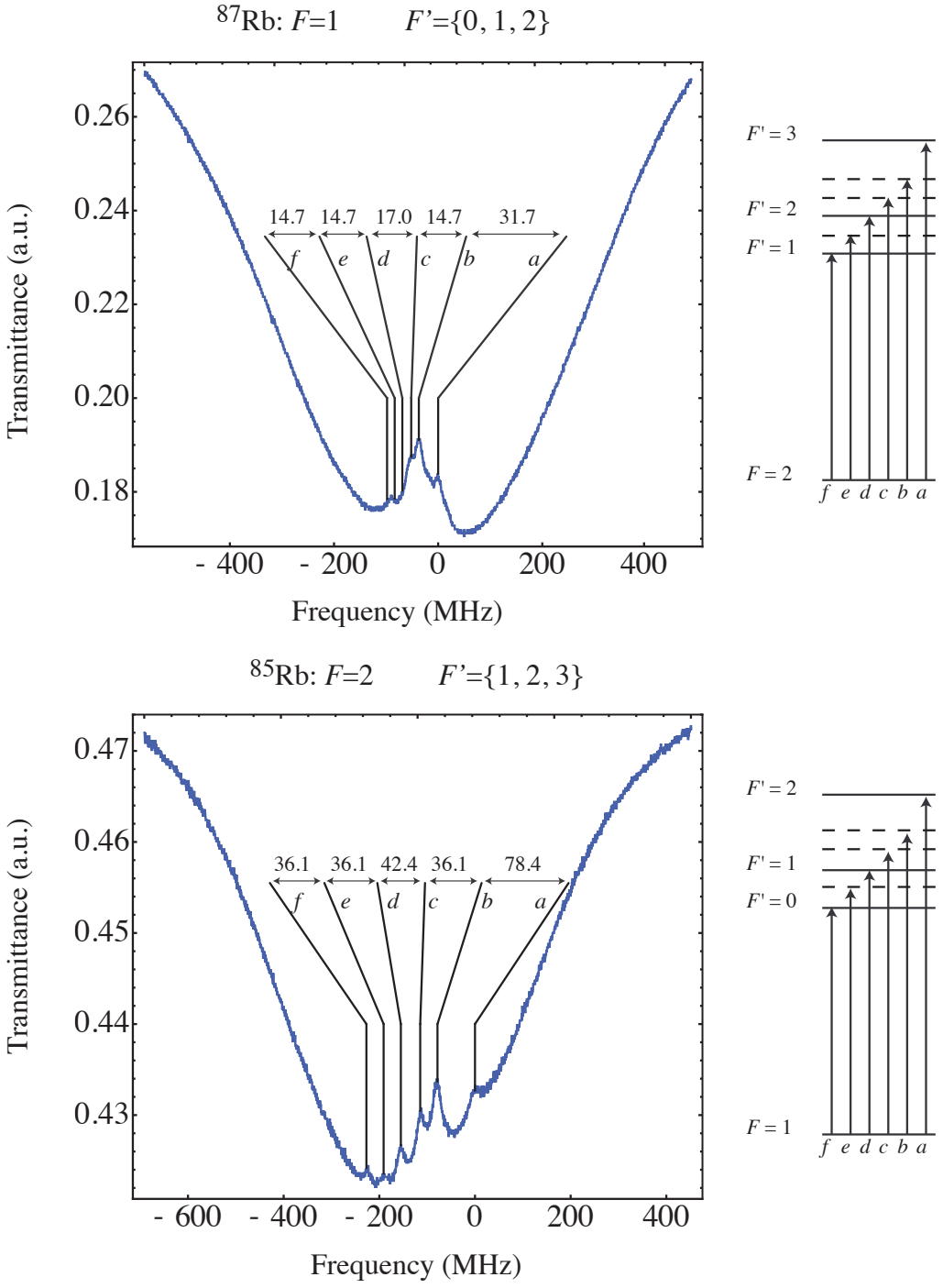

Figure 3.4: Saturated absorption spectrum, lower hyperfine. Top: ^{85}Rb, Bottom: ^{87}Rb

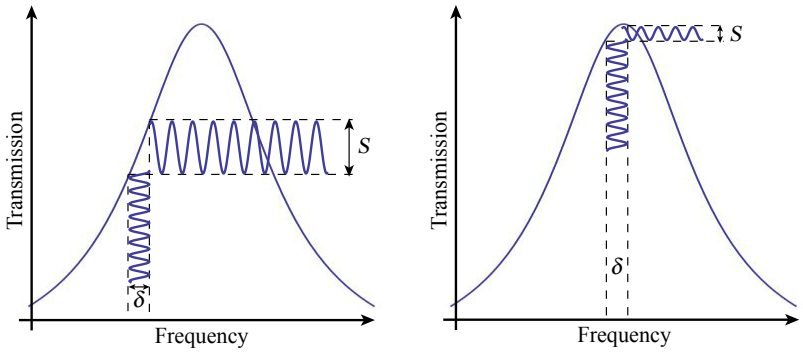

Figure 3.5: The amplitude of the AC component of the photodiode signal S depends on the local gradient of the absorption. At the top of the peak $S \approx 0$, so it is the point of equilibrium of the loop.

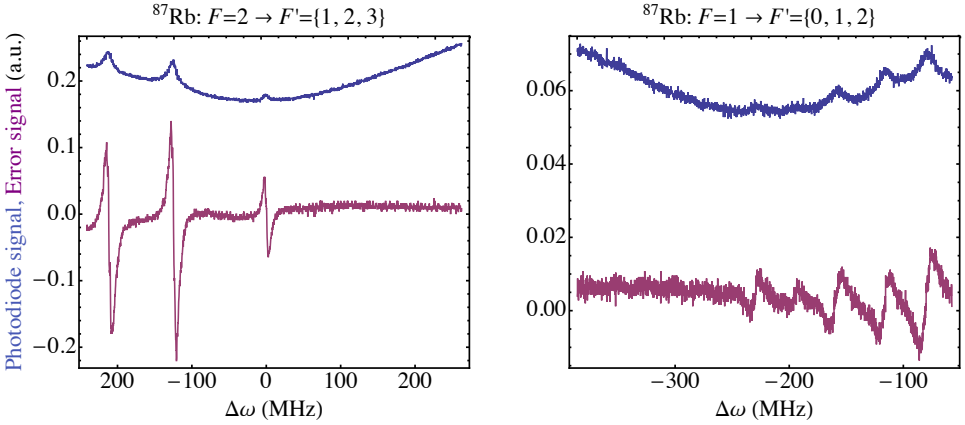

Figure 3.6: Scan of the error signal for both absorption lines of ^{87}Rb

ω and modulated at ω_m with a modulation depth δ :

$$\begin{aligned} E(t) &= E_0 \exp\left(i\left(\omega t + \delta \sin\left(\omega_m t\right)\right)\right) \\ &= E_0 e^{i\omega t} \exp\left(i\delta \sin\left(\omega_m t\right)\right) \\ &= E_0 e^{i\omega t} \exp\left(\delta \frac{e^{i\omega_m t} - e^{-i\omega_m t}}{2}\right) \end{aligned} \tag{3.1}$$

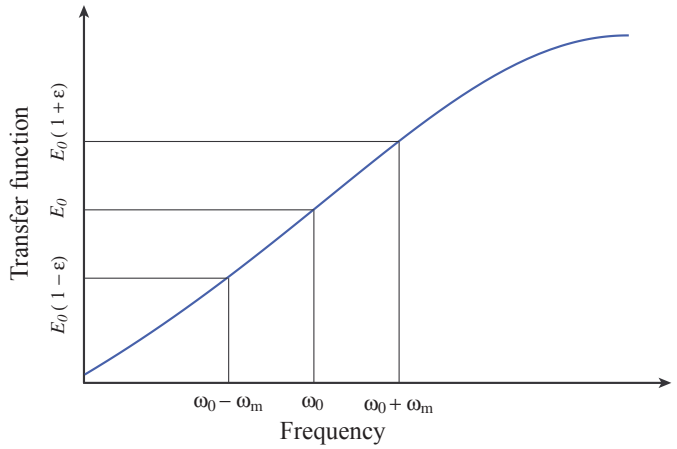

Figure 3.7: The transfer function of the absorbing medium can be considered linear if ω_m is small compared to the width of the absorption line.

For $\delta \ll 1$ this expression can be simplified to $E(t) \approx E_0 e^{i\omega t}\left(1+\frac{\delta}{2}e^{i\omega_m t}+\frac{\delta}{2}e^{-i\omega_m t}\right)$. Because the modulation frequency is small compared to the width of the hyperfine peak, one can assume on first approximation that the frequency dependent transfer function is linear (Figure 3.7), and for mathematical convenience the resulting field can be expressed as:

$$\begin{aligned} E'(t) &\approx E_0' e^{i\omega t}\left(1+\frac{\delta}{2}e^{i\omega_m t}(1+\varepsilon)-\frac{\delta}{2}e^{-i\omega_m t}(1-\varepsilon)\right) \\ &= E_0' e^{i\omega t}\left(1+i\sin\delta(\omega_m t)+\delta\varepsilon\cos(\omega_m t)\right) \end{aligned} \tag{3.2}$$

The power measured by the photodiode to first order in δ is then:

$$\begin{aligned} S &\propto E.E^* = P_0\left(1 + 2\varepsilon\delta\cos(\omega_m t) + \delta^2\sin^2(\omega_m t) + \varepsilon^2\cos(\omega_m t)\right) \\ &\approx P_0\left(1 + 2\varepsilon\delta\cos(\omega_m t)\right) \end{aligned} \tag{3.3}$$

This AC component of S is multiplied by the modulating wave with phase ϕ:

$$\begin{aligned} S_\times &\propto S_{AC}.\sin(\omega_m t + \phi) \\ &\propto \varepsilon\delta\sin(\omega_m t)\sin(\omega_m t + \phi) \\ &\propto \varepsilon\delta(\sin(2\omega_m t + \phi) + \sin(\phi)) \end{aligned} \tag{3.4}$$

The error signal ϵ is finally obtained by low-pass filtering $S_\times$:

$$\epsilon \propto \delta\varepsilon\sin(\phi) \tag{3.5}$$

For the top of the absorption peak to be a stable equilibrium point, ϕ must be tuned to maximise the error signal and to give it the right sign.

The circuit addressing the PZT for scanning, modulating and locking and the modulating/demodulating circuit were taken from Ref. [Arn99] and modified due to a discontinued VCO. This system applied a large 40 kHz modulation to the PZT, which is above its resonance frequency. The response of the PZT at such a high frequency is small, so a larger voltage had to be applied to obtain a sufficiently large modulation depth. Unfortunately, this solution did not work very well with our designs due to the

very poor response of the system at 40 kHz, so a commercial phase sensitive detector was used instead of the mod/demod circuit. The lasers were then modulated at 2.2 kHz, which provided slower but reliable feedback.

3.2 Vacuum system

Achieving a pressure of 10^{-9} mbar or less requires careful assembling of the vacuum parts and powder-free latex gloves should be used to handle the equipment to make sure that no grease is deposited inside the system since grease would limit the quality of the vacuum. The vacuum system used in the experiment, depicted in Figure 3.8, comprises:

1. a glass cell, where the atoms are trapped,
2. a Varian ion pump
3. a valve (enabling the use of a roughing vacuum pump, as explained later),
4. a feedthrough (to dispense Rb vapour in the system),
5. a window (for probing),
6. a five-way cross (putting all parts together)

After the system was carefully assembled, its pressure was taken down to 10^{-6}mbar with a roughing turbo pump whilst heated up to about 350^{o}C

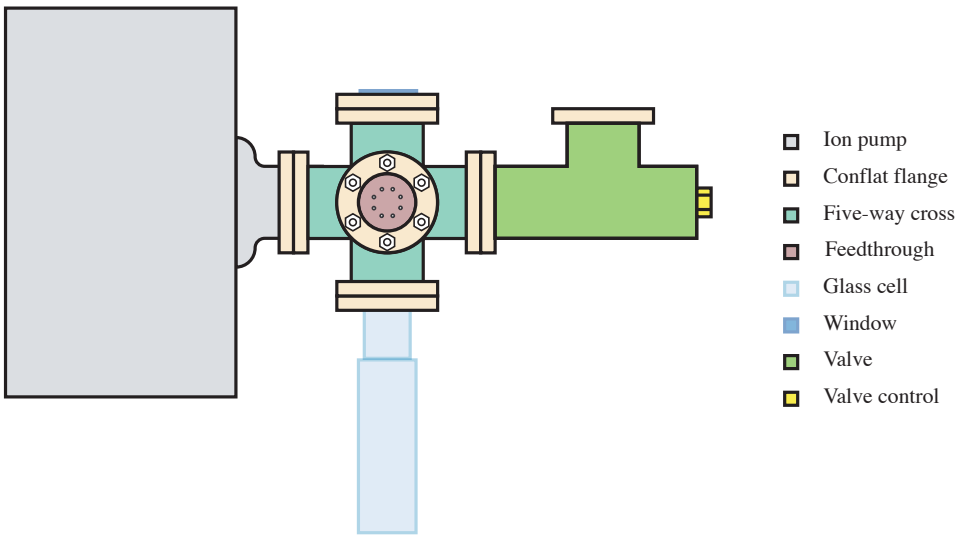

Figure 3.8: The vacuum system

to speed up the outgassing of the walls of the metallic parts. The baking and pumping equipment was borrowed from the group of Photonics at the University of Strathclyde where we were also provided with some invaluable help.

The vacuum system was first connected to the open valve, and then wrapped in aluminium foil to ensure thermal insulation. Particular care was taken wrapping the seal between the glass cell and the metal flanges: too large a thermal gradient in this area could cause irreversible damage to the seal. Thermistors were slid below the foil to monitor temperature and ensure its uniformity. Heating tape was wrapped around the system, more layers of aluminium foil were wrapped around it and a layer of ceramic wool provided insulation from room temperature.

The roughing pump was switched on and the temperature was slowly raised at the safe rate of 1°C per minute, controlling the temperature gradients, especially between the glass cell and the five-way cross. A mass spectrometer, attached to the roughing pump, was used to analyse the composition of the enclosed gas and check for any traces of grease.

After baking and pumping, the system was taken back to Glasgow University where the ion pump was switched on, finally reaching a pressure of 10^{-9} mbar.

3.3 Trapping and stray magnetic field compensation coils

The trapping magnetic field gradient was optimised empirically to about 10 gauss/cm [LSW92], which is easily obtained with coils in the anti-Helmholtz configuration (parallel coils with opposite currents), with about $N = 100$ turns, 10 cm diameter and run with a current of $I = 1$ A to $I = 2$ A. The trapping coils built for this experiment have 130 turns, and were run with $I = 1.8$ A.

Similarly, as the stray fields never exceed a few gauss, Helmholtz (parallel coils with equal currents) coils can be used to compensate them. Given the tight configuration of the vacuum system and the large size of the glass cell, it was convenient to use circular coils for trapping and rectangular coils for compensation.

The Taylor expansion of the spatial variation of the generated magnetic field is given to zeroth order in cartesian coordinates by Equation 3.6 for Helmholtz rectangular coils [Arn99] and to third order in cylindrical coordinates by Equation 3.7 for anti-Helmholtz circular coils [Pec52]. See Figures 3.9 and 3.10 for definitions of $\{a, b, c\}$ and $\{s, r, h, d\}$, and dimensions used in the experiment.

The stray magnetic fields were measured with a Hall effect probe in order to estimate the required number of turns and current for each pair of coils. The fields were measured on each side of the glass cell for each direction ($\{x, y, z\}$ as defined in Figure 3.9) so as to estimate the actual magnetic field field at the centre of the trap. The measured stray fields and the corresponding currents for coils with $N = 30$ turns, are given in Table 3.1.

Table 3.1: Measured stray magnetic fields in each direction (as defined in Figure 3.9), and corresponding coil currents. Note that the actual value of the magnetic field at the centre of the trap cannot be accessed due to the presence of the cell. Assuming the field varies monotonously within the cell, its value in each direction is bound by the values measured on each side of the cell.

Direction	Measured **B** (gauss)	Coil current (A).
x	[0.35; 0.23]	[0.084; 0.128]
y	[-2.69; -1.30]	[0.491; 1.016]
z	[2.17; 2.88]	[0.908; 1.206]

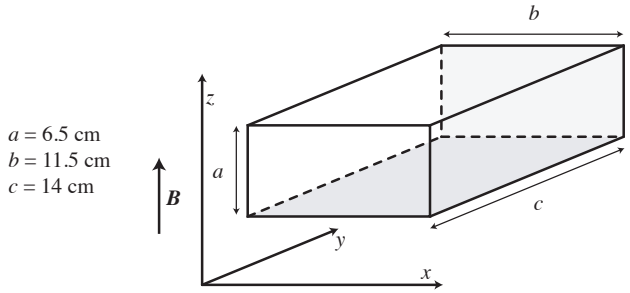

Figure 3.9: Rectangular coils.

$$\mathbf{B} = \frac{8NI}{5} \frac{ab\left(a^2+b^2+c^2\right)}{\left(a^2+b^2\right)\left(b^2+c^2\right)\sqrt{a^2+b^2+c^2}} \begin{pmatrix} 0 \\ 0 \\ 1 \end{pmatrix} \tag{3.6}$$

$$\mathbf{B}\left(r,z\right) = B_1 \begin{pmatrix} -r/2 \\ z \end{pmatrix} + B_3 \begin{pmatrix} \frac{3r^3}{8} - \frac{3r^{2z}}{2} \\ z^3 - \frac{3r^2 z}{2} \end{pmatrix}, \tag{3.7}$$

with $B_1 = \frac{24\pi NId^2 s}{5(d^2+s^2)^{5/2}}$ and $B_3 = \frac{16\pi NId^2 s\left(4s^2-3d^2\right)}{(d^2+s^2)^{9/2}}$.

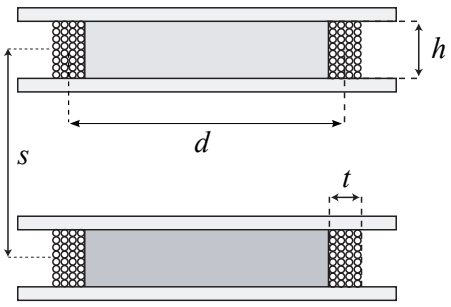

Figure 3.10: Circular coils.

For the magnetic field gradient to be constant to fifth order (true anti-Helmholtz), the diameter of anti-Helmholtz circular coils must be equal to $2/\sqrt{3}$ times their separation, and for a constant field to fourth order, true rectangular Helmholtz coils are obtained when $c = 0.5445a$.

The trapping coils also have to be designed with a fast switching time $\tau = L/R$ if the envisaged experiment is sensitive to magnetic fields. The inductance of a circular multilayer coil with average radius $d/2$, thickness t and height h is approximately [Whe28]:

$$L = \frac{(d/2)^2 N^2}{38.0d/2 + 28.6h + 31.7t} \tag{3.8}$$

Given their dimensions (see Figures 3.9 and 3.10) our trapping coils have an inductance $L = 6\,\mathrm{mH}$, and with a measured resistance of $R = 2.2\,\Omega$, they can be switched in $\tau = 2.7\,\mathrm{ms}$.

3.4 Characterisation of the trap

3.4.1 Fluorescence measurements

Measuring the fluorescence from the trapped atoms provides an easy way of estimating the number of atoms in the trap, the trap loading time and the saturation intensity of the trapped atoms. The fluorescence from the trapped atoms is collected by a lens of numerical aperture NA = 0.14, yielding a ratio of collected light and emitted light $(\mathrm{NA}/2)^2$. The light is

focused on a large area photodiode of responsivity $\eta = 0.6\,\mathrm{A/W}$, with a gain resistor of $1\,\mathrm{M\Omega}$. Given that the absorption rate per atom is:

$$R = \frac{\Gamma}{2}\frac{I_{tot}/I_S}{1 + I_{tot}/I_S + 4\Delta^2/\Gamma^2}, \tag{3.9}$$

the photocurrent ι is thus given by:

$$\iota = N\eta\frac{hc}{\lambda}\left(\mathrm{NA}/2\right)^2\frac{\Gamma}{2}\frac{I_{tot}/I_S}{1 + I_{tot}/I_S + 4\Delta^2/\Gamma^2}. \tag{3.10}$$

The background subtracted photodiode signal was 544 mV. Given that $\Delta = 13\,\mathrm{MHz}$, $I_{tot}/I_{sat} = 3.6$, the number of atoms was then evaluated to $N = 8 \times 10^8$. An approximate trapping volume of $\frac{4}{3}\pi r^3 = 0.5\,\mathrm{cm}^3$ corresponding to $r = 5\,\mathrm{mm}$, gives a density $n_{Rb} = 1.5 \times 10^9\,\mathrm{cm}^{-3}$. However, this is an underestimate of the density in the area of the centre of the cloud since the distribution is not uniform.

The trap loading time was measured by blocking one of the beams and unblocking it rapidly. A fit of the data gives a time constant $\tau = 0.3\,\mathrm{ms}$ (Figure 3.11), a figure that varies as a function of the Rubidium background pressure.

Recall from Chapter 2 that the collisional cross-section of the atoms σ_{Rb} can be calculated either from the number of atoms or from the loading rate (Equation 2.12). Estimating the capture velocity to be $10\,\mathrm{m/s}$, the thermal Rubidium mean velocity to $v_{th} = 340\,\mathrm{m/s}$, and the trapping radius r to $5\,\mathrm{mm}$, one obtains:

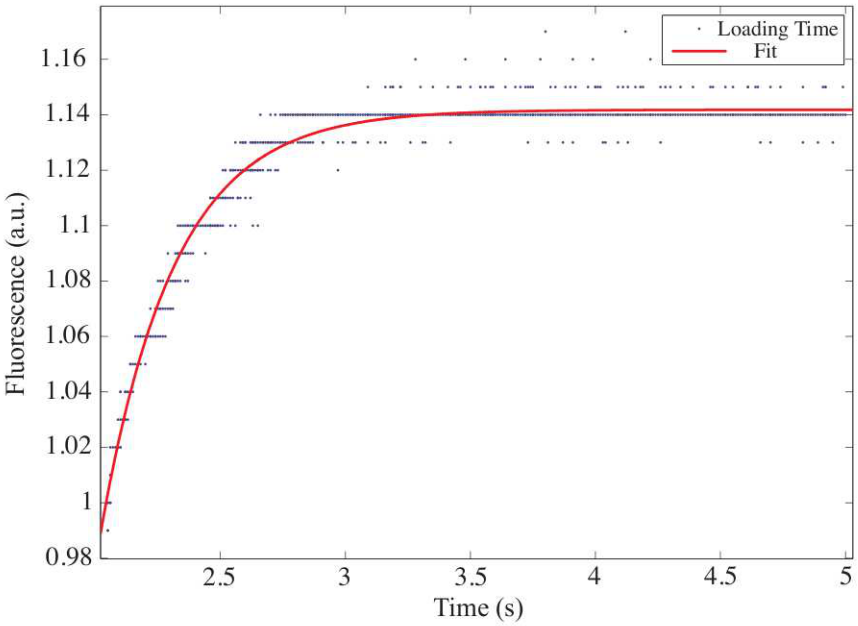

Figure 3.11: Trap Loading Time.

$$\sigma_{Rb} = \frac{3}{4\left(\frac{v_c}{v_{th}}\right)^4}\frac{4\pi r^2}{N} = 1.2 \times 10^{-13}\,\mathrm{m}^{-2} \tag{3.11}$$

$$\sigma_{Rb} = \frac{1}{\tau n_{Rb} v_{th}} = 6.5 \times 10^{-13}\,\mathrm{m}^{-2} \tag{3.12}$$

The factor of 5 between the two values is likely to be due to the crude estimates of the density and of the trapping volume.

Another measurement that can be made using fluorescence is the actual saturation intensity of the atoms. Recall that the light used to trap the

atoms is circularly polarised and carries spin angular momentum. Over a few absorption-spontaneous emission events, the atoms are driven to the states with highest absolute angular momentum (largest $|m_F|$, see Appendix A). The high angular momentum states have a larger dipole moment than the low angular momentum states, so the average dipole moment of the atoms in the trap is higher than the transition average [Arn99]. The saturation intensity is proportional to the square of the dipole moment, so the average saturation intensity is also increased. By switching the amount of trapping light rapidly (faster than the loading time of the trap so that the average number of atoms over the measurement stays constant) and measuring the fluorescence ratio $\frac{F_1}{F_2}$, one can estimate the trap saturation intensity:

$$\frac{F_1}{F_2} = \frac{I_1}{I_2}\frac{1 + I_2/I_S + 4\Delta^2/\Gamma^2}{1 + I_1/I_S + 4\Delta^2/\Gamma^2} \tag{3.13}$$

The estimated saturation intensity in our trap is about $1.86 \pm 0.05\,\mathrm{mW/cm^2}$ (compared to the $1.67\,\mathrm{mW/cm^2}$ of the transition average).

3.5 Summary and outlook

The magneto-optical trap successfully built at in the group of Optics produced trapped vapours of a density $n_{Rb} \geq 1.2 \times 10^9\,\mathrm{cm^{-3}}$ and containing around 8×10^8 atoms. Measuring the absorption of a probe beam through

the cloud would give a far more accurate measurement of the atom density than that obtained by fluorescence. It would also enable the spatial distribution of the atoms to be monitored by imaging the probe onto a CCD camera.

The temperature of the atomic cloud has yet to be measured. This can be done using the method called "release and recapture" (R&R). The R&R method consists of releasing the atoms from molasses and recapturing them after a delay τ that can be varied. The delay-dependent ratio of recaptured atoms $N_r(\tau)/N_T$ gives the velocity distribution of the cloud, which can be fitted to a Maxwell-Boltzmann distribution to deduce the temperature.

Optical molasses should be realised in the near future as they would facilitate the investigation of phase-dependent processes in cold atoms. Indeed, the spatial dependence of the Zeeman shifts induced by the trapping coils would add complexity to the measurements and interpretation. The longer experimental time window optical molasses allow due to their lower temperature is also useful for all experiments investigating information storage.

3.6 References

[Arn99] A.S. Arnold. Preparation and Manipulation of an ^{87}Rb Bose-Einstein Condensate. PhD thesis, University of Sussex, 1999.

[AWB97] A.S. Arnold, J.S. Wilson, and M.G. Boshier. A simple extended-cavity diode laser. Review of Scientific Instruments, 60(3):1236–1239, 1997.

[LSW92] K. Lindquist, M. Stephens, and C. Wieman. Experimental and theoretical study of the vapor-cell zeeman optical trap. Physical Review A, 46:4082–4090, 1992.

[MSW92] K.B. MacAdam, A. Steinbach, and C. Wieman. A narrow-band tunable diode laser system with grating feedback, and a saturated absorption spectrometer for cs and rb. American Journal of Physics, 60:1098–1111, 1992.

[NDA99] L. Nilse, H.J. Davies, and C.S. Adams. Synchronous tuning of extended cavity diode lasers: The case for an optimum pivot point. Applied Optics, 38:548–553, 1999.

[Pec52] E.R. Peck. Electricity and Magnetism. McGraw-Hill, New York, 1952.

[WH91] C.E. Wieman and L. Hollberg. Using diode lasers for atomic physics. Review of Scientific Instruments, 62:548–553, 1991.

[Whe28] H.A. Wheeler. Simple inductance formulas for radio coils. Proceedings of the I.R.E., 1928.

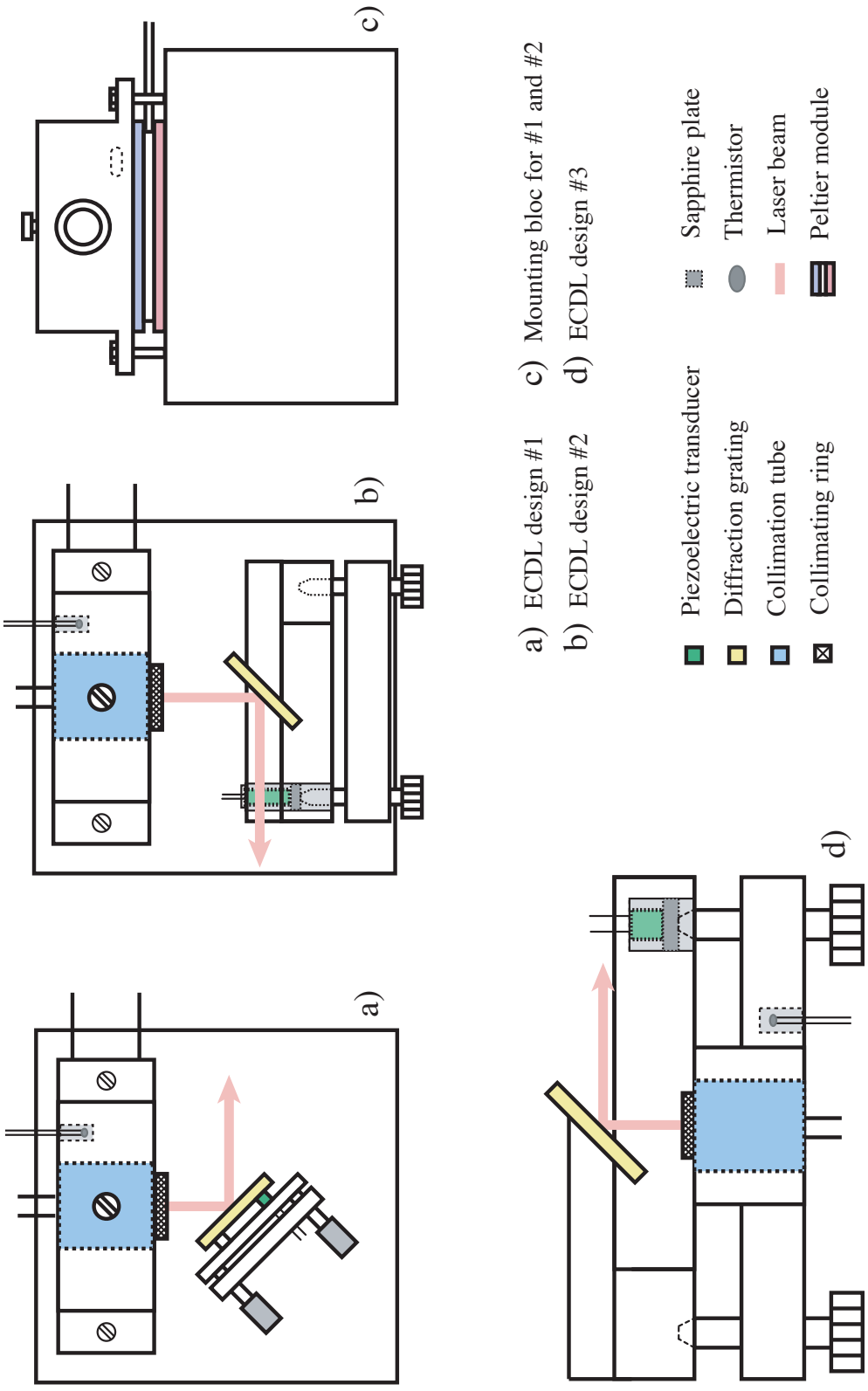

Figure 3.12: ECDL designs.

CHAPTER 4

Generation of 420 nm light via four-wave mixing: the "blue light" experiment

In any medium, whether atomic, molecular or crystalline, coherent emission of radiation can only take place if the emitted field interferes constructively with the excitation field. This means that the phase acquired after a round trip of a closed transition scheme must be zero. In the particular case of four-wave mixing, the four waves $\{k_1, k_2, k_3, k_4\}$ with their associated refractive indices $\{n_1, n_2, n_3, n_4\}$ have to be phase-matched, yielding the condition $\Delta k = n_1 k_1 + n_2 k_2 - n_3 k_3 - n_4 k_4 = 0$. This phase-matching condition can also be interpreted as a conservation of momentum, depicted in Figure 4.1.

Phase coherence (conservation of the phase in a process) and phase dependence are in fact two aspects of the same physical phenomenon: the interference of probability amplitudes. A system exhibiting phase coherence may thus also show signatures of phase dependence. Though it was mentioned in the introduction that cold atomic vapours were particularly suitable to the study of coherent phenomena, cooling the vapour is not always necessary. Four-wave mixing is frequently studied in hot vapours (room temperature to ≈150°C [CCW81, MSS84, IL$^+$88, MBAL07, RCH09]) as the timescale of the nonlinear process is a lot shorter than the diffusion time of the atoms.

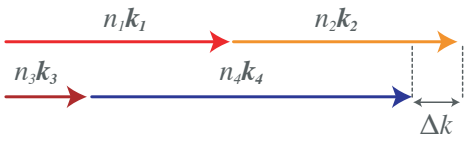

Figure 4.1: Phase mismatch in a four-wave mixing process

Degenerate four-wave mixing was first pursued in Sodium vapours [KTPG85, BLE78] following a proposed experiment by Hellwarth in 1977 [Hel77] to generate phase-conjugate fields. Four-wave mixing also elicited interest for the generation of two-photon coherent states [Yue85] and squeezed states of light [RW85, MKS87]. Experiments for frequency upconversion via multiwave mixing were proposed [Duc85, Man87], and realised [CCW81, MSS84, IL$^+$88] in the 1980s.

The accessible level structure of Rubidium makes this atom ubiquitous in atom optics experiments, and the first four-wave mixing experiment using Rubidium vapours was a conversion of phase variation into intensity variation of a conjugate wave, published in 1992 by G. Grynberg et al. [GPPV92]. Since then, many interesting phenomena have been observed such as the enhancement of non-degenerate four-wave mixing based on EIT [LX96], strong intensity squeezing [MBAL07], and quantum interference in four-wave mixing [VNMT98]. In 2002 Zibrov et al. [ZLHS02] measured 420 nm (blue) light emitted from a hot Rubidium vapour resonantly pumped with 780 nm and 776 nm light to $6D_{5/2}$ as shown on Figure 4.2, a study that was furthered in 2006 by Meijer et al. [MWS+06] and that the group of Photonics at the University of Strathclyde undertook in 2005. This experiment proved of particular interest, since as well as being a closed, thus phase-dependent system [BBK+86, MFAO02, KSMFAO07] (see also Chapter 1), it also provided the opportunity to generate a narrow source of blue light. Blue lasers, even considering the recent advances of laser diode technology are indeed still difficult to obtain cheaply and efficiently as the cost of a 5 mW blue extended cavity diode laser would typically be about £14 000 [cs]. The development of an affordable, tuneable, narrow source of blue light is thus still a technologically relevant challenge.

In order to carry out experimental research in the field of phase-dependent atomic processes, I was invited to work for six months on Dr. Aidan Arnold’s “blue light” setup at the University of Strathclyde. The

aim of the project was to study the four-wave mixing process further and investigate the possible signatures of its phase dependence. This collaboration between the group of Photonics and the group of Optics was supervised by Dr. Arnold for the experimental part, Dr. Franke-Arnold for the theory, and benefitted from Prof. Riis' and Dr. Franke-Arnold's guidance. During the first few months of my participation I worked with Mr. Simon Clark, who worked on the experiment in the framework of his fourth year undergraduate project. The experiment itself was started in 2005 by Dr. Arnold and Mr. Nathan Paterson. My contribution to this work was first defined as a study of the up-conversion efficiency and its phase dependence, but the richness of the observed behaviours led us to making measurements to refine our understanding of the atom-field interaction and find clues towards a theoretical model (Chapter 5).

Four-wave mixing requires conservation of energy, momentum, and a nonzero third order susceptibility of the medium (see p. 12 of Ref. [Boy03]). These experimental requirements predefined some of the measurements that had to be done to identify the emitted blue light as a result of four-wave mixing.

First of all, the beam could only be generated if the beams were co-propagating, which indicated the importance of momentum conservation. From phase-matching considerations, it was ventured that misalignment of the pump beams should result in the generation of a cone, as demonstrated in [MGB85]. A simple example is useful to illustrate this statement: im-

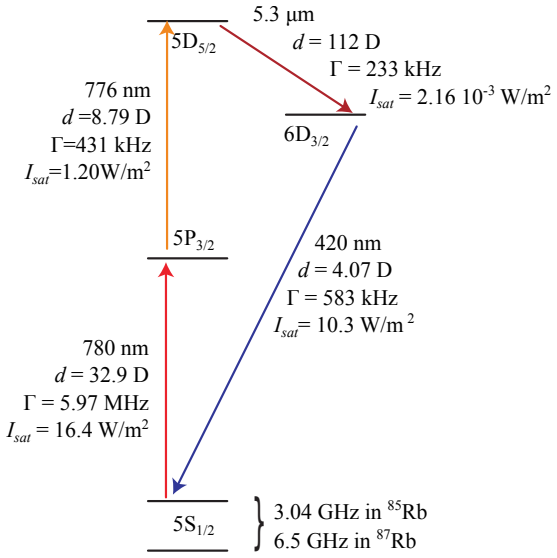

Figure 4.2: Pumping scheme in Rb.

posing a small angle between $\underline{\mathbf{k_{780}}}$ and $\underline{\mathbf{k_{776}}}$ in the perfectly phase-matched case in which $n_{780}k_{780}+n_{776}k_{776}-n_{IR}k_{IR}-n_{420}k_{420}=0$ leads to a new set of solutions. The new $\underline{\mathbf{k_{IR}}}$ and $\underline{\mathbf{k_{420}}}$ possess a constant angle and a cylindrical symmetry with respect to the axis of propagation thus generating a cone of light. This phenomenon was however never observed in the Strathclyde blue light experiment. As $k_{IR} \ll k_{420}$, it may be envisaged that only an angle between $\underline{\mathbf{k_{IR}}}$ and $\underline{\mathbf{k_{420}}}$ approaching 90° would allow the observation of a cone of emission. As we shall see in the next chapter, propagation of the 5 μm radiation seems central to the blue light generation, and such a large transverse component of $\underline{\mathbf{k_{IR}}}$ might not allow a sufficient propagation length for the 420 nm radiation to be generated.

Since the third order polarisation of the atomic medium depends on the frequency of the input beams, and increases with the product of the amplitudes of the pump beams, we measured the output blue light power as a function of the 776 nm and 780 nm powers and detunings.

A polarisation dependence of the process was not to be ruled out since Rubidium atoms possess hyperfine structure, and in the following study the impact of input beam polarisation on the conversion efficiency was assessed. As shown further into this chapter, the polarisation of the input beams in fact proved crucial to the efficiency of the up-conversion.

Unsurprisingly the conversion efficiency is also a function of the Rubidium density: too small a density limits the gain, conversely a very large density leads to a very large absorption of the beams in regions where the intensity of the pumps is not sufficient to induce gain on the 420 nm transition. This generates more fluorescence and less coherent light, as verified experimentally.

The linewidth of the blue beam, as well as being interesting for what it reveals about the effects taking place in the vapour, is also central to practical applications of the setup as a coherent light source. After the end of my contribution to the experimental work, the blue beam linewidth was measured by Dr. Arnold and Prof. Riis with a Fabry-Pérot etalon to be less than or equal to 4 MHz, the linewidth of the etalon.

Throughout this investigation, only the blue beam could be measured since the transmission of the BK7 cell at 5 μm is negligible. Measuring the

transverse structure and the power of the 5 μm beam would provide valuable information to complete the model presented in Chapter 5 as well as the investigation on transfer orbital angular momentum transfer in four-wave mixing presented in Chapter 6.

This chapter presents the optical setup and the experimental results of the measurements mentioned above. Some elements of explanation will be given, but for a more in-depth analysis see Chapter 5. All data extracted from Ref. [VFARA10] were taken by Dr. Arnold after the end of my time on the experiment.

4.1 Experimental setup

The simplicity of this experimental setup belies the complexity of the interaction between a single species of atom and near-resonant light. Indeed, the experiment mainly consists of two co-propagating and overlapped laser beams which get converted to a beam of blue light upon propagation in a hot cell of Rubidium gas (Figure 4.3). The pump beams are tuned to 780 nm and 776 nm, near the two-photon resonance of the $5S_{1/2}$ to $5D_{5/2}$ transition of Rubidium. These two beams are generated by two extended cavity diode lasers (ECDLs, see Section 3.1): the 780 nm laser was built by the group of Photonics at the University of Strathclyde [AWB97] with a similar design to that described in Section 3.1.1, and the 776 nm laser is a Toptica DL100. The two designs generate beams with similar waists and

comparable astigmatism.

The pump beams were overlapped at a polarising or non-polarising beamsplitter, according to the measurement we performed, and weakly focused ($f = 12.5\,\text{cm}$) into a Rubidium cell kept around 120°C. This temperature was measured from an absorption measurement, yielding a Rb vapour pressure of $9 \times 10^{-4}\,\text{mbar}$, nearly 10 000 times higher than the pressure at room temperature, which was found to be the best compromise between nonlinear conversion and pump absorption for the available pump power. The efficiency of blue light generation was relatively independent of pump beam focusing since changing the focal length of the lens from 12.5 cm to 40 cm only reduced the conversion efficiency by 25% [VFARA10]. The blue beam was separated from the pump beams using a dichroic mirror and measured with a photodiode. For the optimum temperature, pump beam focusing and polarisation, a maximum blue beam power of 1.5 mW was observed.

4.2 Measurements

The method we used to find the frequency region of blue light generation consisted in scanning the 780 nm beam across the ground state doublet using the saturated absorption spectroscopy module, and to shift the 776 nm frequency whilst monitoring it with a wavemeter. The detuning of the 776 nm beam was then finely adjusted by delicately changing the grating

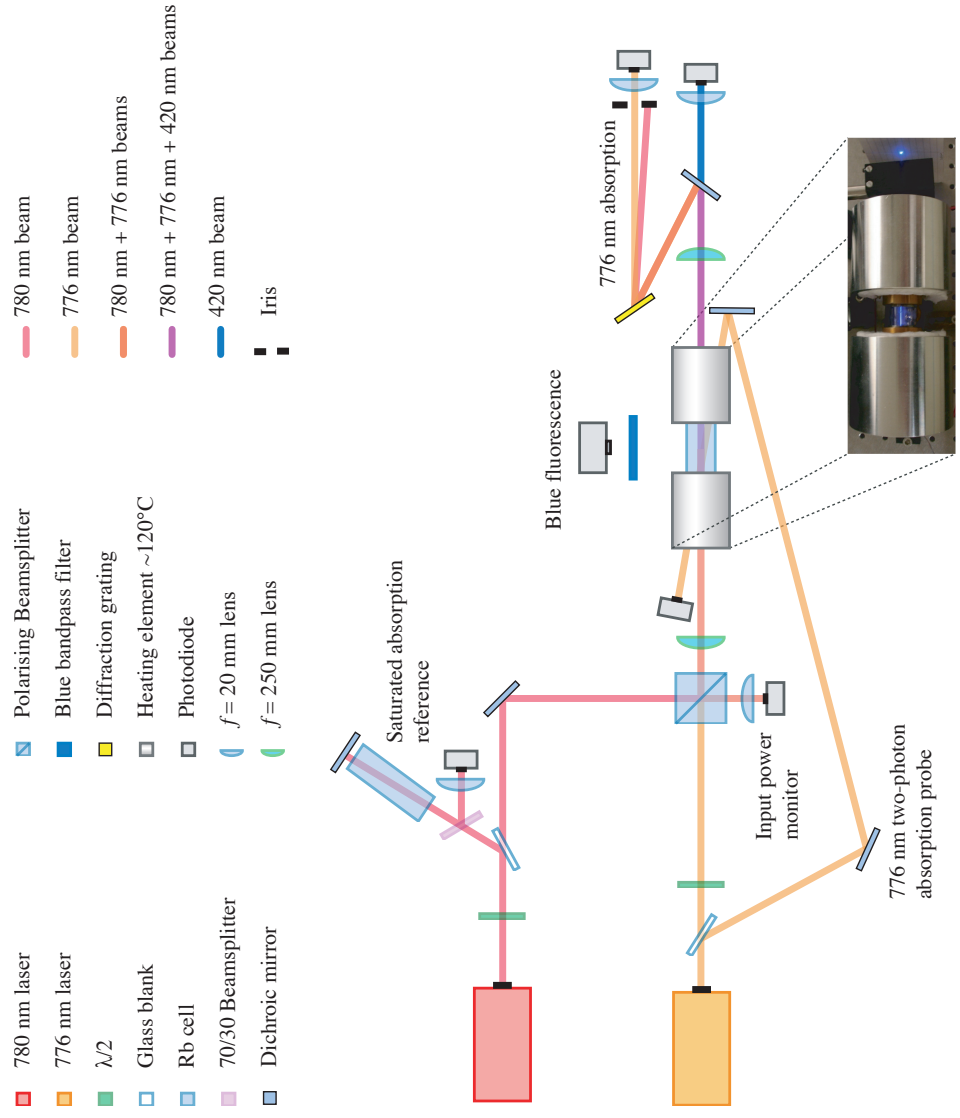

Figure 4.3: Experimental setup.

angle by hand and finding the laser driving current yielding the largest mode-hop free scanning range. Monitoring the absorption of the beam in a saturated absorption spectroscopy setup allowed to ensure that the 780 nm laser was running at a single frequency. The shape and depth of the absorption dips are indeed altered when the laser is running on several longitudinal modes as only a fraction of the power is resonant with the atoms, and this fraction can also be frequency-dependent.

The output mode of the 776 nm laser was regularly checked with a Fabry-Pérot etalon. After the end of my participation to the experimental project Dr. Arnold measured the two-photon absorption by performing two-photon saturated absorption spectroscopy as a reference for the absolute frequency of the 776 nm. This was done by overlapping the probe beam with the pump beams at the entrance of the cell (as shown on Figure 4.3). Once the coherent emission of blue light was established and coarsely optimised, the single mode quality of the 776 nm laser could also be checked by scanning the 780 nm frequency and changing the driving current of the 776 nm diode. A frequency shift without any change in the shape of the blue light emission spectrum provided a good indication of a single mode 776 nm laser. The conversion efficiency was then optimised with respect to the pump beams' frequency, power and state of polarisation, and Rubidium vapour pressure.

4.2.1 Dependence on driving field powers

A polarising beamsplitter cube was used to overlap the two pump beams to vary the input power irrespective of the laser frequency. The power dependence was determined by fixing the frequencies of the beams at their optimum value for the highest available pump powers, and for a temperature of about 120°C, estimated from the absorption of a resonant 780 nm beam through the hot cell. Note that though informative, this method of studying the input power dependence of the conversion efficiency is not rigorous as the two-photon resonance condition for the 776 nm beam, and hence the optimal 776 nm frequency, depends on the power of the 780 nm beam (Chapter 5). The expected discrepancy between this method and the more tedious but more exact method which would consist in adjusting the 776 nm frequency for each value of 780 power is however difficult to estimate since very strong propagation effects critically modify the frequency dependence of the conversion efficiency for high vapour pressure. Figure 4.4 shows the output blue power as a function of the 780 nm power (red) and the 776 nm beam power (black) for the maximum power of the beam kept constant. The red plus on the graph shows the position of the best conversion efficiency $\eta = \frac{P_{420}}{P_{780}P_{776}} = 2.6 \times 10^{-3}\,\mathrm{mW}^{-1}$.

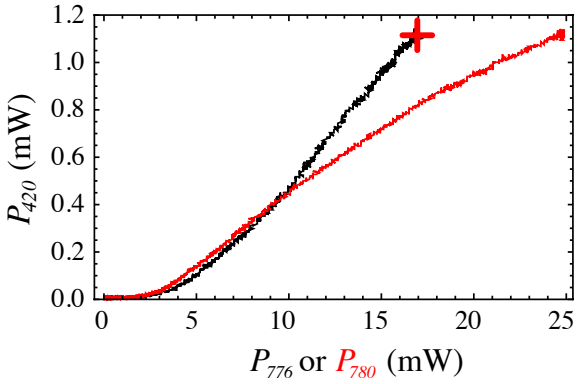

Figure 4.4: Power dependence of blue light generation. From Ref. [VFARA10]. Each curve was taken keeping the constant beam at its maximum power.

4.2.2 Frequency dependence of coherent blue light and fluorescence

A systematic study of the frequency sensitivity of the conversion efficiency was probably the most important measurement to perform if we were to model and understand the system. For this purpose, the 780 nm laser frequency was scanned continuously and the 776 nm laser was shifted by steps of about 100 MHz yielding a scan of about 8 GHz over about 70 points. The two graphs in Figure 4.5 show blue light power as a function of 780 (x-axis) and 776 (y-axis) laser frequencies for low Rubidium pressure, around 100°C (left) and for optimum Rubidium pressure (right). The temperature was determined by Dr. Arnold by fitting the absorption of a 780 nm probe through the cell and fitting the data to the model given in Ref. [SAGH08]

The loci of two photon absorption were estimated by monitoring the absorption of a counterpropagating 776 nm probe (see probe experimental setup on Figure 4.3) showing Doppler-free saturated absorption features on two-photon resonance. The dots on the graphs correspond to local absorption minima.

For the optimum Rb pressure a sharp peak of up to 1.5 mW of blue light is observed for $\delta_{780} = 1.6\,\text{GHz}$ and $\delta_{776} = -1.6\,\text{GHz}$. Less blue light is observed for lower pressure, but the frequency range over which it can be generated is greatly increased, and confined along the lines of two-photon resonance (for an analysis of the effects giving rise to the change of behaviour, see Chapter 5). As the temperature is increased, the density of Rb atoms is also increased, which enhances the effect of propagation such as phase matching and 420 nm reabsorption due to pump depletion. For the corresponding theoretical analysis, see Chapter 5.

The importance of two-photon resonance is clear considering that the ratio of decay rates of levels $5D_{5/2}$ and $6P_{3/2}$ is about 0.4 (Table 4.2.2), which allows population inversion. In the next chapter it will be shown that this population inversion may be at the root of the onset of the four-wave mixing process.

4.2.3 Vapour pressure

The Rubidium temperature was controlled with heating elements (see Figure 4.3), and measured with a thermocouple. An increase of the conver-

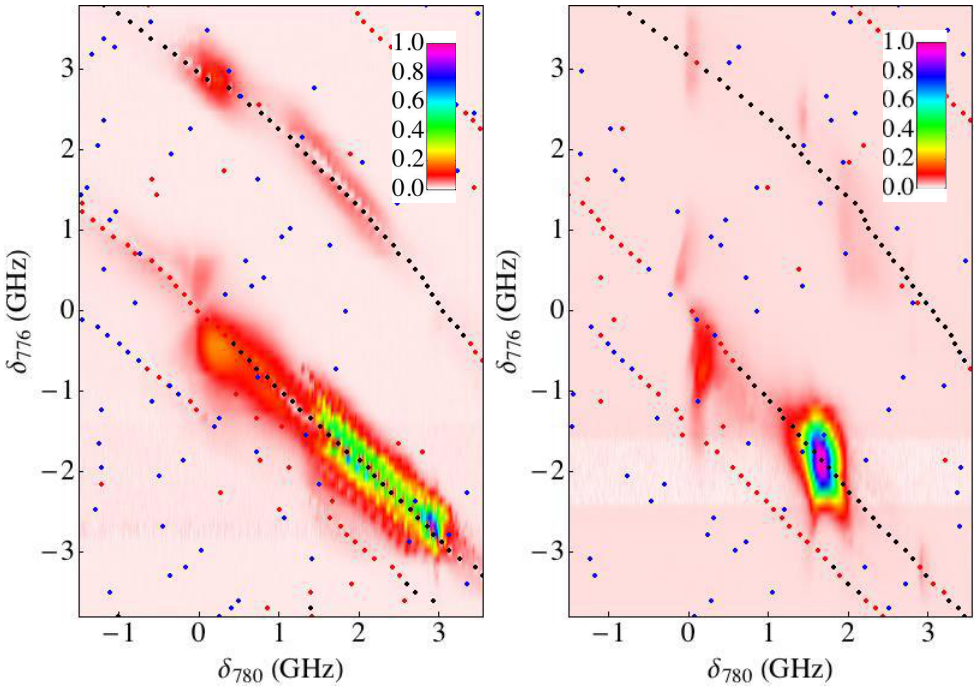

Figure 4.5: Frequency dependence. Left: $P_{Rb} = 10^{-4}$ mbar. Right: $P_{Rb} = 9 \times 10^{-4}$ mbar. The data was normalised, and the interpolation between the data points is linear. From Ref. [VFARA10].

sion efficiency is observed when the cell temperature is raised from 20 °C ($P_{Rb} = 2 \times 10^{-6}$ mbar, conversion from Ref. [Nes63]) where nearly no blue light is generated, to about 120°C ($P_{Rb} = 1.2 \times 10^{-2}$ mbar) where up to 1.5 mW of blue light is generated. The efficiency then decreases back to zero, and some ionization (visible as a very bright white spot at the entrance of the cell) was observed when the temperature was raised to over 170°C ($P_{Rb} \geq 10^{-2}$ mbar). Figure 4.6 shows the plot of photodiode signal as a function of thermocouple temperature. Note that because of tempera-

Table 4.1: Spectroscopic and physical data for the relevant transitions in blue light. Transition frequencies and decay rates from [RKRT08] and [KB95]

Transition	λ (nm)	Γ (kHz)	d (debye)
$5S_{1/2} \rightarrow 5P_{3/2}$	780.2414	6604	32.9
$5P_{3/2} \rightarrow 5D_{5/2}$	775.97855	431	8.79
$6P_{3/2} \rightarrow 5D_{5/2}$	5200	233	112
$5S_{1/2} \rightarrow 6P_{3/2}$	420.2976	583	4.07

ture inhomogeneities, the actual cell temperature in the interaction region is lower than that shown on the plot. The actual vapour temperature was later measured by absorption of a 780 nm probe through the cell showing a maximum of blue light generation for T=120°C.

When the Rubidium density is lower than its optimum value, increasing the temperature results in an increase of the density and therefore of the conversion efficiency. The conversion efficiency increases until the reabsorption of the blue light at the end of the cell (where the 780 nm and 776 nm intensities are too low to induce gain on the 420 nm transition) becomes significant. These two effects result in an overall bell-shaped curve.

4.2.4 Polarisation dependence

Considering the hyperfine structure canopy of Rb atoms (Figure 4.7), we were interested in knowing whether the polarisation of the pump beams had any effect on the conversion efficiency. The polarising beamsplitter was replaced with a non-polarising beamsplitter 4.3 and a quarter-wave plate was

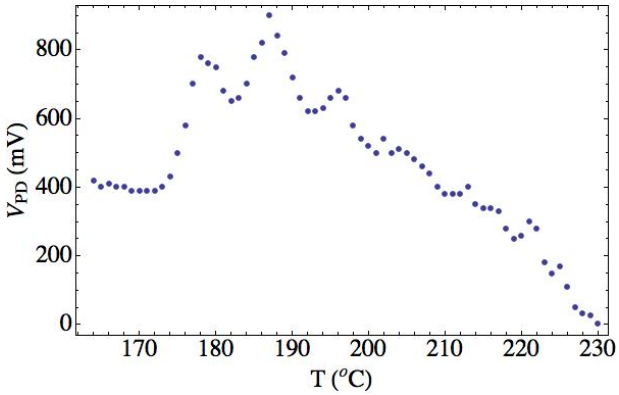

Figure 4.6: Blue light power vs. temperature measured with a thermocouple placed at the surface of the cell. *Note that the temperature plotted here is an overestimate of the actual vapour temperature as the optimum temperature was later measured by absorption to be* $\approx 120^\circ C$.

added just before the hot cell. Half the power was thus systematically lost, but this allowed to set arbitrary pump beam polarisation. The frequencies and Rubidium pressure were set for optimal blue light generation. The results of the various polarisation combinations are compiled in Table 4.2 and given as a ratio with respect to the highest yielded power. The conversion efficiency is largest for co-circular polarisation of the input beams and is inhibited by a factor of 500 for counter-circular polarisations.

Despite the striking contrast between the two opposite cases, there is no simple explanation for this behaviour. A possible model to investigate this effect is outlined at the end of Chapter 5. The presence of a stray magnetic field displacing the magnetic sub-levels due to the Zeeman effect may explain the discrepancy between the two. It is however clear that

co-circular polarisation favours four-wave mixing. Driving the atoms with $\{\sigma_+, \sigma_+\}$ pumps the atoms to the stretched states, yielding the closed circuit of transition depicted in Figure 4.7.

It is worth noting that the stray magnetic fields in this experiment were not cancelled, and that no strong magnetic field was imposed to define a major quantisation axis. Interestingly, a very similar study [AMSH09] was published whilst the work presented here was under review for publication. The authors of Ref. [AMSH09] report a significantly lower contrast whereby the counter-circular beams only inhibit the conversion by a factor of 10. The difference in contrast could be explained by a difference of the magnitude and direction of stray magnetic fields between the two experiments. An investigation of the polarisation dependence as a function of the direction of an imposed magnetic field setting a main quantisation axis would be particularly relevant, and should be realised in the near future.

Table 4.2: Polarisation dependence of blue light generation, relative to highest yield (obtained with co-circular pumps $\{\circlearrowright, \circlearrowright\}$ or $\{\circlearrowleft, \circlearrowleft\}$)

Polarisation	$\leftrightarrow$	$\updownarrow$	$\circlearrowleft$	$\circlearrowright$
$\leftrightarrow$	.53	.31		
$\updownarrow$	.31	.53		
$\circlearrowleft$			1	2×10^{-3}
$\circlearrowright$			2×10^{-3}	1

It is also instructive to look at a 780 nm laser scan of the blue light beam and fluorescence for different combinations of pump beams polarisations,

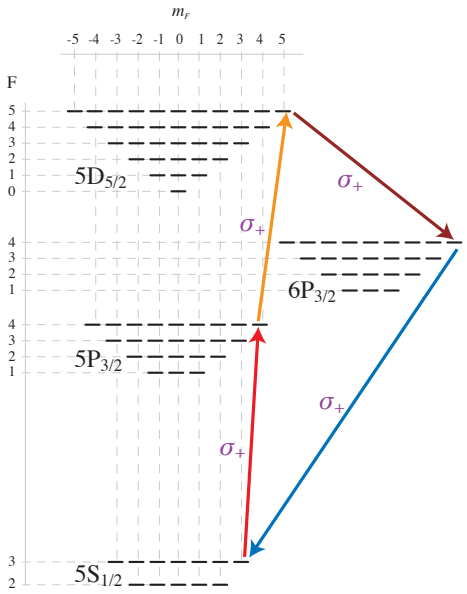

Figure 4.7: Full ^{85}Rb hyperfine structure. Red arrows show that pumping with σ_+ on both pumping transitions yields a closed loop.

as shown in Figure 4.8. The isotropic emission of blue light (fluorescence) stays roughly constant and follows the 776 nm beam absorption whatever the state of polarisation of the pump beams, but the coherent, directional emission shows a dramatic polarisation dependence. The presence of fluorescence and the absorption of 776 nm light show that the system is indeed pumped to the $5D_{5/2}$ level, so the absence of coherent emission suggests destructive interference between the dipole moments of the possible paths on the $5D_{5/2} \rightarrow 6P_{3/2} \rightarrow 5S_{1/2}$ cascade. However this cannot be the full explanation, as pumping the system with linear polarisation leads to the same uppermost hyperfine level as pumping with counter-circular polarisa-

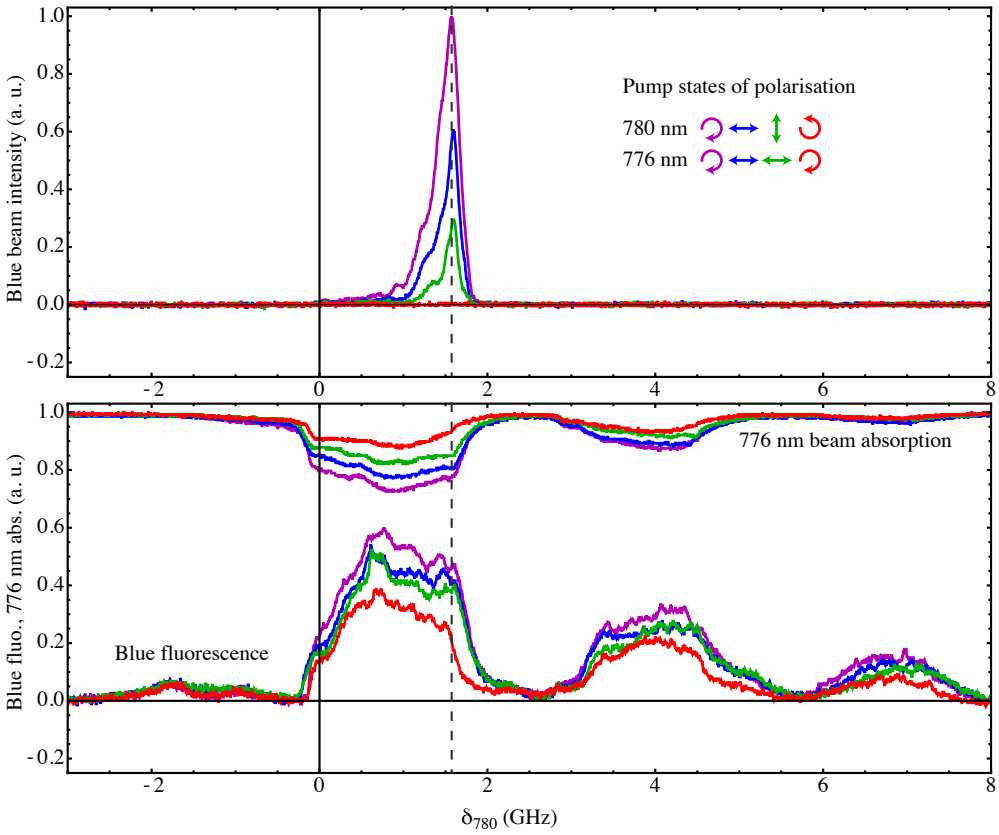

Figure 4.8: Top: blue beam generation for four combinations of pump states of polarisation vs. δ_{780}. Bottom: blue fluorescence and 776 nm beam absorption for all combinations of pump beam polarisations. From Ref. [VFARA10].

tions. These two cases may differ by the optical pumping they induce in the atomic populations. Due to the complexity of the system, this would have to be assessed numerically.

4.3 Summary and outlook

The blue light conversion efficiency was found to depend on the frequency, power and state of polarisation of the pump beams, as well as on the density of the Rubidium vapour. For a Rubidium pressure of about 10^{-4} mbar, the blue light generation follows closely the lines of two-photon absorption. Increasing the Rubidium pressure to 9×10^{-4} mbar reduces the frequency range over which blue light is generated to a few 100 MHz around a 780 nm beam detuning of 1.6 GHz with respect to the upper hyperfine level. As increasing the atomic density leads to an enhancement of all propagation effects (absorption, gain, focussing, defocussing and phase-matching) a number of reasons for the restriction of the frequency range of blue light generation may be envisaged. As a significant amount of focussing and defocussing of the 780 nm beam was experimentally observed in the vapour (see Figure 6.4 of Chapter 6), the reduction of the conversion efficiency could be attributed to the combination of a reduced 780 nm intensity with a degraded 780 nm and 776 nm beam overlap. A study of the impact of phase-matching can be found in the next chapter.

Increasing the Rubidium density initially improves the conversion efficiency, but as the pump beams get depleted, they no longer induce gain on the 420 nm transition. In the absence of gain, the 420 nm beam gets re-absorbed by the vapour. This could be checked experimentally by varying the pump beam power and observing the optimum temperature vary

accordingly.

A surprisingly critical polarisation dependence of the blue light generation was observed as co-circular pump beams generated 500 times more blue light than counter-circular beams. This cannot be explained by two-photon selection rules as this is contradicted by a significant absorption of the 776 nm beam and the presence of blue fluorescence. A possible explanation would be a cancellation of dipole moments on the $5D_{5/2} \rightarrow 6P_{3/2} \rightarrow 5S_{1/2}$ cascade combined with optical pumping. This may be studied by simulating the optical pumping induced by the various combinations of input states of polarisation along with a calculation of the dipole moments of each transition between magnetic sub-levels.

As the observed behaviours proved richer and more complex than we expected, there was a lot to be understood at the end of the six months project. Dr. Franke-Arnold and I took this as opportunity for a dialogue between a working experiment and a model to the study of atom-field interaction. The next chapter presents our attempt at untangling the effects at play within the vapour.

4.4 References

[AMSH09] A.M. Akulshin, R.J. McLean, A.I. Sidorov, and P. Hannaford. Coherent and collimated blue light generated by four-wave mixing in Rb vapour. Optics Express, 17:22861–22870,

2009.

[AWB97] A.S. Arnold, J.S. Wilson, and M.G. Boshier. A simple extended-cavity diode laser. Review of Scientific Instruments, 60(3):1236–1239, 1997.

[BBK+86] S.J. Buckle, S.M. Barnett, P.L. Knight, M.A. Lauder, and D.T. Pegg. Atomic interferometers. Optica Acta, 33:1129–1140, 1986.

[BLE78] D.M. Bloom, P.F. Liao, and N.P. Economou. Observation of amplified reflection by degenerate four-wave mixing in atomic sodium vapor. Optics Letters, 2:58–60, 1978.

[Boy03] R.W. Boyd. Nonlinear Optics. Academic Press. Elsevier Science, second edition, 2003.

[CCW81] R.G. Caro, A. Costela, and C.E. Webb. Resonantly enhanced rare-gas-halide laser frequency up-conversion in Mg vapor. Optics Letters, 6:464–466, 1981.

[cs] Toptica customer services. http://www.toptica.com. Retrieved August 2010.

[Duc85] M. Ducloy. Optical phase conjugation with frequency up-conversion via high order nondegenerate multiwave mixing. Applied Physics Letters, 46:1020, 1985.

[GPPV92] G. Grynberg, A. Petrossian, M. Pinard, and M. Vallet. Phase-contrast mirror based on four-wave mixing. Europhysics Letters, 17:213, 1992.

[Hel77] R.W. Hellwarth. Generation of time-reversed wave fronts by nonlinear refraction. Journal of the Optical Society of America, 67:1–3, 1977.

[IL+88] C.H. Muller III, D.D. Lowenthal, , M.A. DeFaccio, and A.V. Smith. High efficiency, energy scalable, coherent 130 nm source by four-wave mixing in Hg vapor. Optics Letters, 13:651–653, 1988.

[KB95] R.L. Kurucz and B. Bell. Atomic line data. http://www.cfa.harvard.edu/amp/ampdata/kurucz23/sekur.html, 1995. Retrieved August 2010.

[KSMFAO07] S. Kajari-Schroder, G. Morigi, S. Franke-Arnold, and G.-L. Oppo. Phase-dependent light propagation in atomic vapors. Physical Review A, 75:013816, 2007.

[KTPG85] B. Kleinmann, F. Trehin, M. Pinard, and G. Grynberg. Degenerate four-wave mixing in sodium vapor in the rabi regime. Journal of the Optical Society of America B, 2:704–713, 1985.

[LX96] Y. Li and M. Xiao. Enhancement of nondegenerate four-wave mixing based on electromagnetically induced transparency in rubidium atoms. Optics Letters, 21:1064–1066, 1996.

[Man87] G. Manneberg. Phase-matched frequency tripling and phase conjugation in isotropic materials. Journal of the Optical Society of America B, 4:1790–1793, 1987.

[MBAL07] C.F. McCormick, V. Boyer, E. Arimondo, and P.D. Lett. Strong relative intensity squeezing by four-wave mixing in rubidium vapor. Optics Letters, 32:178–180, 2007.

[MFAO02] G. Morigi, S. Franke-Arnold, and G.-L. Oppo. Phase-dependent interaction in a four-level atomic configuration. Physical Review A, 66:053409, 2002.

[MGB85] M.S. Malcuit, D.J. Gauthier, and R.W. Boyd. Suppression of amplied spontaneous emission by the four-wave mixing process. Physical Review Letters, 55, 1985.

[MKS87] M.W. Maeda, P. Kumar, and J.H. Shapiro. Observation of squeezed noise produced by forward four-wave mixing in sodium vapor. Optics Letters, 12:161–163, 1987.

[MSS84] K. Miyazaki, H. Sakai, and T. Sato. Generation of continuously tunable coherent vacuum-ultraviolet radiation in Cd vapor. Optics Letters, 9:457–459, 1984.

[MWS+06] T. Meijer, J.D. White, B. Smeets, M. Jeppesen, and R.E. Scholten. Blue five-level frequency-upconversion system in rubidium. Optics Letters, 31(3):1002–1004, 2006.

[Nes63] A.N. Neseyanov. Vapor Pressure of the Chemical Elements. Elsevier, Amsterdam, 1963. English edition edited by Robert Gray.

[RCH09] P.K. Vudyasetu R.M. Camacho and J.C. Howell. Four-wave-mixing stopped light in hot atomic rubidium vapour. Nature Photonics, 3:103–106, 2009.

[RKRT08] Yu. Ralchenko, A.E. Kramida, J. Reade, and NIST ASD Team. Nist atomic spectra database (version 3.1.5). http://physics.nist.gov/asd3, 2008. Retrieved August 2010.

[RW85] M.D. Reid and F.D. Walls. Generation of squeezed states via degenerate four-wave mixing. Physical Review A, 31:1622–1635, 1985.

[SAGH08] P. Siddons, C.S. Adams, C. Ge, and I.G. Hughes. Absolute absorption on rubidium D lines: comparison between theory and experiment. Journal of Physics B, 41:155004, 2008.

[VFARA10] A. Vernier, S. Franke-Arnold, E. Riis, and A.S. Arnold. Enhanced frequency up-conversion in Rb vapor. Optics Express, 18:17020–17026, 2010.

[VNMT98] S.S. Vianna, P. Nussenzveig, W.C. Magno, and J.W.R. Tabosa. Polarization dependence and interference in four-wave mixing with rydberg levels in rubidium vapor. Physical Review A, 58:3000–3003, 1998.

[Yue85] H.P. Yuen. Two-photon coherent states of the radiation field. Physical Review A, 13:2226–2243, 1985.

[ZLHS02] A.S. Zibrov, M.D. Lukin, L. Hollberg, and M.O. Scully. Efficient frequency up-conversion in resonant coherent media. Physical Review A, 65:051801(R), 2002.

CHAPTER 5

Blue Light generation - Model

The development of a model for the blue light experiment started as a side-project to investigate the likely phase dependence of the conversion efficiency, but as both experiment and theory exhibited complex behaviours, it turned out difficult to match the model to the experiment. This side-project turned into an important part of this thesis as a large amount of time, work and discussions were required to understand the physics of the process. Bridging the gap between the experimental and theoretical points of view was a productive and enjoyable experience which eventually lead to a better grasp of the effects at play.

The numerical model consisted in a solution of the steady states of the optical Bloch equations (OBE). The Mathematica code that was used is an extension of the code developed by Dr. Franke-Arnold for the study of phase-dependent four-wave mixing in the four-level "diamond" configura-

tion, published by G. Morigi et al. [MFAO02]. The details of the mathematical model used in this numerical analysis are presented in the first part of the chapter. This numerical analysis was completed by the dressed states picture when appropriate, to simplify the interpretation.

The analysis presented here was restricted to the steady state of a single five-level atom driven by four constant near-resonant fields, as shown on Figure 5.1. Some propagation effects could be inferred qualitatively by combining theoretical data and experimental evidence. The case of phase-matching was given particular attention and some fairly good agreement was obtained.

5.1 Model

Because of the complexity of a high temperature vapour of Rubidium driven above saturation by two lasers we had to assess which parameters to include or omit in the description. Due to the large computation time of the programme for a relatively small (four or five) number of levels, it was out of the question to include the fourteen hyperfine levels of each isotope (see Appendix A), so only the ground state hyperfine doublet, and the main 5D, 5P and 6D levels were considered.

Omitting the hyperfine structure of the 5P, 5D and 6P levels was necessary as the number of coupled equations goes with the square of the number of levels. As we shall see, this simplification is suitable for modeling the

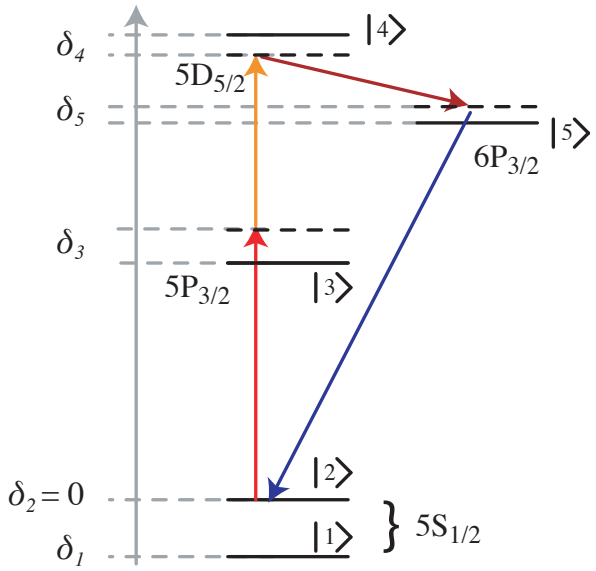

Figure 5.1: Pumping scheme with detunings. Omitting the hyperfine magnetic sub-levels is equivalent to assuming that the atoms are pumped with $\{\sigma_+, \sigma_+\}$ due to the subsequent optical pumping into the levels of highest angular momentum.

general trend of the experiment, but it is insufficient to explain all the effects experimentally observed, in particular the polarisation dependence of the blue light generation. This theoretical level scheme adequately describes a system pumped with two σ_+ (or σ_-) transitions. Indeed, as the only possible path of $\{\sigma_+, \sigma_+\}$ is allowed for the downward cascade, it effectively corresponds to a closed system. This transition scheme is also that with the largest oscillator strength, as well as the optimum pumping for the generation of blue light (see Section 4.2.4).

The Hamiltonian directing the coherent dynamics is then given by [MFAO02]:

$$\begin{aligned} H(t) &= \frac{p_z^2}{2m} + \sum_{j=2}^{5} \hbar\delta_j |j\rangle\langle j| + \frac{\hbar}{2}\big\{ g_{13}e^{-i\Phi_{13}}|3\rangle\langle 1| + g_{23}e^{-i\Phi_{23}}|3\rangle\langle 2| \\ &\quad + g_{34}e^{-i\Phi_{34}}|4\rangle\langle 3| + g_{54}e^{-i\Phi_{54}}|4\rangle\langle 5| \\ &\quad + g_{15}e^{-i\Phi_{15}}|5\rangle\langle 1| + g_{25}e^{-i\Phi_{25}}|5\rangle\langle 2| + H.c.\big\}, \end{aligned} \tag{5.1}$$

where :

- g_{ij} denotes the coupling between levels $|i\rangle$ and $|j\rangle$, and is related to the Rabi frequency as $g_{ij} = 2\Omega_{ij} = 2\frac{d_{ij}E_{ij}}{\hbar}$ with d_{ij} the dipole moment of the transition, and E_{ij} the coupling electric field
- δ_{ij} is the detuning of the driving laser light with respect to the natural atomic transition
- $\Phi_{ij} = \phi_{ij} + \varphi_{ij}$ is the sum of the phase of the input field $\phi_{ij} = k_{ij}z - \omega_{ij}t + \theta$ and φ_{ij} the phase of the dipole
- $\frac{p^2}{2m}$ is the kinetic energy of the atom, which we neglect.

The Hamiltonian 5.1 can then be transformed using the unitary operator:

$$\begin{aligned} \hat{U} &= \exp\left(i\left(\Phi_{13} + \Phi_{34} - \Phi_{54}\right)\right)|1\rangle\langle 1| + \exp\left(i\left(\Phi_{23} + \Phi_{34} - \phi_{54}\right)\right)|2\rangle\langle 2| \\ &\quad + \exp\left(i\left(\Phi_{34} - \Phi_{54}\right)\right)|3\rangle\langle 3| + \exp\left(i\Phi_{54}\right)|4\rangle\langle 4| + |5\rangle\langle 5|, \end{aligned} \tag{5.2}$$

following the transformation rule $\tilde{H}(t) = -i\hbar\hat{U}^{-1}\dot{\hat{U}} + \hat{U}^{-1}\hat{H}(t)\hat{U}$. This transformation formally simplifies Equation 5.1 by attributing the overall phase to the $5S_{1/2}$-$6P_{3/2}$ transition, connecting levels $|1\rangle$ and $|5\rangle$, as well as $|2\rangle$ and $|5\rangle$.

$$\begin{aligned}\tilde{H}(t) &= \frac{p_z^2}{2m} + \sum_{j=2}^{5} \hbar\delta_j |j\rangle\langle j| + \frac{\hbar}{2}\big\{ g_{13}|3\rangle\langle 1| + g_{23}|3\rangle\langle 2| \\ &\quad + g_{34}|4\rangle\langle 3| + g_{54}|4\rangle\langle 5| \\ &\quad + g_{15}e^{-i(\Phi_{15}+\Phi_{54}-\Phi_{13}-\Phi_{34})}|5\rangle\langle 1| \\ &\quad + g_{25}e^{-i(\Phi_{25}+\Phi_{54}-\Phi_{13}-\Phi_{34})}|5\rangle\langle 2| + H.c.\big\}\end{aligned} \tag{5.3}$$

The energy zero in Equation 5.3 is set to the ground upper hyperfine state $|2\rangle$ so that the detunings correspond to the experimental data. The detunings δ_i are expressed as a function of the field and natural resonance frequencies as :

$$\delta_1 = -\omega_{12}^0 + (\omega_{13} - \omega_{23}) \tag{5.4}$$

$$\delta_2 = 0 \tag{5.5}$$

$$\delta_3 = -\omega_{13}^0 + \omega_{13} \tag{5.6}$$

$$\delta_4 = -\omega_{14}^0 + (\omega_{13} + \omega_{34}) \tag{5.7}$$

$$\delta_5 = -\omega_{15}^0 + (\omega_{13} + \omega_{34} - \omega_{45}) \tag{5.8}$$

The relaxation processes are described by the Lindblad operator $\mathcal{L}$ [GZ91]:

$$\mathcal{L}\rho = \sum_{j=3,5} \frac{\gamma_{j1}}{2} \left(2|1\rangle\langle j|\rho|j\rangle\langle 1| - |j\rangle\langle j|\rho - \rho|j\rangle\langle j|\right) \tag{5.9}$$

$$+ \sum_{j=3,5} \frac{\gamma_{j2}}{2} \left(2|2\rangle\langle j|\rho|j\rangle\langle 2| - |j\rangle\langle j|\rho - \rho|j\rangle\langle j|\right) \tag{5.10}$$

$$+ \sum_{j=3,5} \frac{\gamma_{4j}}{2} \left(2|j\rangle\langle 4|\rho|4\rangle\langle j| - |4\rangle\langle 4|\rho - \rho|4\rangle\langle 4|\right) \tag{5.11}$$

The time dependence of the system is determined by:

$$\frac{\partial \rho}{\partial t} = \frac{1}{i\hbar}\left[\tilde{H}\left(\Phi_1, \Phi_2\right), \rho\right] + \mathcal{L}\rho \tag{5.12}$$

The density matrix ρ gives the full atomic state, that is, the population of the natural states, the refractive index and the absorption/gain. Each of these observable quantities corresponds to an element of the density matrix. A rough guide to the interpretation of the matrix elements in terms of experimental observables can be found in the next section.

5.2 Physical interpretation of the density matrix elements

The study presented in Section 5.4 involves the comparison between the experimental data and the value of the density matrix elements. In practice, this means retrieving the populations, the refractive index and the absorption of the fields in the atomic medium from the computed density

matrix. This section presents the interpretation we used throughout the analysis. For the sake of simplicity we shall start with the density matrix of a two-level atom, with ground state $|1\rangle$ and excited state $|2\rangle$:

$$\rho = \begin{pmatrix} \rho_{11} & \rho_{12} \\ \rho_{21} & \rho_{22} \end{pmatrix} \tag{5.13}$$

The probability for the atom to be in state j is given by ρ_{jj}, which is always a real number. The fluorescence from an ensemble of atoms is proportional to the number of atoms in the excited state. In the case of a two-level atom of excited state decay rate γ, the rate of spontaneous emission from a volume V of a vapour of density N is given by $N.V\rho_{22}\gamma$. In our simplified 5-level Rubidium atom, the experimentally measured fluorescence on the 420 nm transition will be compared with ρ_{55} (see Figure 5.1).

The non-diagonal elements ρ_{ij} represent the coupling between the two levels, or coherences. The real part of coherences quantifies the dephasing of an incident wave by the atomic system thus expresses the refractive behaviour of the atom. Its imaginary part gives the absorption profile.

It is the imaginary part of ρ_{ij} that is responsible for the absorption of an input field. In a two-level atom, the imaginary part of the coherence $\Im(\rho_{12})$ is always positive, corresponding to the absorption of the excitation field. In multiple level systems, notably in the presence of population inversion, $\Im(\rho_{ij})$ can be negative, thus leading to the amplification of the excitation wave. The density matrix elements which account for the generation of the

blue beam are therefore $\Im(\rho_{15})$ and $\Im(\rho_{25})$. In Section 5.4 $-\Im(\rho_{15})$ and $-\Im(\rho_{25})$ will be plotted in order to show gain instead of absorption.

For a two-level atom, the real part of the linear susceptibility $\chi_{12}^{'} = n_{12} - 1$ is commonly expressed as [ISJ74]:

$$\chi_{12}^{'} = \frac{d_{12}^2 N}{\epsilon_\circ E} \frac{\delta}{\delta^2 + \gamma^2} (\rho_{22} - \rho_{11}) \tag{5.14}$$

where N is the number of atoms per unit volume, d_{12} is the dipole moment of the transition, E is the amplitude of the excitation wave, δ is the detuning and γ is the spontaneous decay rate.

In our case, the 780 nm and 420 nm beams are near-resonant with both ground states. Taking the 420 nm transition as an example, the susceptibility is then given by [FKS+92]:

$$\chi_{12}^{'} = \frac{P}{\epsilon_\circ E} = \left[\frac{d_{15} N}{\epsilon_\circ E} \Re(\rho_{15}) + \frac{d_{25} N}{\epsilon_\circ E} \Re(\rho_{25}) \right] \tag{5.15}$$

In the subsection presenting phase-matching, the linear susceptibility $\chi_{ij}^{'}$ will be either expressed as $\chi_{ij}^{'} = \frac{dN}{\epsilon_\circ E} \Re(\rho_{ij})$ or as Equation 5.15, as appropriate.

5.3 Computational evaluation

In order to be solved in Mathematica as a matrix diagonalisation, Equation 5.12 had to be transformed to $\frac{\partial \rho}{\partial t} = L\rho$ where $L = H + L_{decay}$. The steady states of the ρ_{ij} were computed by solving this equation numerically (replacing any of the 25 coupled equations by the conservation of trace

$\sum_{j=1}^{5} \rho_{jj} = 1$, as the system is overdetermined). Although the propagation of the field is central to the generation of coherent blue light, the steady state of the system can nevertheless give a reliable picture of the processes undergone by the atomic gas provided thermal and propagation effects are included in the subsequent interpretation.

The experimental maximum pumping values, the branching ratios to the ground state hyperfine levels (Clebsch-Gordan coefficients), and the decays of the excited states of ^{85}Rb and ^{87}Rb are given in Table 5.1. There is neither experimental control over it nor measurement of the value of δ_5 as it is determined by the probability of the downward cascade itself. In the following section we will show that for low intensities of infrared and blue light $\delta_5 = 0$ is a reasonable approximation in the limit of weak infrared and blue fields as the most likely decay route is resonant.

It is worth mentioning here that because of the absorption of the vapour, the effective experimental Rabi frequencies within the central interaction region are estimated to be lower and frequency dependent.

An incoherent transfer of population from $|1\rangle$ to $|2\rangle$ and $|2\rangle$ to $|1\rangle$ estimated to 6 MHz, corresponding to the interaction time of atoms at 120°C (whose velocity is therefore 340 m/s) in a beam focus of 60 μm, was added "manually" to account for the finite interaction time between the atoms and the light.

The Hamiltonian 5.1 is phase dependent, and it was shown [KSMFAO07] that a zero phase difference between the two excitation paths

Table 5.1: Experimental values for ^{85}Rb and ^{87}Rb - Natural ratio of isotopes : .39

Transition	Γ (MHz)	Ω_{Rabi} (GHz)	C_{ij}coeff.	Level	Detuning (MHz)
$\|3\rangle\langle 1\|$	5.9	1.38	.84	$\|1\rangle$	$\delta_1 = -2.195$
$\|3\rangle\langle 2\|$	5.9	1.38	1	$\|2\rangle$	$\delta_2 = 0$
$\|4\rangle\langle 3\|$	0.4	0.36	1	$\|3\rangle$	$\delta_3 = -\delta_{780}$
$\|4\rangle\langle 5\|$	0.2	0.3	1	$\|4\rangle$	$\delta_4 = -\delta_{780} - \delta_{776}$
$\|5\rangle\langle 1\|$	0.6	0.04	.84	$\|5\rangle$	$\delta_5 = -\delta_{780} - \delta_{776} + \delta_{IR}$
$\|5\rangle\langle 2\|$	0.6	0.04	1		
Transition	Γ (MHz)	Ω_{Rabi} (GHz)	C_{ij} coeff.	Level	Detuning (MHz)
$\|3\rangle\langle 1\|$	5.9	1.38	.65	$\|1\rangle$	$\delta_1 = -5.44$
$\|3\rangle\langle 2\|$	5.9	1.38	.84	$\|2\rangle$	$\delta_2 = 1.1$
$\|4\rangle\langle 3\|$	0.4	0.36	1	$\|3\rangle$	$\delta_3 = -\delta_{780}$
$\|4\rangle\langle 5\|$	0.2	0.3	1	$\|4\rangle$	$\delta_4 = -\delta_{780} - \delta_{776}$
$\|5\rangle\langle 1\|$	0.6	0.04	.65	$\|5\rangle$	$\delta_5 = -\delta_{780} - \delta_{776} + \delta_{IR}$
$\|5\rangle\langle 2\|$	0.6	0.04	.84		

$5S_{1/2} \rightarrow 5P_{3/2} \rightarrow 5D_{5/2}$ and $5S_{1/2} \rightarrow 6P_{3/2} \rightarrow 5D_{5/2}$, as depicted in Figure 5.1 is the stable solution established on propagation. As we are interested here in the steady state of the atoms we kept the overall phase of the two loops equal to zero. This approach always assumes that the sums of the phases of the dipoles $\Delta\varphi_1 = \varphi_{13} + \varphi_{34} - \varphi_{54} - \varphi_{15}$ and $\Delta\varphi_2 = \varphi_{23} + \varphi_{34} - \varphi_{54} - \varphi_{25}$ is zero. It was shown in the general case that $\Delta\varphi \neq 0$ leads to a cancellation of the coherent terms upon propagation [KSMFAO07], which in our system would decrease the blue light generation.

The assumption of $\Delta\varphi_{1,2} = 0$ is certainly valid for the $\{\sigma_+, \sigma_+\}$ as the Clebsch-Gordan coefficients only depend on L, S, J, F and m_F and are thus the same on the way up through $5P_{3/2}$ and on the way down through $6P_{3/2}$. For more details, see Section 5.5.

5.3.1 Doppler broadening

Considering the high temperature of the cell, it is clear that the effect of Doppler broadening is worth investigating. Propagating the field in an atomic medium with a spread of velocities, possibly using a Monte-Carlo simulation, would be the rigorous way of integrating it into the model. Field propagation was beyond the scope of this study so Doppler broadening was simulated by smoothing the steady state of the populations and coherences with a Gaussian of Doppler width $\Delta\omega_D = \frac{1}{\lambda}\sqrt{\frac{k_B T}{m}} \approx 200\,\text{MHz}$ corresponding to the temperature of the cell, i.e. 120°C. The density matrix elements were smoothed over a frequency range of about 3 times the Doppler width of the atomic vapour.

Doppler-broadening for two-photon absorption can be easily understood by considering the simplest case of two-photon resonance shown in Figure 5.2, but can of course be extended to any set of $\{\delta_{780}, \delta_{776}\}$. Because of the Doppler effect, two-photon resonance can be achieved for a range of δ_{780} and δ_{776}. Indeed, two-photon resonance with respect to an atom at rest is equivalent to blue detuned pumps counter-propagating with respect to the interacting atom, provided the sum of the pump detunings $\delta_{780} + \delta_{776}$ is equal to the Doppler shift $\nu_{Dopp} = -v\left(\frac{1}{\lambda_{780}} + \frac{1}{\lambda_{776}}\right)$.

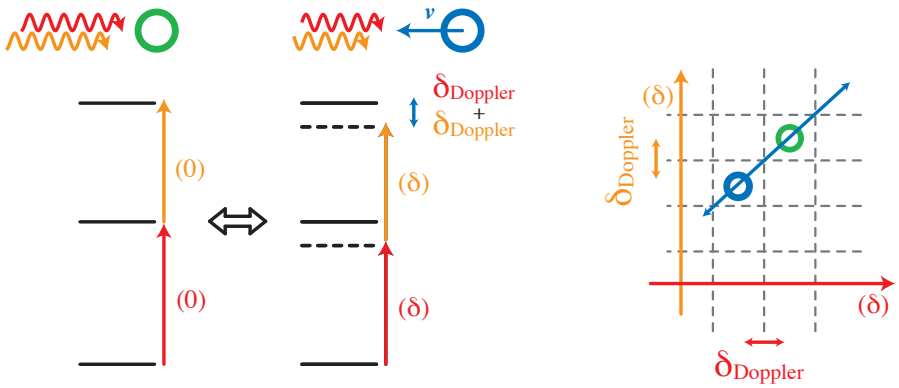

Figure 5.2: Doppler averaging: the pumping scheme on the left hand side of the figure represents two-photon resonance with an atom at rest. This is equivalent to two red-detuned beams, counterpropagating with respect to the interacting atom. The numerical grid is represented schematically on the right hand side, and shows that Doppler averaging has to be performed along the diagonal line shown in blue.

5.4 Discussion and comparison with experimental data

As we are aiming at singling out the contributions of the effects and behaviours taking place in the vapour, we will mainly look at the steady states of a non-Doppler broadened system and attempt to interpret the results in the light of the dressed states. We will investigate the behaviour of the emission spectrum of both incoherent and coherent light, as well as that of phase matching as a function of pump frequencies.

5.4.1 Two-photon absorption and blue fluorescence

Before considering coherences on the 5S-6P-5D ladder, it is instructive to simply study the emission of blue fluorescence, which is proportional to the population on $|5\rangle$ in the absence of any infrared and 420 nm coherent fields. Given that the dipole moment of the 5D-6P transition is 13 times larger than that of the 5D-5P transition, the occupancy of state 5D leads to a large amount of 5 μm and 420 nm fluorescence. Experimentally, a large amount of blue fluorescence was thus observed along the two-photon absorption lines. The shape of the lines of two-photon absorption for low 776 nm intensity can be predicted by calculating the new resonance frequencies of the three lowest levels shown in Figure 5.1 "dressed" by the electromagnetic field. The latter induces a level coupling of energy $\hbar\Omega$ with $\Omega = dE/\hbar$ which shifts the bare levels (see p. 163 of Ref. [Ste05]). The new resonance frequencies of the dressed atom are then found by calculating the difference between the eigenvalues of the Hamiltonian:

$$\frac{H_0}{\hbar} = \begin{pmatrix} \delta_1 & 0 & C_{13}\frac{\Omega}{2} \\ 0 & \delta_2 & C_{23}\frac{\Omega}{2} \\ C_{13}\frac{\Omega}{2} & C_{23}\frac{\Omega}{2} & \delta_3 \end{pmatrix} \tag{5.16}$$

It should be underlined that this description does not take incoherent processes (spontaneous decay, collisions, losses) into account and can only give information about level mixing.

For a very low intensity on the 6P-5D transition, two-photon absorption

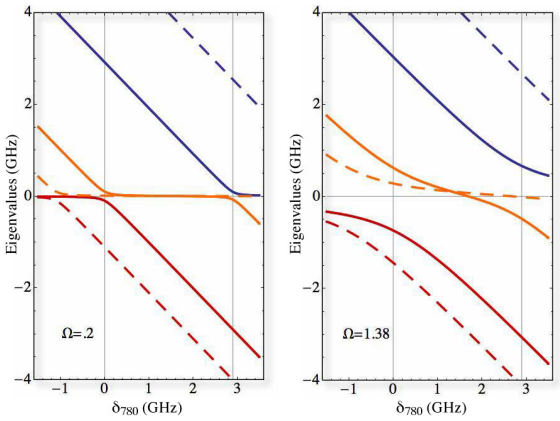

Figure 5.3: Eigenvalues of the dressed states (linear combinations ofs $|1\rangle$, $|2\rangle$ and $|3\rangle$). Solid line for ^{85}Rb, dashed for ^{87}Rb. Ω is the Rabi frequency in GHz.

follows the eigenvalues, as shown by the numerical evaluation of $\Im(\rho_{34})$ plotted as a function of δ_{780} and δ_{776} in Figure 5.4.

The two-photon absorption leading to the generation of blue light does not strictly coincide with a simple probing of the dressed three lower levels: when the light intensity on the 776 nm transition is large compared to the saturation intensity, all four addressed levels are mixed, and the 776 light cannot be considered as a weak probe. The discrepancy between the two cases can be assessed by calculating the two-photon absorption by numerical solution of the optical Bloch equations (Sec. 5.3). The two graphs on Figure 5.5 give the absorption of light on $|3\rangle \rightarrow |4\rangle$, i.e. $\Im(\rho_{34})$ as a function of δ_{780} and δ_{776} for a low power probe on the 776 nm transition, or the full power present in the experiment. Both graphs were plotted for the experimental values of $\Omega_{13} = \Omega_{23} = 1.38$ GHz. The presence of a large amount of 776 nm

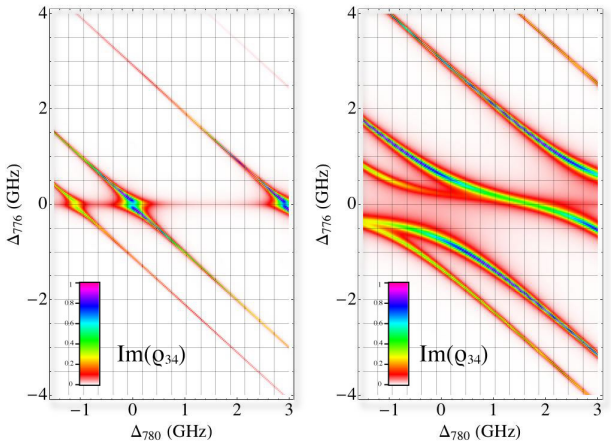

Figure 5.4: $\Im(\rho_{34})$ (scaled to 1). Left: $\Omega_{13} = \Omega_{23} = 0.2\,\text{GHz}$, Right: $\Omega_{13} = \Omega_{23} = 1.38\,\text{GHz}$. For both graphs, $\Omega_{34} = 0.01\,\text{GHz}$ and all other fields are zero.

light induces a shift and a distortion of the lines that becomes larger in the neighbourhood of the avoided crossings.

The uppermost level of the ladder is populated as a result of two-photon absorption, and fluorescence is thus observed (Figure 5.6, a)). In the absence of any infrared or blue coherent light, the system exhibits population inversion between $|4\rangle$ and $|5\rangle$ due to a favourable decay ratio $\Gamma_4/\Gamma_5 = 0.4$ (Table 5.1). The lines of population inversion follow the condition of two-photon resonance where light can thus be amplified, as shown on Figure 5.6, b). It may be speculated that amplified spontaneous emission acts here as a trigger to the four-wave mixing process, and is subsequently taken over by four-wave mixing if the phase-matching conditions are favourable. This could be measured experimentally by monitoring the ratio of forward and

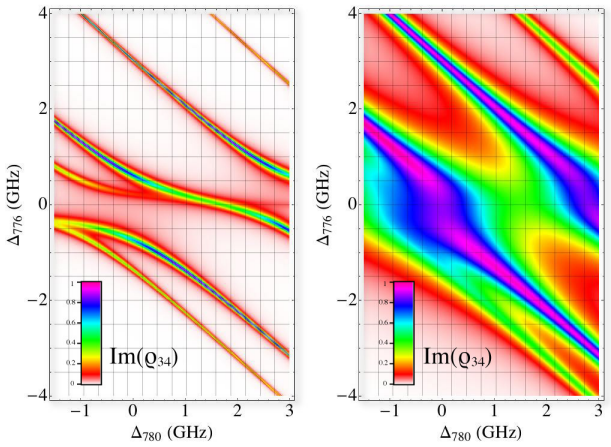

Figure 5.5: $\Im(\rho_{34})$ (scaled to 1). Left: $\Omega_{34} = 0.01\,\text{GHz}$. Right: $\Omega_{34} = 0.39\,\text{GHz}$. For both graphs, $\Omega_{13} = \Omega_{23} = 1.38\,\text{GHz}$ and all other fields are zero.

backward emission of $5\,\mu$m [MGB85].

Graph c) on Figure 5.6, shows that adding a small seed of infrared and 420 nm populates state $|5\rangle$, due to stimulated emission on $|4\rangle \rightarrow |5\rangle$. This results in a depletion of the population inversion on $|4\rangle \rightarrow |5\rangle$ (graph d), Figure 5.6). The sharp, straight lines are due to the low power of the seeding terms (about 10 nW) and the fact that δ_{IR} was manually set to $\delta_{IR} = \delta_{780} - \delta_{776}$ instead of being determined by its probability in the cascade. As the four-wave mixing process conserves energy, δ_{420} was always set to zero.

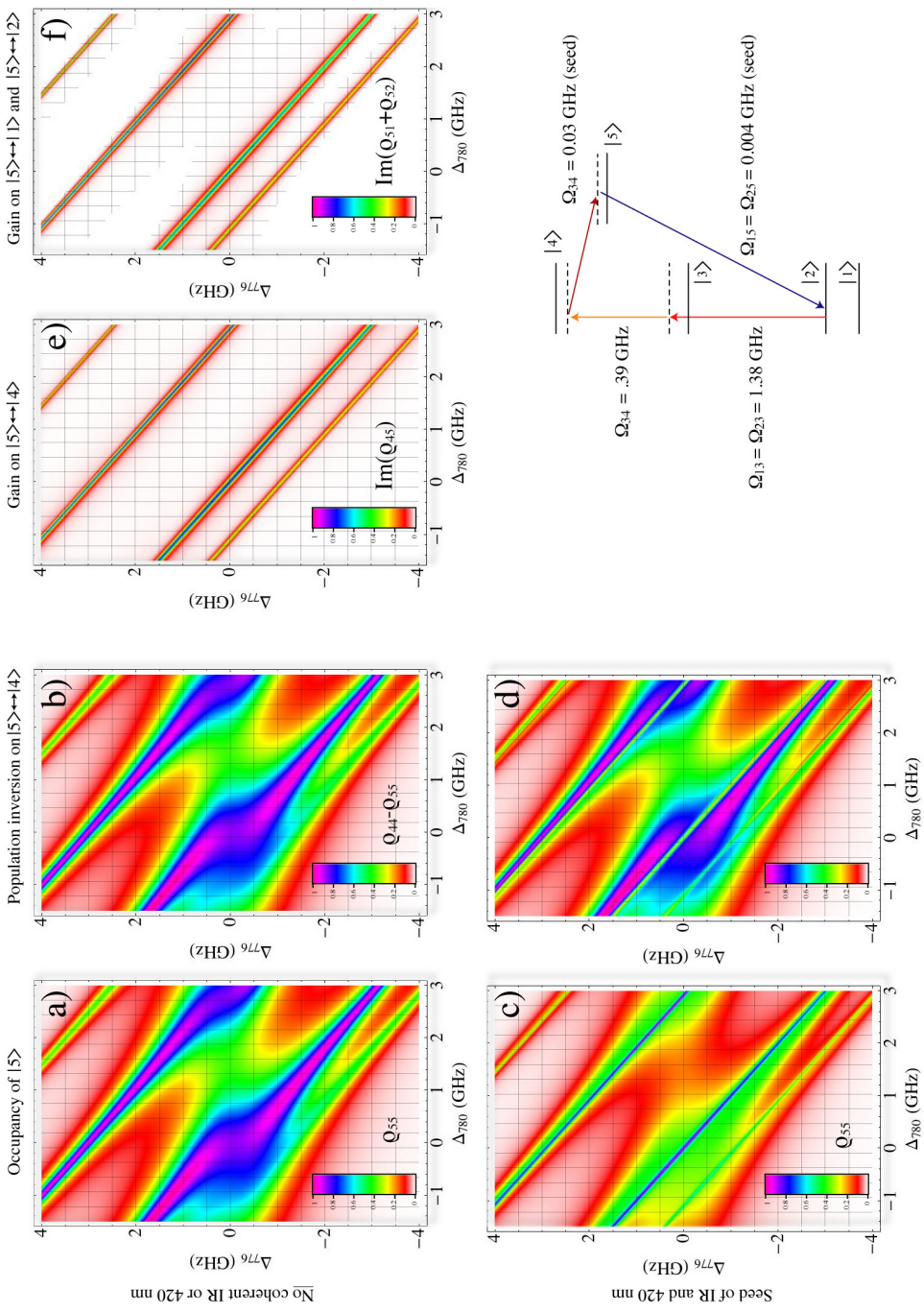

Figure 5.6: a) and c): blue fluorescence (ρ_{55}). b) and d): population inversion $\rho_{44} - \rho_{55}$; e) 5 μm gain, f) 420 nm gain. For c), d), e) and f), $\delta_{IR} = -\delta_{780} - \delta_{776}$, and $\delta_{420} = 0$ to satisfy conservation of energy in the process.

5.4.2 Atomic coherences on the infrared and blue transitions

As this section presents comparisons with the experimental data, the notation $\{\Omega_{780}, \Omega_{776}, \Omega_{IR}, \Omega_{420}\}$ *will be used instead of* $\{\Omega_{13}, \Omega_{23}, \Omega_{34}, \Omega_{45}, \Omega_{15}, \Omega_{25}\}$.

While the semiclassical approach we took here does not allow us to study the mechanism of the emission of the first coherent photons (which would require quantization of the light field), it is suitable for the analysis of the propagation or the steady state of an already present coherent field. The growth rate of a driving coherent field in the atomic medium is proportional to the imaginary part of atomic coherence, so evaluating the atomic coherences on the $5\,\mu$m and 420 nm transitions including a seeding term corresponding to small, but classical fields shows whether an initial spark of coherent light gets amplified or absorbed.

The first and simplest approach that can be taken is to evaluate whether a seed of coherent 420 light at a given frequency gets amplified. This is quantified by $-\Im(\rho_{15} + \rho_{25})$, which is negative for absorption and positive for gain. A plot of the gain on the $5\,\mu$m and 420 nm transitions is shown on Figure 5.6, graphs e) and f). All values on this graph are positive, which confirms that the seeding fields are amplified along the two-photon resonance. Note that the straightness of the lines is due to the condition

imposed on δ_{IR} and is not physically meaningful.

Given that the Rabi frequencies of all fields vary along the cell and that δ_{IR} is unknown, trying to reproduce the experimental results quantitatively from the steady state of a single atom driven by constant field is unrealistic. It is however useful to examine the steady states of the atom for various driving regimes and attempt to infer the physical processes underlying the generation of blue light.

As δ_{IR} is unknown, it is interesting to map the resonances as a function of δ_{776} and δ_{IR} keeping δ_{780} constant at its experimental optimum $\delta_{780} = 1.6\,\text{GHz}$. The effect of the strength of the different driving fields on the frequency dependence of the resonances is singled out by increasing the Rabi frequency of each driving field. For all fields below saturation (Figure 5.7) a resonance is found for the expected condition of two-photon resonance: $\{\delta_{IR} = 0, \delta_{776} = -1.6\}$. Increasing Ω_{780} shifts the resonances (Figure 5.7) and increasing Ω_{776} splits them, leading to the appearance of the familiar avoided crossings (Figure 5.8).

Figure 4.5 from Chapter 4 showed that the generation of blue light followed the two-photon absorption lines measured at the entrance of the cell, in a region of low $\{\Omega_{780}, \Omega_{780}\}$. The coincidence of these two lines may seem rather surprising, considering that the resonances are shifted by about 100 MHz from the entrance of the cell to the focus.

The interpretation of the coincidence of the two lines is rather speculative in the absence of a model for propagation, but a possible explanation

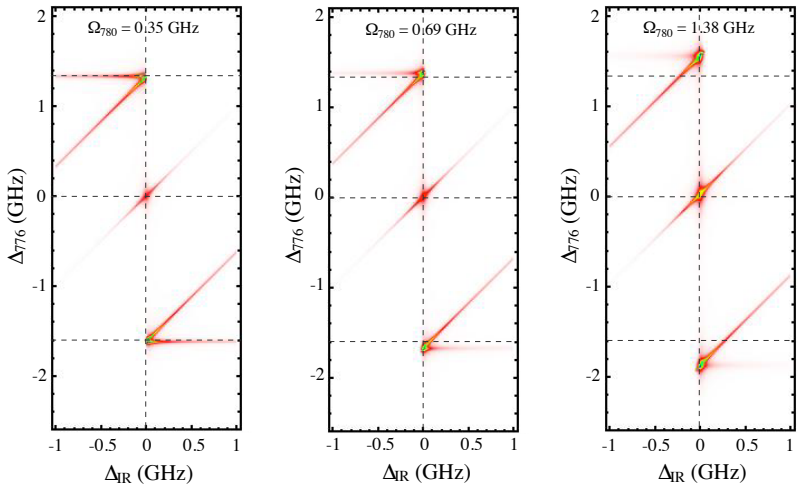

Figure 5.7: Atomic coherences on the infrared transition vs. δ_{IR} and δ_{776}, and with δ_{780}=1.6 GHz. The 776 nm 420 nm and 5 μm fields were input as weak fields with $\Omega_{776} = 0.11\,\text{GHz}, \Omega_{IR} = 0.03\,\text{GHz}, \Omega_{420} = 0.004\,\text{GHz}$.

may be envisaged. As the gain on the 420 nm transition for a given couple of pump beam frequencies depends on the intensity of all beams, the maximum yield after propagation might not be obtained for the pump powers at the focus, but for lower powers, closer to those found at the entrance of the vapour cell. This possibility is not excluded by the model, which shows non-zero, though not maximum, gain for $\{\delta_{IR} = 0, \delta_{776} = -1.6\,\text{GHz}\}$ for the driving Rabi frequencies present at the focal point. The gain on the infrared transition as a function of δ_{776} and δ_{IR} is illustrated in Figure 5.8, for three couples of $\{\Omega_{780}, \Omega_{776}\}$, and keeping the 420 nm and 5 μm fields as weak probes.

Ideally, this hypothesis could be tested experimentally by measuring the

two-photon absorption in a separate cell pumped with weak fields only, and vary the position of the focus within the cell. If the frequency of the infrared field were indeed determined by the fields emitted close to the entrance of the cell in the current setup, then moving the focus should induce a shift of the blue light emission line. In the case of this experimental setup, this would also mean that the infrared and the blue beams are very close to resonance. The absolute frequency of the 420 nm beam could be measured by beating it with the signal from the second harmonic generation from a BBO crystal pumped with a Ti:Sapphire at 840 nm.

It also has to be borne in mind that the Rabi frequencies given in Table 5.1 were calculated from the measured input 780 nm and 776 nm powers and the size of the focus. These values do not account for pump absorption or the fact that the interaction region extends beyond the focal spot. The effective Stark shift is therefore lower than that shown on the right hand side of Figure 5.7, resulting in a higher gain for $\delta_{IR} \approx 0$.

The picture can be completed by evaluating the same coherences with increasing Ω_{IR} and Ω_{420}. A broadening of the emission lines and a shift of the maxima are observed as Ω_{IR} and Ω_{420} are increased. The complexity of the intensity dependence of the gain on the 420 nm transition, illustrated in Figures 5.7, 5.8, and 5.9, means that a quantitative analysis would require field propagation. However, as we shall see in the next section, the steady states calculation does give a good qualitative agreement with the experiment. It also allows a fine resolution in frequency space, which field

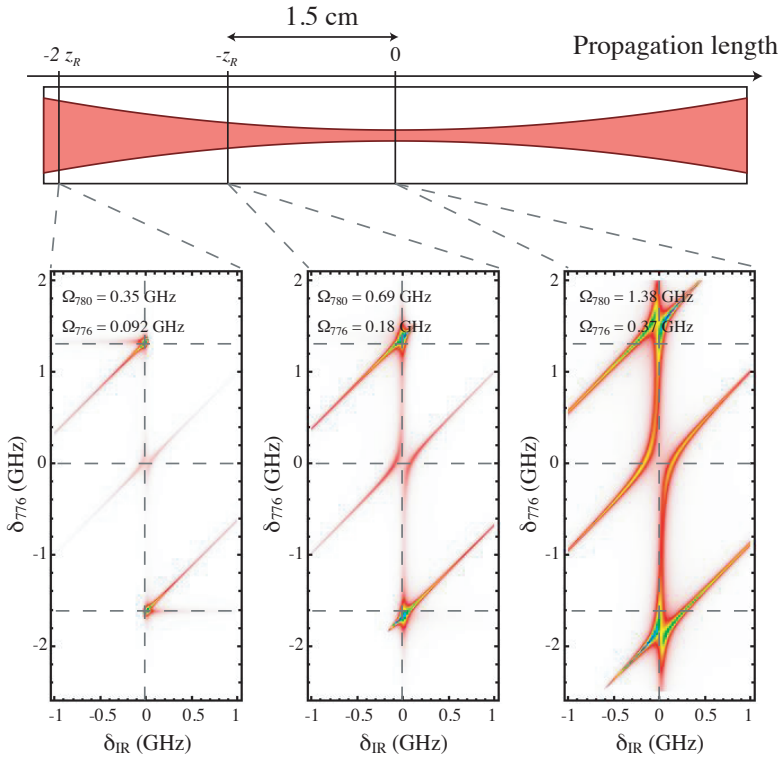

Figure 5.8: Atomic coherences on the infrared transition vs. δ_{IR} and δ_{776}, and with δ_{780}=1.6 GHz. The 420 nm and 5 μm fields were input as weak fields ($\Omega_{IR} = 0.03\,\text{GHz}, \Omega_{420} = 0.004\,\text{GHz}$).

propagation would not due to the long computational time.

5.4.3 Phase Matching

As the four-wave mixing process leading to the generation of blue light takes place in a closed system, the momentum imparted by the excitation wave is fully transferred to the emitted field. This conservation of momentum corresponds to a condition of phase matching. Most familiar in the context

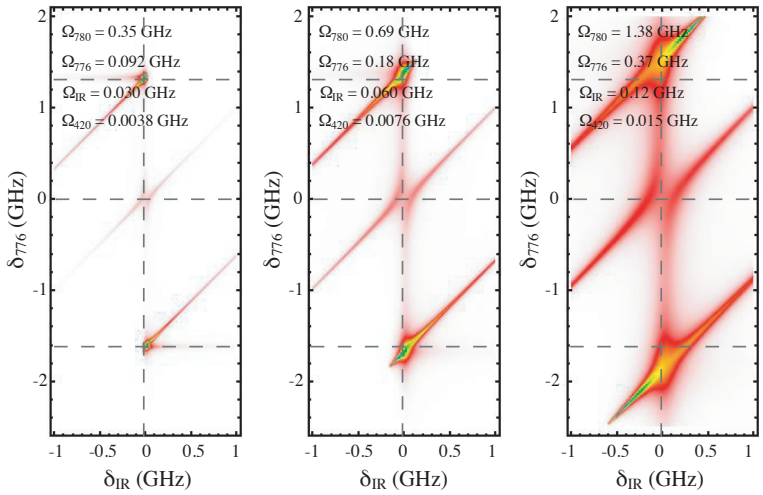

Figure 5.9: Atomic coherences on the infrared transition vs. δ_{IR} and δ_{776}, and with δ_{780}=1.6 GHz.

of second harmonic generation (see for example Ref. [Boy03]), a phase-matching condition must also be satisfied in our system.

The relevant parameter is the phase mismatch $\Delta k = n_{780}k_{780}+n_{776}k_{776}-n_{IR}k_{IR}-n_{420}k_{420}$, with the refractive indices defined as in Equation 5.15, on page 95. The four-wave mixing efficiency as a function of phase mismatch in degenerate four-wave mixing has been studied as early as 1978 [AL78], but the non-degenerate case is more difficult to tackle. There is not, to my knowledge, any theoretical model published on the matter at the date of submission of this thesis. It is however clear that a $\mathrm{sinc}^2(L\Delta k)$ term would appear as it stems directly from the product of the four fields, decomposed into Fourier modes [HM84]. In this section we will then use $\mathrm{sinc}^2(L\Delta k)$ as a qualitative indication for the efficiency dependence on phase mismatch,

and as we shall see it provides a fairly good fit of the the experimental data.

In this system, the amplitude of the emitted 420 nm field is proportional to $-\Im(\rho_{15} + \rho_{25})$, so as a first qualitative approach, it is interesting to compare the experimental data with the computed values of $-\Im(\rho_{15} + \rho_{25})\text{sinc}^2(L\Delta k)$ as a function of δ_{780} and δ_{776}, with $\delta_{IR} = 0$. As underlined in the previous section, $\delta_{IR} = 0$ is only meaningful in this model for low field intensities, so the graphs shown on Figure 5.10 were plotted for the Rabi frequencies given in Table 5.2.

The Rubidium pressure yielding the experimental graph shown on Figure 5.10 a) corresponds to a density of 3×10^{17} atoms per cubic metre. The best theoretical fit for this density was obtained for values of L ranging from 500 μm to 1.5 mm. The theoretical graphs shown on the left hand side of Figure 5.10 were plotted for $L = 2$ mm. The plot obtained for the higher pressure on Figure 5.10 c), was modeled using the same propagation length and a density of 3×10^{18} atoms per cubic metre corresponding to the experimental pressure of 9×10^{-4} mbar.

A fairly good agreement between the theoretical plots and the experiment is obtained. The major discrepancy is the inhibition of the 420 nm light generation for two-photon resonance with the lower ground state of ^{85}Rb, for $\delta_{776} \geq 0$, and on single-photon resonance, for $\{\delta_{780} = 0, \delta_{776} = 0\}$ and $\{\delta_{780} = 2.9\,\text{GHz}, \delta 776 = 0\}$. We believe the latter may be explained by the reabsorption of the 420 nm light.

Also, in the low pressure case, the model does not always allow genera-

Ω_{780}	Ω_{776}	Ω_{IR}	Ω_{420}
0.35	0.09	0.07	0.01

Table 5.2: Rabi frequencies used in Figure 5.10, all in GHz

tion where the experiment does. The model showed that increasing the intensity of the pumps or of the generated beams modifies the phase-matching condition, as well as the frequency dependence of the gain.

The presence of two isotopes in the vapour is taken into account by taking a weighted sum of $-\Im(\rho_{15}+\rho_{25})\mathrm{sinc}^2\left(L\Delta k\right)$ for each isotope, with the weightings $\alpha_{85}=0.72$ and $\alpha_{87}=0.28$ corresponding to their natural occurrence.

The details of the plot are easier to visualise as a cut for $\delta_{776}=-1.6\,\mathrm{GHz}$ and $\delta_{IR}=0\,\mathrm{GHz}$. Figure 5.11 gives a comparison between Figure 4.8 from the Chapter 4 for $\{\sigma_+,\sigma_+\}$ pumping and the theory. The coherent light was modeled for the values of Table 5.1. The fluorescence is essentially generated in the focal area, so for this plot the relevant Rabi frequencies correspond to the intensity at the focal spot (Table 5.2).

It is interesting to note that the experimental plot exhibits local maxima whose spacings are similar to those of a sinc^2 and do not correspond to any hyperfine features. They are reminiscent of the local maxima exhibited by the theoretical curve but have a different frequency scaling. This question should be investigated within the context of the field propagation.

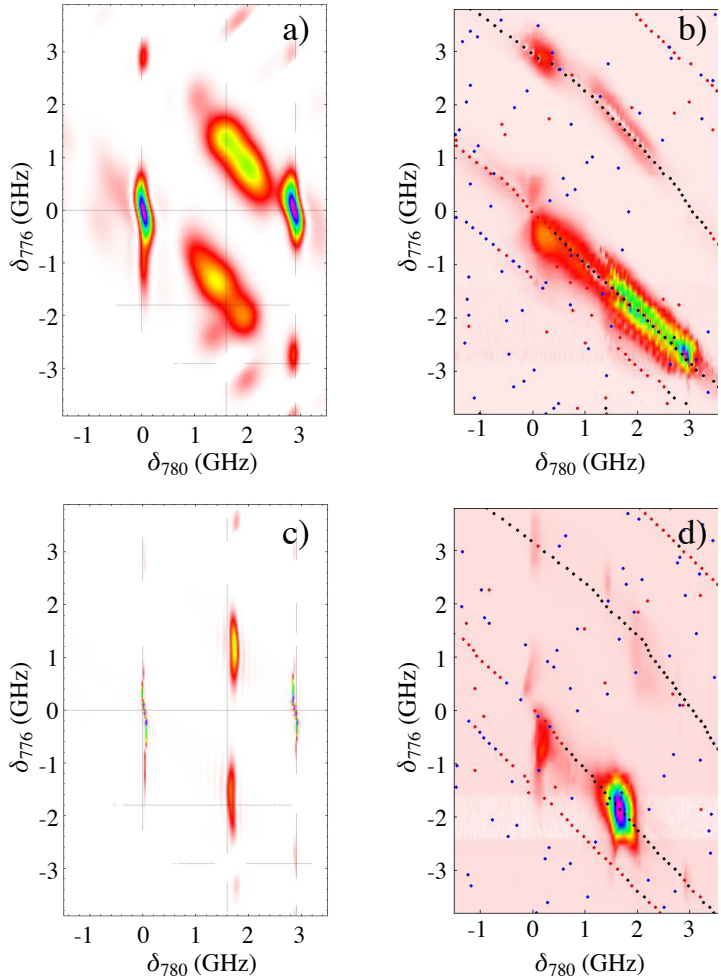

Figure 5.10: a) and c): model $-\Im(\rho_{15}+\rho_{25})\mathrm{sinc}^2\left(L\Delta k\right)$ vs. δ_{780} and δ_{776}, and with δ_{IR}=0. b) and d): experimental data corresponding respectively to low and high Rb pressure. The dotted line on the experimental data corresponds to the two-photon absorption measured as described in Section 4.2.2, page 73.

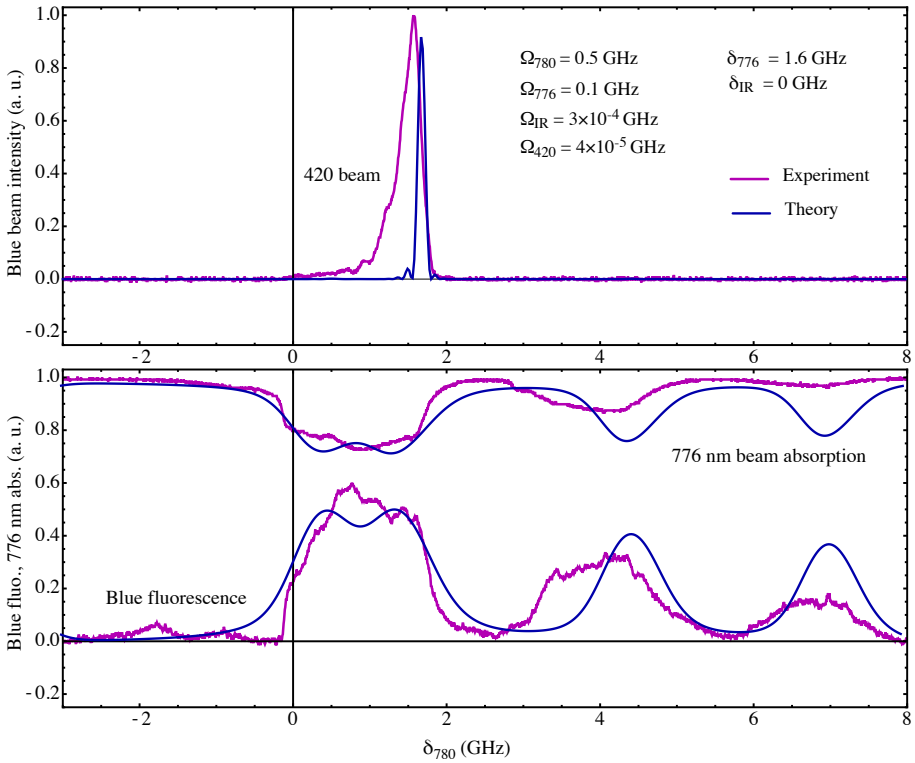

Figure 5.11: Comparison of experiment and theory for blue beam and fluorescence. Top: 420 nm beam intensity (purple), $-\Im(\rho_{15}+\rho_{25})\mathrm{sinc}^2(L\Delta k)$ vs. δ_{780}, with $\delta_{776} = -1.6$ GHz and δ_{IR} =0 (blue). Bottom: 420 nm fluorescence (purple), ρ_{55} (blue). The small peaks on the left hand side of the main blue beam peak might stem from the $\mathrm{sinc}^2(L\Delta k)$ phase-matching term.

5.5 Open questions, further studies

Our analysis so far showed that blue light generation was possible anywhere along the two-photon absorption lines, a behaviour experimentally approached for low Rb density. However the sole evaluation of the coherences is insufficient to explain the very sharp peak that emerges when the

Rb density is increased. Clearly the frequency dependent enhancement or inhibition of the process results from propagation effects induced by the increase in optical path within the vapour.

This question was addressed qualitatively by evaluating the phase mismatch as a function of pump frequencies, for $\delta_{IR} = 0$ and for low driving and emitted fields. The features of the experimental results, notably the existence of a sharp peak, could be reproduced rather accurately. Using a "sinc^2" dependence, without prefactors, is expected to be quantitatively incorrect, but gives good qualitative agreement with the experiment. A rigorous analysis of the phase-matching condition in this highly non-degenerate case would be a particularly interesting topic to pursue.

A more complete picture could be obtained by modelling the effects of propagation. Indeed, the gain on the infrared and 420 nm transitions is both frequency and intensity dependent, which can be addressed by evaluating the field gain from the atomic coherences, replacing the Rabi frequencies accordingly and recalculating the atomic states, for a given propagation length. This approach would allow us to address the issues of the frequency of the infrared and the possible reabsorption of the resonant 420 nm field as the pumps get depleted and no longer ensure gain on the infrared and 420 nm transitions.

Considering the amount of lensing that was experimentally observed on the 780 nm transition (Figure 6.4 of Chapter 6), it could be speculated that lensing might play a role in the frequency selectivity of the blue light gen-

eration due to the reduced 780 nm beam intensity and pump beam overlap. Assessing this theoretically would require the inclusion of the transverse intensity of the beam in the model.

A striking experimentally observed effect was the strong polarisation dependence of the process which our model could not predict, as it did not include the hyperfine structure of levels $5P_{3/2}$, $5D_{5/2}$ and $6P_{3/2}$. It could be speculated that this effect arises from the cancellation of dipole moments on the $5D_{5/2} \rightarrow 6P_{3/2} \rightarrow 5S_{1/2}$ transitions. In order to model this, the full hyperfine structure with all magnetic sub-levels would have to be included, as well as their associated oscillator strength which may be calculated from the formulas found in Ref. [Sob79]. Evaluating the steady state of this system may then give an answer to this interesting question.

5.6 References

[AL78] R.L. Abrams and R. C. Lind. Degenerate four-wave mixing in absorbing media. Optics Letters, 2:94–96, 1978.

[Boy03] R.W. Boyd. Nonlinear Optics. Academic Press. Elsevier Science, second edition, 2003.

[FKS+92] M. Fleischhauer, C.H. Keitel, and M.O. Scully, C. Su, B.T. Ulrich, and S.-Y. Zhu. Resonantly enhanced refractive index

without absorption via atomic coherence. Physical Review A, 46:1468–1487, 1992.

[GZ91] C.W. Gardiner and P. Zoller. Quantum Noise. Springer-Verlag, 1991.

[HM84] C.K. Hong and L. Mandel. Theory of parametric frequency down conversion of light. Physical Review A, 31:2409–2418, 1984.

[ISJ74] M. Sargent III, M.O. Scully, and W.E. Lamb, Jr. Laser Physics. Addison-Wesley, Reading, MA, 1974.

[KSMFAO07] S. Kajari-Schroder, G. Morigi, S. Franke-Arnold, and G.-L. Oppo. Phase-dependent light propagation in atomic vapors. Physical Review A, 75:013816, 2007.

[MFAO02] G. Morigi, S. Franke-Arnold, and G.-L. Oppo. Phase-dependent interaction in a four-level atomic configuration. Physical Review A, 66:053409, 2002.

[MGB85] M.S. Malcuit, D.J. Gauthier, and R.W. Boyd. Suppression of amplied spontaneous emission by the four-wave mixing process. Physical Review Letters, 55, 1985.

[Sob79] I.I. Sobelman. Atomic Spectra and Radiative Transitions. Springer, 1979.

[Ste05] S. Stenholm. Foundations of Laser Spectroscopy. Dover Publications inc., Mineola, New York, 2005.

CHAPTER 6

Laguerre-Gaussian modes in Blue Light

The phase coherence of four-wave mixing makes the blue light experiment a good candidate for the study of phase dependence in light-atom interactions. It is then a practical solution to shape the phase profile to measure how this affects the transverse phase profile of the generated blue beam. This can be done by shaping the beams as Laguerre-Gaussian modes, whose transverse phase possesses a simple azimuthal dependence. As we shall see, Laguerre-Gaussian (LG) modes are an especially interesting case to study, beyond their mere transverse phase structure.

The space and time dependence of the amplitude of Laguerre-Gaussian beams can be mathematically expressed in cylindrical coordinates $\{r, \phi, z\}$ as Equation 6.1, where $L_{p,\ell}\left(\frac{2r^2}{w^2(z)}\right)$ is the associated Laguerre polynomial.

LG modes are uniquely defined by a radial index p and an azimuthal number ℓ and are often written "$\mathrm{LG}_{p,\ell}$" as a shorthand. The azimuthal dependence of the phase is given by $\phi = \ell\theta$, resulting in an undefined phase for $r = 0$. As no field can satisfy this condition, the field intensity at the phase singularity is thus zero. The characteristic doughnut-shaped intensity profile and the phase structure of the three first orders of ℓ are depicted in Figure 6.1.

$$u_{pl}(r,\phi,z) = \sqrt{\frac{P}{w_0^2}}\sqrt{\frac{2p!}{\pi(|\ell|+p)!}}\frac{w_0}{w(z)}\left(\frac{r\sqrt{2}}{w(z)}\right)^{|\ell|} L_{p,\ell}\left(\frac{2r^2}{w^2(z)}\right)\exp\left(-\frac{r^2}{w^2(z)}\right) \times \exp\left(-\frac{ikr^2 z}{2(z^2+z_R^2)}\right) e^{-i\ell\phi}\exp(i(2p+\ell+1)\tan^{-1}\left(\frac{z}{z_R}\right) \tag{6.1}$$

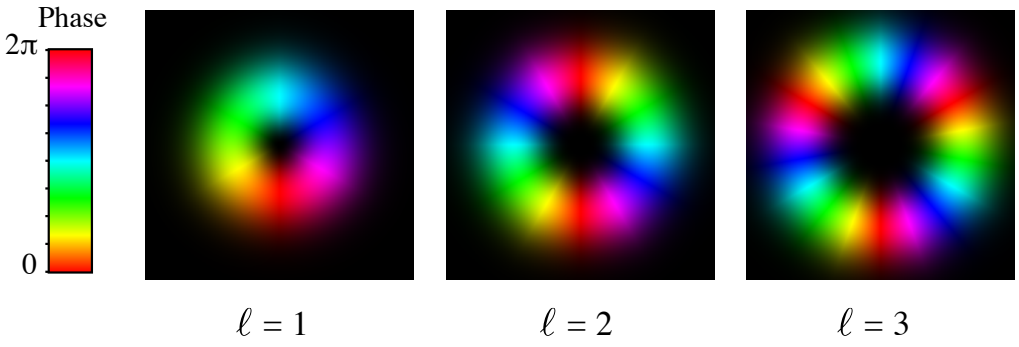

Figure 6.1: Laguerre-Gaussian modes, $p = 0$.

The effects light beams with orbital angular momentum (OAM) exert on matter have been of interest ever since these beams were shown to carry orbital angular momentum [ABSW92]. While it is well known that the

spin angular momentum couples to the magnetic sub-levels of atoms, there is still some question as to whether the OAM of light can be transfered to the internal atomic states. It was however theoretically shown in 1994 by van Enk and Nienhuis that in the paraxial regime ($k_\perp \ll k_z$) the spin and orbital angular momenta of light coupled respectively to the internal and external angular momenta of the atom [vEN94]. There has not been, to my knowledge, any experiment working in the non-paraxial regime. In all experiments devised so far, the beams have been either assumed or shown to be paraxial (see for example [TP99, SB03]). The transfer of $\ell\hbar$ orbital angular momentum per photon and per atom was experimentally demonstrated in 2006 by M. F. Andersen et al. [ARC+06] in a Bose-Einstein condensate. It is also worth mentioning an elegant classical demonstration of the same effect in a simple vapour by S. Barreiro et al. [BTFL06] in the same year. In four-wave mixing experiments such as ours the beam is very clearly paraxial, so if transfer of OAM to the atoms does occur, it is as an imparted mechanical rotation around the beam axis.

The curious topology of LG beams aroused a lot of interest in the field of nonlinear dynamics as the propagation of vortex beams in nonlinear media was shown to exhibit intricate properties. It was observed for example that focusing and defocusing Kerr media could induce a filamentation of the beam due to azimuthal instability [JL92, SF98, VGI+06], and the formation of lattices of optical solitons [MSF92]. For a recent review on the nonlinear dynamics of vortex beams, see [DKT05].

Another point of interest is the conservation of a beam's orbital angular momentum in frequency conversion. The first experiment showing optical pumping of OAM was realised in 1999 in non-degenerate four-wave mixing in Cesium atoms, where OAM was transferred from a pump to a generated beam [TP99]. In the quantum regime, conservation of orbital angular momentum was experimentally investigated in spontaneous parametric down conversion by A. Mair et al. [MVWZ01] in 2001. The physical processes underlying the two-photon entanglement of orbital angular momentum state were studied by S. Franke-Arnold et al. [FABPA02], where the conservation of OAM was demonstrated to stem from phase-matching.

Some phase-matching conditions, though difficult to treat theoretically (see Chapter 5), must be obeyed in the blue light experiment. The phase-coherence at the root of the four-wave mixing process suggested that $\ell_{780} + \ell_{776} = \ell_{IR} + \ell_{420}$, so Dr. Franke-Arnold was interested in investigating what modes would be generated from pumping the system with Laguerre-Gaussian beams. Unlike Ref. [TP99] where one field is generated from three, two correlated coherent fields are generated in the blue light experiment. This degree of freedom makes it more akin to the generation of spatial modes in spontaneous parametric down conversion, which is currently a subject of study [FK08, OMTT08].

The frequency up-conversion of LG beams via four-wave mixing presented in this chapter offered an opportunity to investigate the phase dependence and the nonlinear dynamics of singular beams. In practice, a

limiting factor is the beam power as beam shaping is inevitably lossy, and the four-wave mixing efficiency decreases with increasing ℓ due to a reduced overlap of the pump and and generated beams' wavefunctions (for details, see Section 6.3 and the last graph in Figure 6.12). In 2010 a fibre-coupled tapered amplifier was installed on the blue light experiment by Dr. Arnold, raising the power from 40 mW to about 140 mW of clean $\mathrm{TEM}_{0,0}$ light in each pump beam. These ideal experimental conditions allowed us to examine the transfer of orbital angular momentum to the up-converted beam. The first preliminary measurements presented in this thesis provided clear evidence that the generated blue beam carries orbital angular momentum.

Due to the limited availability of the tapered amplifier, only a week could be allotted to this investigation. During this period, Dr. Franke-Arnold and I devised a setup to be fitted into the blue light experiment, for which we got guidance and equipment from Dr. Arnold. I then carried out the measurements presented in this chapter. Because of the short amount of time spent on this study, the results are, as yet, preliminary, and many questions are still left to be answered.

Several modifications had to be made to the original setup, so the full experimental apparatus is detailed in the first part of this chapter. The experimental results and their interpretation are given in the second part, in which some future research will also be proposed.

6.1 Experimental apparatus

The two pump beams (780 nm and 776 nm) from the ECDLs which were previously focused directly into the Rubidium vapour were, for this new set of experiments, overlapped and coupled into the fibre input of a tapered amplifier (TA). Their state of polarisation was cleaned with a polarising beam splitter just before the coupling stage. The TA output power is proportional to the input, so the coupling had to be optimised. The TA's fibre output was collimated, and measured to be ≈280 mW corresponding to about 130 mW of 780 nm and 150 mW of 776 nm of perfectly collinear pumping light, purely in the $TEM_{0,0}$ mode.

In order to generate a beam with a charge ℓ vortex, a phase step of $2\pi\ell$ must be introduced in the beam. This can be done using a spiral phase plate or a transmission hologram on a photographic plate, but we had the possibility to use an electronically addressed Hamamatsu spatial light modulator (SLM), which is a programmable diffractive element. SLMs consist of an optically or electronically addressed array of liquid crystal pixels. The orientation of the crystals in each pixel determines the local phase-shift imposed upon the light. SLMs allow the phase and the intensity of a reflected beam to be engineered for flexible or real-time beam shaping. They are commonly used in transmission in data projectors, but reflective SLMs are often more suitable due to the difficulty of designing transparent electronic systems. The hologram displayed on the SLM for the generation

of a LG mode with $p = 0$ and $\ell = 1$ is shown and described in Figure 6.2. The display on the SLM was computer-controlled, using a LabView interface. The programme used was written by Mr. G. Walker, using the "wavetrace" set of libraries written by Dr. J. Courtial.

Figure 6.2: Hologram on SLM screen. Left: a phase grating, equivalent to a prism due to phase-wrapping, is used to separate the diffracted from the undiffracted light. The number of lines determines the angle between the 0^{th} and the 1^{st} orders of the SLM. Middle: the phase and intensity of a LG mode are added to the phase grating. Right: the final hologram is obtained from the phase-wrapped sum of the two previous holograms and displayed on the SLM using a grayscale of 0 to 255.

The beam was expanded by a factor of 5 (Fig. 6.3) to fill about 2/3 of the SLM screen. The diffraction efficiency was a little more than a third, as the total LG beam power was measured to be around 100 mW. The resulting beam was thus made up of 45 mW of 780 nm and 55 mW of 776 nm, with each pump carrying one unit of OAM ($\ell_{780} = 1$, $\ell_{776} = 1$). This "dichroic" LG beam was then re-collimated to its original size, and focused into the Rubidium vapour to a waist of 60 μm ($z_R \approx 1.5$ cm), yielding .2 mW of blue light. The 780 nm beam showed a significant amount of Kerr lensing around

the optimum frequency for blue light generation, as shown in Figure 6.4 for two different frequencies a few 100 MHz apart. These two pictures show quite clearly how self-focussing and self-defocussing deteriorate the mode overlap, thus decreasing the conversion efficiency (see Chapter 5).

Some astigmatism, mainly introduced by the off-centre collimating lens after the SLM (marked in red in Figure 6.3) and, to a lesser extent by the SLM itself, was corrected for using Zernike polynomials on the SLM [Lov97]. All pictures were taken using a full colour QCam Micropublisher 3.3 Charge Coupled Device (CCD) camera.

The obtained blue beam was finally expanded, and its phase was analysed using a ring interferometer. The full experimental setup is shown in Figure 6.3.

Note that because of the very short amount of time assigned to the experiment, I did not take enough care over the quality of the pictures which often turn out saturated, show colour scales which are not linear with input, and have a negative offset. This amounts to unrealistically sharp images that are not representative of the real image contrast.

6.1.1 Independent control over ℓ_{780} and ℓ_{776}

The ideal, most unambiguous situation however consists in shaping only one of the two pumps as a $LG_{0,1}$ as photons cannot carry half a unit of orbital angular momentum. Another setup was therefore also attempted: the 776 nm beam was coupled into the tapered amplifier and shaped, whereas

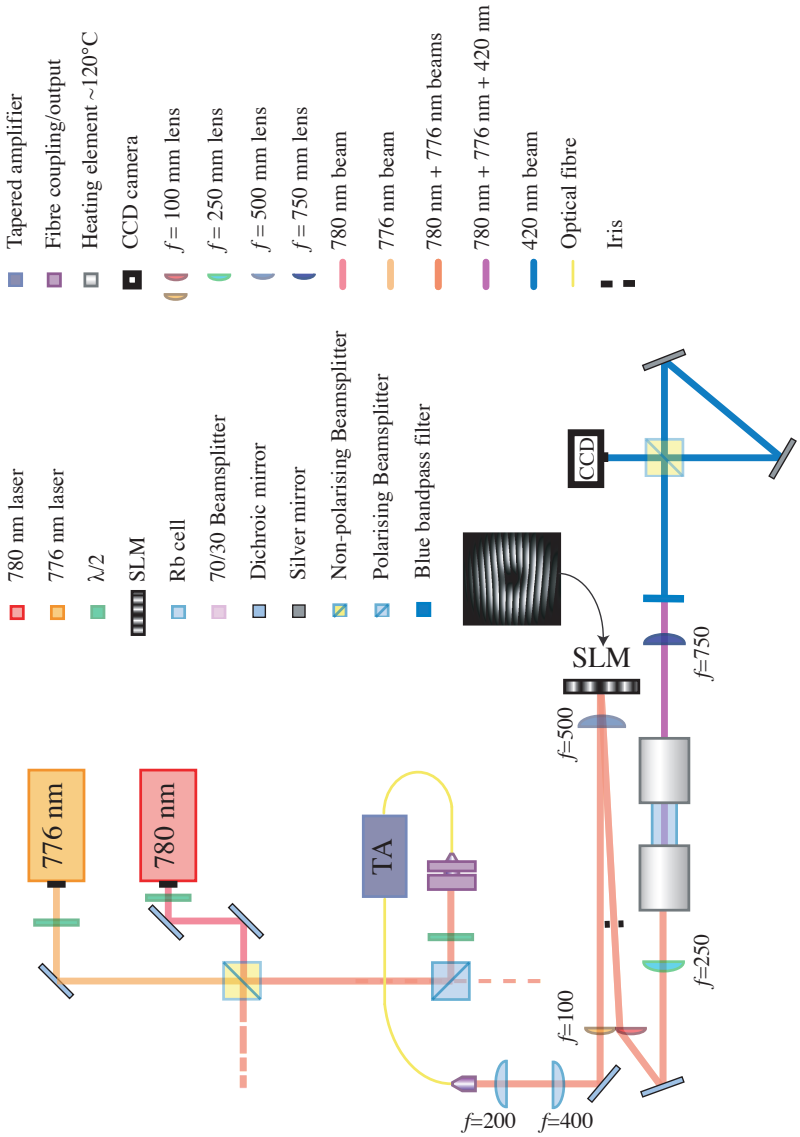

Figure 6.3: Experimental setup. The 780 nm saturated absorption spectroscopy has been omitted for clarity. For details on saturated absorption spectroscopy, see Chapter 3

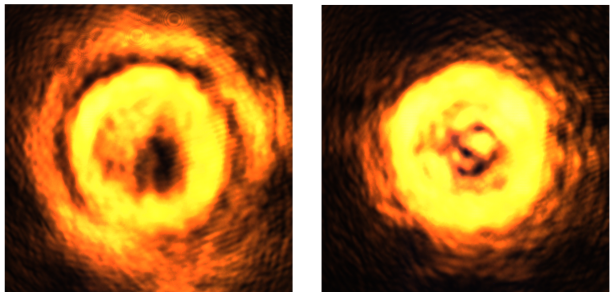

Figure 6.4: Concentric 780 nm and 776 nm beams. Left: 780 nm beam outside 776 nm beam. Right: 780 nm beam inside 776 nm beam.

the 780 nm was overlapped directly from the output of the laser (which is close to a $TEM_{0,0}$), as shown in Figure 6.5. It was found that the angle and overlap between the two pump beams critically modified the shape of the generated blue beam, making the interpretation more difficult. Irises were used to align the two pump beams and the alignment was performed several times. For the best achieved alignment (yielding the largest output power) the blue beam showed two lobes, which could be more or less pronounced (Figure 6.5, top, left). This intensity modulation of the beam's cross-section could be attributed to aberrations in the optical system, simulated in Figure 6.5, right (for more details, see Sec.6.2). Due to time constraints, the phase structure of the output beam could, unfortunately, not be determined.

Because of the ambiguity of the interpretation of the profile due to its sensitivity to alignment, the analysis presented in the following section concerns exclusively the cases $\ell_{780} = 1, \ell_{776} = 1$ or $\ell_{780} = 0, \ell_{776} = 0$.

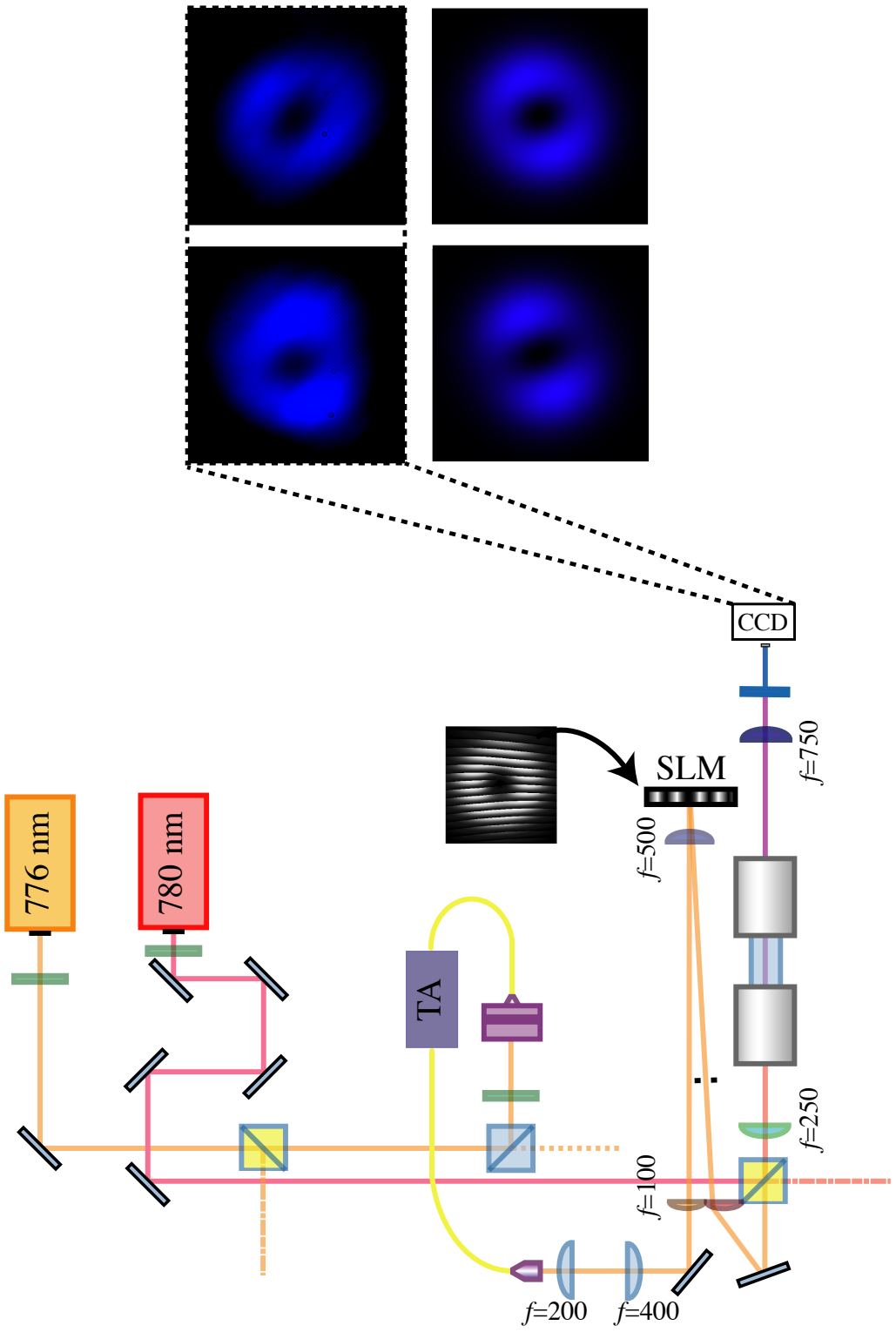

Figure 6.5: Setup and output blue beams for $\ell_{780} = 0$ and $\ell_{776} = 1$, experimental (left) and simulated profiles (right). For details regarding the simulated profiles, see Sec. 6.2.

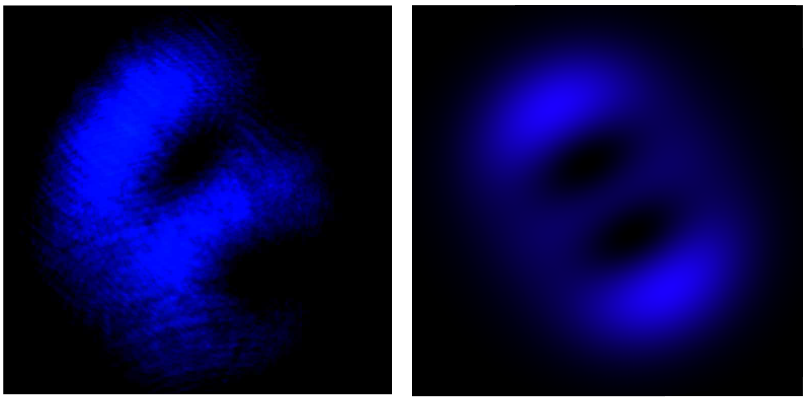

Figure 6.6: $\ell = 2$ beam with charge 2 vortex split into two charge 1 vortices. Left: experiment. Right: simulated far field of an astigmatic $p = 0, \ell = 2$ mode

6.2 Laguerre-Gaussian blue beam analysis

6.2.1 Aberration correction

Without aberration correction, the intensity profile of the blue beam shows two holes corresponding to two vortices. Aberrations commonly found in optical systems are known to displace the vortices from the centre of the beam and to distort the beam profile. Astigmatism, in particular, changes the relative Gouy phase in two opposite directions, and therefore results in modes which look like Hermite-Gaussian modes. An experimental picture of an uncorrected beam and a simulated beam obtained by adding astigmatism and propagating the mode are shown in Figure 6.6.

The aberrations were corrected by manually adjusting the phase profile imprinted on the SLM to obtain an input beam as circular and symmetric

as possible (Figure 6.7, left) . After correction, a roughly circular output beam exhibiting four lobes was observed (Figure 6.7, middle). The origin of these four lobes is not understood. It could be argued that filamentation due to the non-zero Kerr nonlinearity of the vapour is the source of the lobes in the profile [SF98] [VGI+06], but this seems unlikely as the number of lobes only seemed to correlate with the charge of the input beams and not with their power. More thorough investigation of the possible power dependence of the number of lobes would however be required to definitely rule it out. Another possibility would be a superposition of $\ell_{420} = 2$ and $\ell_{420} = -2$, but this would imply a significant contribution of $\ell_{IR} = 4$ which is unlikely given the negligible mode overlap (see Section 6.3).

Laguerre-Gaussian modes can be expressed as the sum of Hermite-Gaussian modes [BAvdVW93]. In particular, a $LG_{0,2}$ can be expressed as a weighted sum of $HG_{2,0}$, $HG_{0,2}$, and $HG_{1,1}$ The simulated profile on the right of Figure 6.6 shows a deviation of the phase from the ideal values of 20% for $HG_{1,1}$, and of 30% for $HG_{2,0}$. This theoretical mode resembles the experimental mode, but the physical origin of such a large phase variation in the experimental system is unknown.

6.2.2 Interferometric measurements

As mentioned previously, an unambiguous determination of the output mode requires knowledge of the phase and of the intensity profile. An

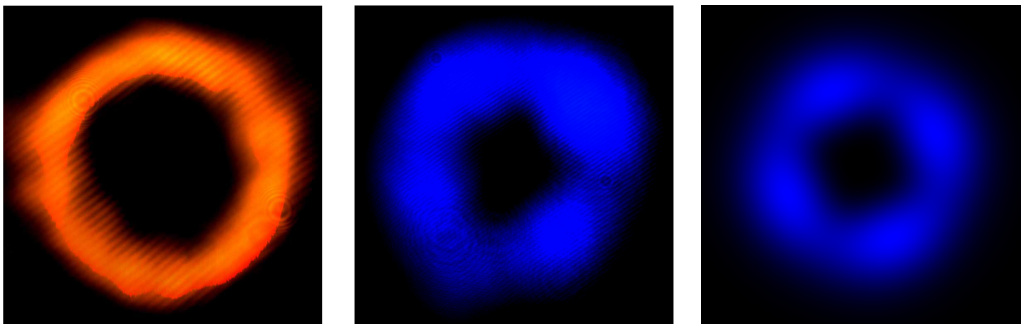

Figure 6.7: Left: Input "dichroic" beam. Middle: experimental blue output beam for best astigmatism correction. Right: theoretical beam cross section for a variation of the phase of 20% for $HG_{1,1}$, and of 30% for $HG_{2,0}$.

ideal setup to determine the charge of Laguerre-Gaussian beams could be a Mach-Zehnder interferometer with a Dove prism in one of the two arms. Indeed, a Dove prism flips the image along one axis, as shown in Figure 6.8, thus changing the sign of ℓ. The interferogram would then exhibit 2ℓ lobes. Only one beamsplitter for 420 nm was available at the time, so the vertical flip of the phase was performed using a ring interferometer. The image flip performed by the ring interferometer can be understood by following the purple and red rays shown on Figure 6.8.

Ring interferometers are quite particular since there is an infinite number of paths the light can take (0, 1, 2, ...,n, ... times around the ring), showing multiple spots when the interferometer was not aligned, and multiple wave interference when inaccurately aligned (Figure 6.8, inset). When exactly aligned, the resulting amplitude interference is given by:

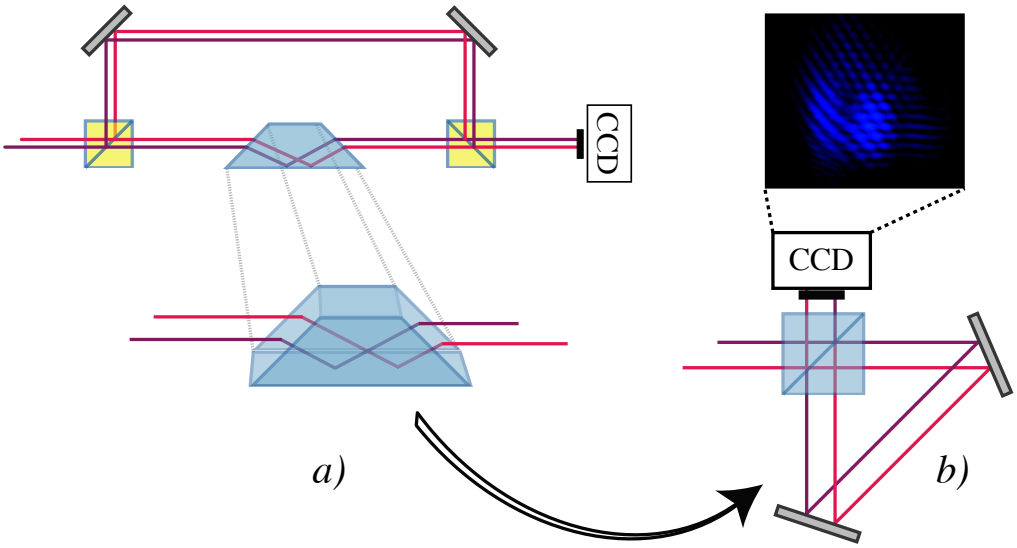

Figure 6.8: Left: a Mach-Zehnder interferometer with a Dove prism in one of the two arms is an ideal setup to analyse the OAM carried by the blue beam. Right: the same measurement can be performed in a ring interferometer at the price of a decreased visibility due do the infinite number of paths the light can take. The inset picture shows a multiple wave interferogram obtained with a misaligned ring interferometer.

$$A_{out} \propto \sum_{n=0}^{\infty} (-1)^{n+1} \frac{1}{2^{n+1}} e^{in\phi} = -\frac{1}{2 + e^{i\phi}} \tag{6.2}$$

The phase-dependent intensity is then:

$$|A_{out}|^2 \propto \frac{1}{5 + 4\cos\phi} \tag{6.3}$$

fwhich has a maximum visibility (no losses) of about 82% and results in a distortion of the ideal interferometric fringe profile.

A satisfactory alignment yielded the interferograms shown on the left hand side, at the bottom of Figure 6.9. To check the results, a test was run with two Gaussian $p_{780,776} = 0, \ell_{780,776} = 0$ and two Laguerre-Gaussian $p_{780,776} = 0, \ell_{780,776} = 1$ pump beams, both for aligned and misaligned interferometer.

Both aligned and misaligned cases yield interferograms which indicate an $\ell_{420} = 2$ beam from $\{\ell_{780} = 1, \ell_{776} = 1\}$ pumping, as shown with theoretical profiles in Figure 6.9. To double check that the interferometer gave the results we expected, the interferometric pattern was measured for Gaussian pump beams. As expected, the generated mode showed straight fringes in the misaligned interferometer, which turned into a single spot as the interferometer was aligned (Figure 6.9, top). A rotation of the fringes was also observed upon the slightest change in the path length (imposed by lightly touching the mirror mounts).

With an aligned interferometer a speedy measurement of the behaviour of the interference fringes with 776 nm beam detuning was performed. The crossed fringes were expected to rotate smoothly with 776 nm detuning, as the blue beam frequency, and thus the phase picked up after a round trip in the ring interferometer was expected to vary accordingly. This was however observed not to be the case. Instead, a curious switching from an otherwise stable pattern to another occurred as the beam was continuously tuned across the emission line. A movie of this phenomenon was taken, some snapshots of which are depicted in Figure 6.10.

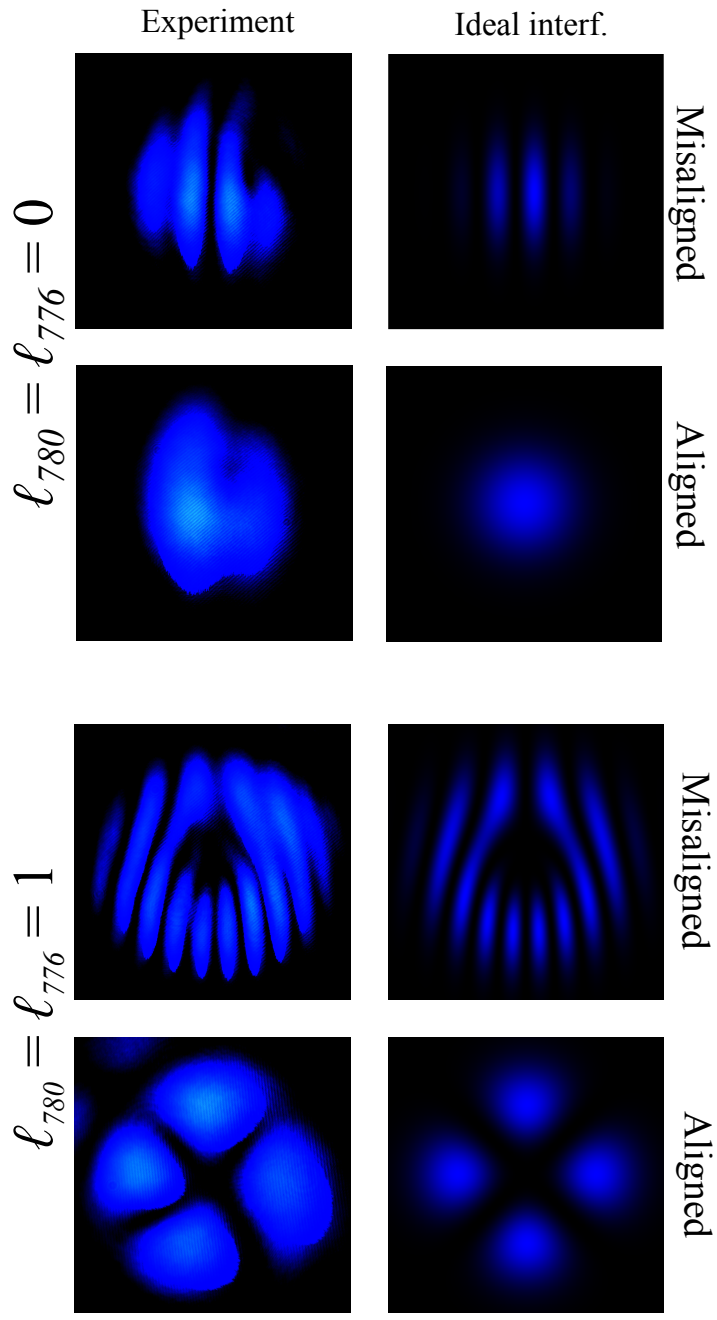

Figure 6.9: Blue output beams, experiment and simulations. Top: $\ell_{780} = \ell_{776} = 0$. Bottom: $\ell_{780} = \ell_{776} = 1$. Two interference patterns were taken for each combination of $\{\ell_{780}, \ell_{776}\}$: the top figure is obtained with a slightly misaligned interferometer, and the bottom figure with an aligned interferometer.

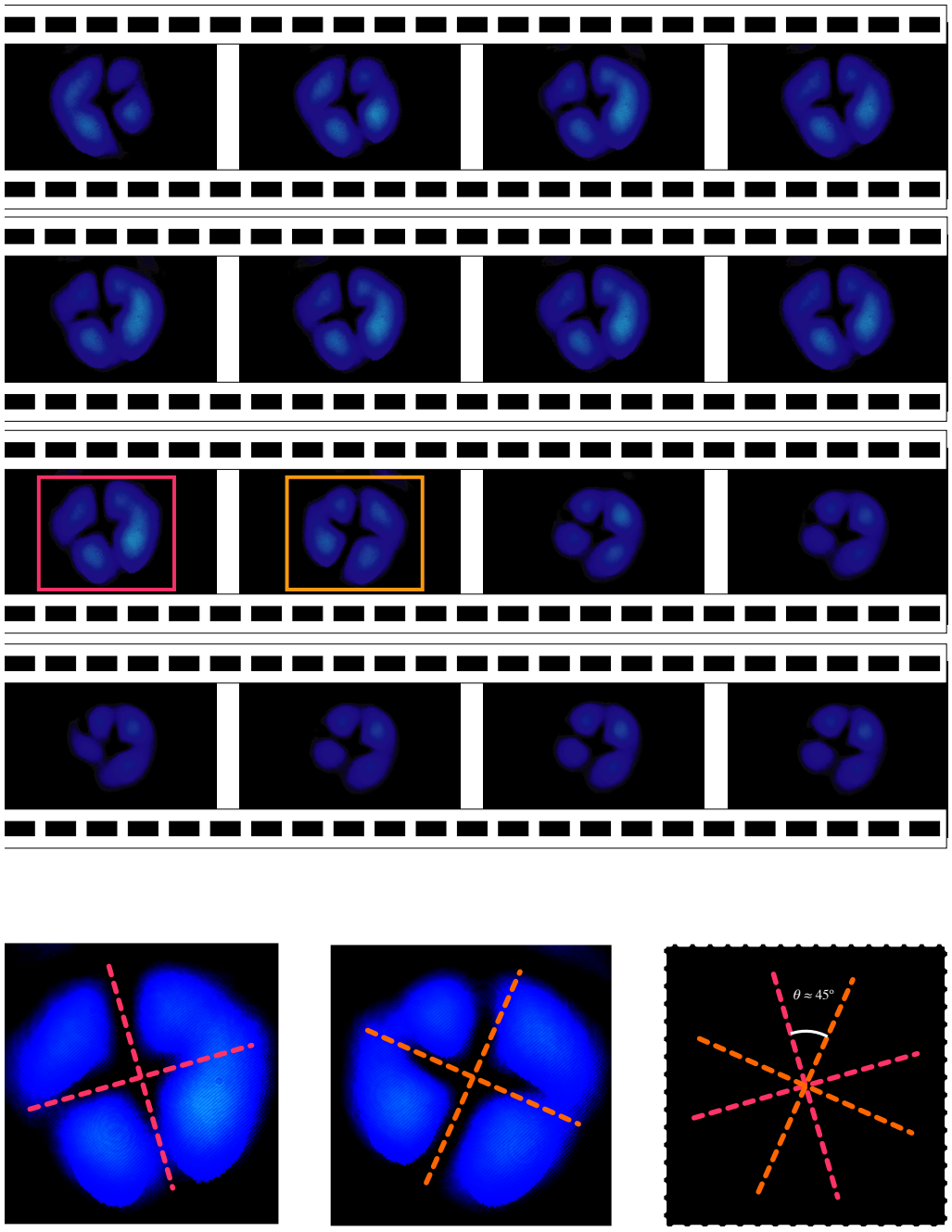

Figure 6.10: Top: "movie" of the interferogram as a function of 776 nm beam detuning. The fringes do not change position as the beam is detuned, until the fringe angle suddenly switches by about 45°. Bottom: In the ring interferometer whose path length difference is about 50 cm, a shift of 45° corresponds to a frequency change of about 1.8 GHz.

The pictures of the two fringe positions in Figure 6.10 show a rotation of $45\pm5°$, implying a frequency jump corresponding to a phase jump of about π between the two paths of the interferometer. For a ring interferometer of path length difference $\Delta L \approx 50\,\text{cm}$, the frequency jump is estimated to be 1.8 GHz. The physical origin of this frequency jump is unknown at the date of submission of this thesis. A measurement of the absolute frequency of the 420 nm beam would allow this phenomenon to be to investigated.

These preliminary results convincingly indicate that all the orbital angular momentum is carried by the blue beam. Measuring the beam profile of the infrared would at this stage be particularly relevant. In further work, the glass Rubidium cell will be replaced with a quartz cell to allow transmission of the infrared.
A question then arises: why should all the OAM be carried by the blue beam and none by the infrared?

6.3 All the OAM in the blue beam

Naively one could think that the orbital angular momentum should be distributed between the two emitted beams, but this is evidently not the case in this experiment. It should however be borne in mind that the two emitted beams differ greatly by their wavelength: for a given Rayleigh range, the waist w_{IR} of the infrared beam is $\sqrt{\lambda_{IR}/\lambda_{420}} = 3.5$ times larger than that of the blue beam.

In frequency conversion experiments it has commonly been observed that the best conversion efficiency is achieved when the confocal parameters (twice the Rayleigh range) of the beams are matched [Boy03]. Assuming that this experiment is no exception, it is informative to notice that the waist of a beam of wavelength λ scales with $\sqrt{\lambda}$ and that the radius of maximum intensity of a beam with orbital angular momentum ℓ scales with $\sqrt{\ell}$. For two beams of wavelengths $\lambda_{IR} = 5\,\mu$m and $\lambda_{blue} = 420\,$nm and a total orbital angular momentum $\ell_{780} + \ell_{776} = 2$, the best transverse overlap is achieved for $\ell_{IR} = 0$ and $\ell_{blue} = 2$. The overlap of the various profiles at the waist is shown in Figure 6.11.

It was shown that the position dependence of the field mode only determines the selection rules of external variables [vEN94], so it is legitimate to assume that the overlap between the initial and final states of the system composed of the coupled atoms and field reduces to the overlap of the fields only. Neglecting the refractive effects of the vapour, assuming that the conserved quantity in the process is the confocal parameter $\frac{2\pi}{\lambda}w_0^2$, and given that both pump beams carry an orbital angular momentum of $\hbar\ell$, the overlap is found to be the largest for a Gaussian infrared and $\ell_{420} = 2$. A plot of the numerical computation of the integral of the pump and generated fields over the transverse plane with different values of ℓ, and for total angular momenta $\ell = 1$ and $\ell = 2$ is shown in the top and middle graphs of Figure 6.12. The graph at the bottom of the figure shows the relative overlap of the following combinations of modes:

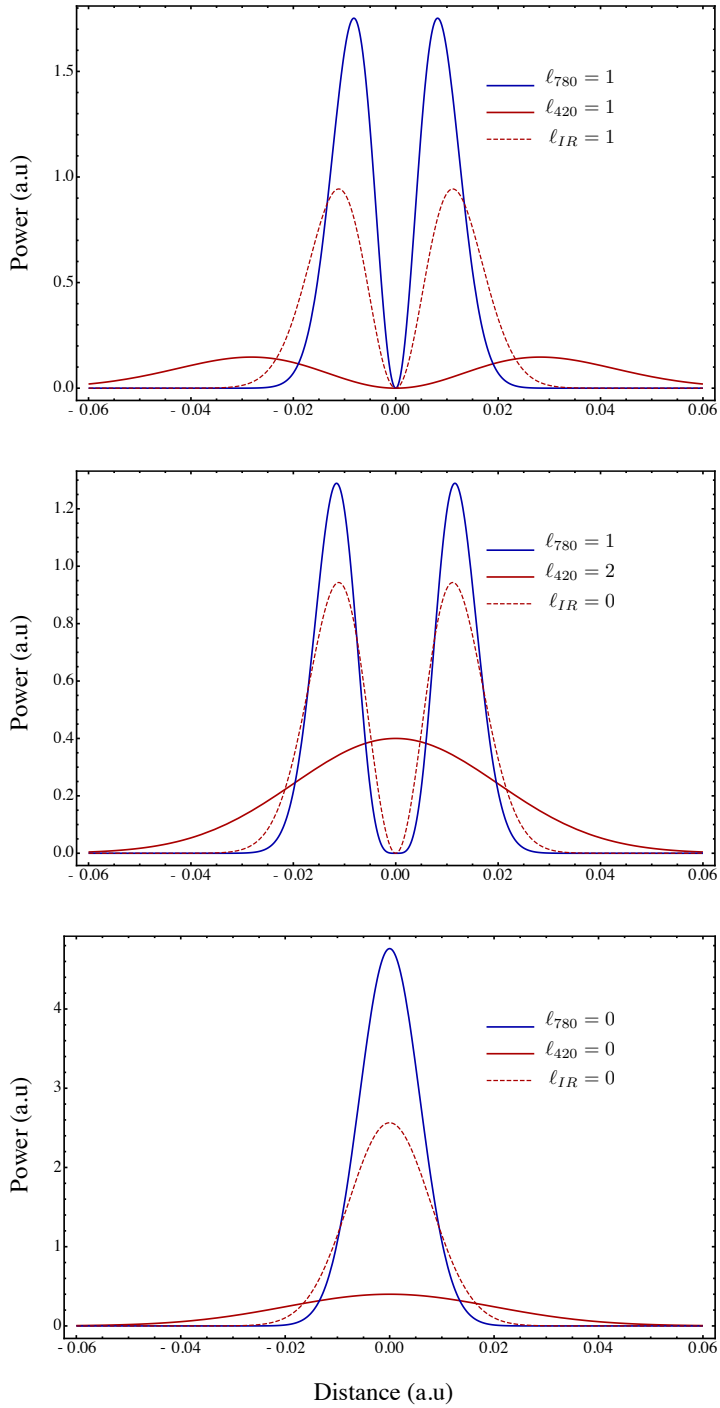

Figure 6.11: Field cross-sections for three cases of orbital angular momentum conservation. Top: $\ell_{780} = \ell_{776} = 1$, $\ell_{IR} = 1$, $\ell_{420} = 1$. Middle: $\ell_{780} = \ell_{776} = 1$, $\ell_{IR} = 0$, $\ell_{420} = 2$. The bottom graph shows the overlap of Gaussian beams $\ell_{780} = \ell_{776} = 0$, $\ell_{IR} = 0$, $\ell_{420} = 0$.

$\{\ell_{780} = 0, \ell_{776} = 1, \ell_{IR} = 0, \ell_{420} = 1\}$, $\{\ell_{780} = 1, \ell_{776} = 1, \ell_{IR} = 0, \ell_{420} = 2\}$ and $\{\ell_{780} = 0, \ell_{776} = 0, \ell_{IR} = 0, \ell_{420} = 0\}$, illustrating the decreased efficiency with increasing $\ell_{780} + \ell_{776}$.

The integral of the mode overlap I over the twice the Rayleigh range according to Equation 6.4 favours the combination $\{\ell_{780} = 1, \ell_{776} = 1, \ell_{IR} = 0, \ell_{420} = 2\}$ against $\{\ell_{780} = 1, \ell_{776} = 1, \ell_{IR} = 1, \ell_{420} = 1\}$ by a factor of 6, and $\{\ell_{780} = 0, \ell_{776} = 1, \ell_{IR} = 0, \ell_{420} = 1\}$ against $\{\ell_{780} = 0, \ell_{776} = 1, \ell_{IR} = 1, \ell_{420} = 0\}$ by a factor of 10.

$$I = |\int_{-z_R}^{+z_R} \int_{-\infty}^{+\infty} \int_{-\infty}^{+\infty} E_{780} E_{776} E_{IR}^{*} E_{420}^{*} dx dy dz|^2 \tag{6.4}$$

In Section 6.2.1 we showed that the output blue beam exhibited four lobes in its intensity profile. This structure is characteristic of a superposition of $\ell = 2$ and $\ell = -2$ beams, but the overlap of $\{\ell_{780} = 1, \ell_{776} = 1, \ell_{IR} = 4, \ell_{420} = -2\}$ is 4 orders of magnitude smaller than that of $\{\ell_{780} = 1, \ell_{776} = 1, \ell_{IR} = 0, \ell_{420} = 2\}$, thus making this combination very unlikely. The absence of the $\ell = -1$ mode in the pump beams should be checked interferometrically.

6.4 Summary and further work

The interest in phase-dependent effects as well as orbital angular momentum conservation in the blue light experiment led us to investigate the frequency up-conversion of Laguerre-Gaussian beams. This preliminary study

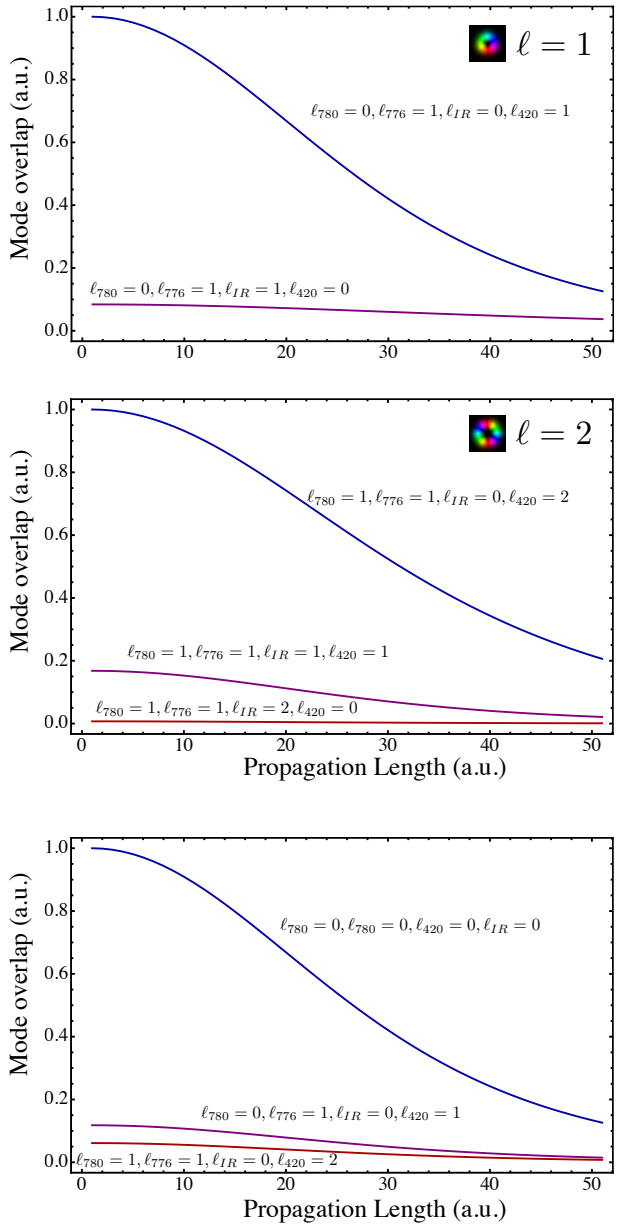

Figure 6.12: Field overlap ($|\int_{-\infty}^{+\infty}\int_{-\infty}^{+\infty} E_{780}E_{776}E_{IR}^{*}E_{420}^{*}dxdy|^2$) as a function of propagation length. Top: pumping with $\ell_{780} = 0, \ell_{776} = 1$ favours the combination $\ell_{IR} = 0, \ell_{420} = 1$ over $\ell_{IR} = 1, \ell_{420} = 0$. Middle: pumping with $\ell_{780} = 1, \ell_{776} = 1$ favours $\ell_{IR} = 0, \ell_{420} = 2$ over $\ell_{IR} = 1, \ell_{420} = 1$ and $\ell_{IR} = 2, \ell_{420} = 0$. The bottom graph shows the relative overlap of the following fields: $\ell_{780} = \ell_{776} = 0, \ell_{IR} = 0, \ell_{420} = 0$ (blue), $\ell_{780} = 0, \ell_{776} = 1, \ell_{IR} = 0, \ell_{420} = 1$ (purple), and $\ell_{780} = \ell_{776} = 1, \ell_{IR} = 0, \ell_{420} = 2$ (red)

suggests that due to the large frequency difference between the two generated beams (5 μm and 420 nm), the blue beam is the sole carrier of the converted orbital angular momentum. This should be confirmed in further work by monitoring the profile of the infrared beam. An interferometric analysis of the blue beam in a Mach-Zehnder interferometer is also one of the measurements that will be performed for an unambiguous measurement of ℓ_{420}.

The physical processes leading to the transfer of OAM from the pump beams to the blue light have not yet been established. In Ref. [SB03], the transfer of orbital angular momentum in four-wave mixing was ascribed to the generation of a "population grating". This spatially varying population is equivalent to a refractive index grating which diffracts the incident light beam. This can only occur if the pump beams have the same polarisation, so it would be interesting to study the polarisation dependence of the OAM transfer from the pump beams to the generated beams.

Further attention should also be directed towards the measurement of the frequency of the generated blue light as a function of the 776 nm pump frequency. Indeed, the frequency of the blue light was expected to vary smoothly with 776 nm detuning (δ_{776}), but this was observed not to be the case. The interference fringes obtained from a ring interferometer switched from an otherwise stable position to another when δ_{776} was scanned across the blue light emission line. Determining whether this phenomenon also occurs for Gaussian pump beams, and correlating the fringe position with

the absolute 776 beam frequency would offer important clues to understand this phenomenon.

6.5 References

[ABSW92] L. Allen, M.W. Beijersbergen, R.J.C. Spreeuw, and J.P. Woerdman. Orbital angular momentum of light and the transformation of Laguerre-Gaussian modes. Physical Review A, 45:8185–8189, 1992.

[ARC+06] M.F. Andersen, C. Ryu, P. Clad, V. Natarajan, A. Vaziri, and K. Helmerson. Quantized rotation of atoms from photons with orbital angular momentum. Physical Review Letters, 97:170406, 2006.

[BAvdVW93] M.W. Beijersbergen, L. Allen, H.E.L.O. van der Veen, and J.P. Woerdman. Astigmatic laser mode converters and transfer of orbital angular momentum. Optics Communications, 96:123–132, 1993.

[Boy03] R.W. Boyd. Nonlinear Optics. Academic Press. Elsevier Science, second edition, 2003.

[BTFL06] S. Barreiro, J.W.R. Tabosa, H. Failache, and A. Lezama. Spectroscopic observation of the rotational Doppler effect. Physical Review Letters, 97:113601, 2006.

[DKT05] A.S. Desyatnikov, Y.S. Kivshara, and L. Torner. Optical vortices and vortex solitons. Progress in Optics, 47:291–391, 2005.

[FABPA02] S. Franke-Arnold, and S.M. Barnett, M.J. Padgett, and L. Allen. Two-photon entanglement of orbital angular momentum states. Physical Review A, 65:033823, 2002.

[FK08] S. Feng and P. Kumar. Spatial symmetry and conservation of orbital angular momentum in spontaneous parametric down-conversion. Physical Review Letters, 101:163602, 2008.

[JL92] G.A. Swartzlander, Jr. and C.T. Law. Optical vortex solitons observed in Kerr nonlinear media. Physical Review Letters, 69:2503–2506, 1992.

[Lov97] G.D. Love. Wave-front correction and production of Zernike modes with a liquid-crystal spatial light modulator. Applied Optics, 36:1517–1520, 1997.

[MSF92] G.S. McDonald, K.S. Syed, and W.J. Firth. Optical vortices in beam propagation through a self-defocussing medium. Optics Communications, 94:469–476, 1992.

[MVWZ01] A. Mair, A. Vaziri, G. Weihs, and A. Zeilinger. Entanglement of the orbital angular momentum states of photons. Nature, 412:313–316, 2001.

[OMTT08] C.I. Osorio, G. Molina-Terriza, and J.P Torres. Correlations in orbital angular momentum of spatially entangled paired photons generated in parametric down-conversion. Physical Review A, 77:015810, 2008.

[SB03] J.W.R. Tabosa S. Barreiro. Generation of light carrying orbital angular momentum via induced coherence grating in cold atoms. Physical Review Letters, 90:133001, 2003.

[SF98] D.V. Skryabin and W.J. Firth. Dynamics of self-trapped beams with phase dislocation in saturable Kerr and quadratic nonlinear media. Physical Review E, 58:3916–3930, 1998.

[TP99] J.W.R. Tabosa and D.V. Petrov. Optical pumping of orbital angular momentum of light in cold Cesium atoms. Physical Review Letters, 83:4967–4970, 1999.

[vEN94] S.J. van Enk and G. Nienhuis. Commutation rules and eigenvalues of spin and orbital angular momentum of radiation fields. Journal of Modern Optics, 41:963–977, 1994.

[VGI+06] L.T. Vuong, T.D. Grow, A. Ishaaya, and A.L. Gaeta, G.W. t Hooft, and E.R. Eliel, and G. Fibich. Collapse of optical vortices. Physical Review Letters, 96:133901, 2006.

CHAPTER 7

Conclusion

7.1 Summary

The work presented during the course of this thesis was centred around quantum interference in four-level linkages, with the understanding of the interaction between light and atoms as its primary motivation.

In the first part of this thesis, the realisation of a magneto-optical trap was presented. An explanation of the principles underlying the trapping scheme, as well as some simplified models to deduce the physical properties of the trapped atoms were detailed in Chapter 2. This was followed by a demonstration of the experimental realisation of the trap in Chapter 3. Around 8×10^8 atoms were trapped, with a density estimated to be $\approx 10^9$ atoms per cubic centimetre.

The second part was dedicated to the investigation of the generation

of 420 nm coherent radiation via a four-wave mixing process whereby two pump beams at 780 nm and 776 nm were overlapped and focussed into a hot Rubidium cell, yielding up to 1 mW of 420 nm light. This project started as a side-project, joint between the Optics group at Glasgow University and the group of Photonics at the University of Strathclyde. The interesting, though puzzling effects that were subsequently observed and the complexity of the task of modeling the system meant that this project soon became the main motive of this thesis.

On the experimental side, presented in Chapter 4, several unexpected effects were observed. The most striking was perhaps the efficiency of the non-linear process as for the optimal condition, one in six absorbed 776 nm photons were converted to the 420 nm beam. The dependence of the conversion efficiency on the pump frequencies was mapped for two Rubidium pressures which gave rise to two different behaviours. In the case of a low Rubidium pressure (10^{-4} mbar), the 420 nm coherent light emission more or less followed the lines of two-photon resonance, whereas a high pressure (9×10^{-4} mbar) lead to the appearance of a "sweet spot" and the inhibition of the process everywhere else. The existence of such a locus was studied theoretically and was ascribed to a favourable phase-matching condition. Finally, the four-wave mixing process proved critically polarisation-dependent, as pumping with counter-circularly polarised beams inhibited the generation of blue light by a factor of 500 with respect to the co-circular case.

Most of these effects could be reproduced qualitatively by an evaluation of the steady states of the optical Bloch equations and an analysis of phase-matching in the vapour demonstrated in Chapter 5. Phase-matching was found to be most likely to be responsible for the peak observed for high Rubidium pressure.

An interesting result that may be tested experimentally was that the best match of theoretical plots with the experimental data was obtained for Rabi frequencies corresponding to the pump intensities present at the entrance of the cell. It may be a coincidence, but it is striking to note that the experiment shows that the blue light generation coincides with the two-photon absorption measured at the entrance of the cell. This might suggest that the maximum blue light intensity is obtained for the condition of two photon resonance at the entrance of the cell. Two interpretations were then envisaged, as this condition either maximises the propagation length in the cell, or stems from the absorption of the pump beams upon propagation.

The last chapter presented a study of the conversion of phase structure in the four-wave mixing process. The pump beams were shaped as Laguerre-Gaussian modes, characterised by the azimuthal dependence of their transverse phase structure, as well as the fact that they carry orbital angular momentum. A transfer of the input orbital angular momentum to the 420 nm beam was indeed observed, and in fact all the orbital angular momentum seemed to be carried by the 420 nm beam. The phase structure of the blue beam pumped with either $\{\ell_{780} = 0, \ell_{776} = 0\}$ or

$\{\ell_{780} = 1, \ell_{776} = 1\}$ was measured interferometrically, yielding $\ell_{420} = 0$ and $\ell_{420} = 2$, respectively. Although the infrared beam was not measured, it can be inferred by conservation of orbital angular momentum that $\ell_{IR} = 0$. This first came as a surprise, but could be later explained from considerations of mode overlap.

7.2 Future work and open questions

There is, of course, a lot of work to be done on the Glasgow trap, as it is the beginning of the atom trapping project in the Optics group. The work on the MOT is ongoing, and currently pursued by Mr. G. Walker who is working on SLM-assisted novel trapping geometries. The next important step for this experiment will be the realisation of optical molasses, along with the measurement of the temperature of the atomic cloud. Future work will include the measurement of phase-dependent population transfer and the storage of phase structure within the atomic populations.

The most important missing data to understand the "blue light" experiment is clearly the absolute frequency of the 420 nm beam. The steady states simulations suggest that the infrared radiation is resonant with the bare $6P_{3/2} \rightarrow 5D_{5/2}$ transition, but this has yet to be verified experimentally. In Chapter 6 we saw that tuning the 776 nm pump induced a sudden frequency shift of the 420 nm beam instead of the smooth change we expected (Figure 6.10). It would be interesting to simultaneously measure

the absolute frequency of the 420 nm beam and the position of interference fringes. This measurement could be performed in the near future.

As mentioned in Section 5.4, we suspect that the frequency dependence of the blue light emission lines for low pressure may depend on the position of the focus within the cell, as well as on the pump intensity. Taking the two-dimensional data shown on Figure 4.5 for different pump intensities and/or focus positions within the cell would allow the confirmation or disproval of our hypothesis.

We believe that the elusive polarisation dependence of the blue light generation could be explained by evaluating the steady state of a system including the full hyperfine structure (see Appendix A) and the corresponding Clebsch-Gordan coefficients. The joint effects of optical pumping and destructive interference between pathways may be sufficient to explain the contrast between co- and counter-circular pumping observed experimentally.

A simulation of the propagation of the fields in the atomic medium is an obvious extension to be made to the model, as it would allow the depletion of the pumps and the reabsorption of the blue beams to be taken into account. It would also provide some insight into the behaviour of the phase of the fields upon propagation. A theoretical investigation of the phase-matching condition for the non-degenerate, spontaneously arising four-wave mixing process in this system would also be very interesting as it holds many similarities with spontaneous parametric down conversion. It

may be envisaged that such a study could lead to the use of this process for a source of entangled photons.

Finally, the measurements of conversion of phase structure and orbital angular momentum in the process will have to be taken again for a rigorous quantitative analysis. Also, a measurement of the transverse phase structure of the generated $5\,\mu$m beam would be of interest to confirm the conservation of orbital angular momentum in the four-wave mixing process.

APPENDIX A

Rubidium hyperfine structure

The hyperfine level splittings were calculated from the experimentally determined values of the magnetic dipole constant A and the electric quadrupole constant B according to the Equation A.1 which gives the hyperfine interaction energy as a function of F, I, J, A and B. K is defined as $K = F(F+1) - J(J+1) - I(I+1)$ for conciseness. The derivation of this expression can be found in Ref. [AIV77].

The values of A and B shown in Table A.1 were taken from Ref. [AIV77] for levels $5P_{3/2}$ and $6P_{3/2}$, and from Ref. [NBFM93] for $5D_{5/2}$, and the ground state splittings were taken from Ref. [AIV77].

$$W_F = \frac{1}{2}hAK + hB\frac{3/2K(K+1) - 2I(I+1)J(J+1)}{2I(2I+1)2J(2J+1)} \qquad \text{(A.1)}$$

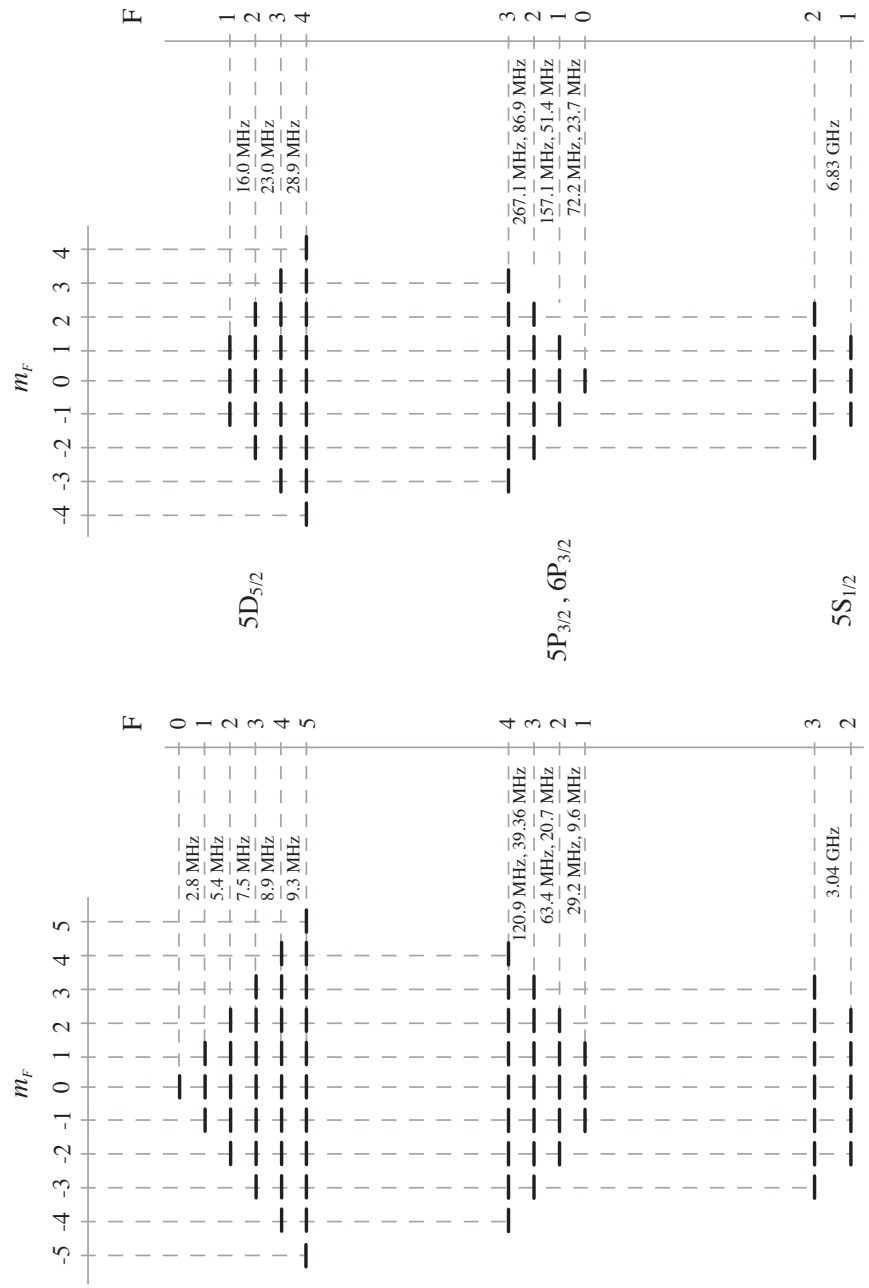
m_F
-5 -4 -3 -2 -1 0 1 2 3 4 5
F
0 1 2 3 4 5
2.8 MHz
5.4 MHz
7.5 MHz
8.9 MHz
9.3 MHz
120.9 MHz, 39.36 MHz
63.4 MHz, 20.7 MHz
29.2 MHz, 9.6 MHz
3.04 GHz
^{85}Rb
$5D_{5/2}$
$5P_{3/2}$, $6P_{3/2}$
$5S_{1/2}$
-4 -3 -2 -1 0 1 2 3 4
F
1 2 3 4
16.0 MHz
23.0 MHz
28.9 MHz
267.1 MHz, 86.9 MHz
157.1 MHz, 51.4 MHz
72.2 MHz, 23.7 MHz
6.83 GHz
^{87}Rb

Table A.1: Values of the magnetic dipole constant A and the electric quadrupole constant B for the calculation of the hyperfine levels splittings. Extracted from Refs. [AIV77, NBFM93]

Level (^{85}Rb)	A (MHz)	B (MHz)
$5P_{3/2}$	25.029(16)	26.032(70)
$6P_{3/2}$	8.16(6)	8.40(40)
$5D_{5/2}$	-2.1911(12)	2.6804(200)
Level (^{85}Rb)	A (MHz)	B (MHz)
$5P_{3/2}$	84.852(30)	12.611(70)
$6P_{3/2}$	27.674(28)	3.945(19)
$5D_{5/2}$	-7.4923(3)	1.2713(20)

A.1 References

[AIV77] E. Arimondo, M. Inguscio, and P. Violino. Experimental determinations of the hyperfine structure in the alkali atoms. Reviews of Modern Physics, 49:3175, 1977.

[NBFM93] F. Nez, and F. Biraben, R. Felder, and Y. Millerioux. Optical frequency determination of the hyperfine components of the $5s_{1/2}$-$5d_{3/2}$ two-photon transitions in rubidium. Optics Communications, 102:432–438, 1993.

Enhanced frequency up-conversion in Rb vapor

A. Vernier,[1] S. Franke-Arnold,[1] E. Riis,[2] and A. S. Arnold[2,*]

[1]*SUPA, Dept. of Physics and Astronomy, University of Glasgow, Glasgow G12 8QQ, UK*
[2]*SUPA, Dept. of Physics, University of Strathclyde, Glasgow G4 0NG, UK*
**a.arnold@phys.strath.ac.uk*

Abstract: We demonstrate highly efficient generation of coherent 420 nm light via up-conversion of near-infrared lasers in a hot rubidium vapor cell. By optimizing pump polarizations and frequencies we achieve a single-pass conversion efficiency of 260% per Watt, significantly higher than in previous experiments. A full exploration of the coherent light generation and fluorescence as a function of both pump frequencies reveals that coherent blue light is generated close to ^{85}Rb two-photon resonances, as predicted by theory, but at high vapor pressure is suppressed in spectral regions that do not support phase matching or exhibit single-photon Kerr refraction. Favorable scaling of our current 1 mW blue beam power with additional pump power is predicted.

OCIS codes: (190.4380) Nonlinear optics, four-wave mixing; (270.1670) Coherent optical effects.

References and links

1. F. Nez, F. Biraben, R. Felder and Y. Millerioux, "Optical frequency determination of the hyperfine components of the $5S_{1/2}$-$5D_{3/2}$ two-photon transitions in rubidium," Opt. Commun. **102**, 432–438 (1993).
2. M. J. Snadden, A. S. Bell, E. Riis and A. I. Ferguson, "Two-photon spectroscopy of laser-cooled Rb using a mode-locked laser," Opt. Commun. **125**, 70–76 (1996).
3. A. J. Olson, E. J. Carlson and S. K. Mayer, "Two-photon spectroscopy of rubidium using a grating-feedback diode laser," Am. J. Phys. **74**, 218–223 (2006).
4. M. Xiao, Y. Q. Li, S. Z. Jin and J. Gea-Banacloche, "Measurement of dispersive properties of electromagnetically induced transparency in rubidium atoms," Phys. Rev. Lett. **74**, 666–669 (1995).
5. S. D. Badger, I. G. Hughes and C. S. Adams, "Hyperfine effects in electromagnetically induced transparency," J. Phys. B **34**, L749–L756 (2000).
6. A. S. Arnold, J. S. Wilson and M. G. Boshier, "A simple extended-cavity diode laser," Rev. Sci. Instrum. **69**, 1236–1239 (1998).
7. M. S. Malcuit, D. J. Gauthier and R. W. Boyd, "Suppression of amplified spontaneous emission by the four-wave mixing process," Phys. Rev. Lett. **55**, 1086–1089 (1985).
8. S. M. Hamadani, J. A. D. Stockdale, R. N. Compton and M. S. Pindzola, "Two-photon resonant four-wave mixing and multiphoton ionization of cesium in a heat-pipe oven," Phys. Rev. A **34**, 1938–1943 (1986).
9. D. V. Sheludko, Simon C. Bell, R. Anderson, C. S. Hofmann, E. J. D. Vredenbregt, and R. E. Scholten, "State-selective imaging of cold atoms," Phys. Rev. A **77**, 033401 (2008).
10. H. Ohadi, M. Himsworth, A. Xuereb, and T. Freegarde, "Magneto-optical trapping and background-free imaging for atoms near nanostructured surfaces," Opt. Express **17**, 23003–23009 (2009).
11. A. I. Lvovsky, S. R. Hartmann and F. Moshary, "Omnidirectional superfluorescence," Phys. Rev. Lett. **82**, 4420–4423 (1999).
12. A. S. Zibrov, M. D. Lukin, L. Hollberg and M. O. Scully, "Efficient frequency up-conversion in resonant coherent media," Phys. Rev. A **65**, 051801 (2002).
13. T. Meijer, J. D. White, B. Smeets, M. Jeppesen, and R. E. Scholten, "Blue five-level frequency-upconversion system in rubidium," Opt. Lett. **31**, 1002–1004 (2006).

#128183 - $15.00 USD Received 10 May 2010; revised 11 Jun 2010; accepted 19 Jul 2010; published 27 Jul 2010

14. A. M. Akulshin, R. J. McLean, A. I. Sidorov, and P. Hannaford, "Coherent and collimated blue light generated by four-wave mixing in Rb vapour," Opt. Express **17**, 22861–22870 (2009).
15. Kurucz data, cfa-www.harvard.edu/amp/tools.html.
16. P. Siddons, C. S. Adams, C. Ge and I. G. Hughes, "Absolute absorption on rubidium D lines: comparison between theory and experiment," J. Phys. B **41**, 155004 (2008).
17. J. L. Hall, M. Zhu and P. Buch, "Prospects for using laser-prepared atomic fountains for optical frequency standards applications," J. Opt. Soc. Am. B **6**, 2194–2205 (1989).
18. G. Morigi, S. Franke-Arnold, and G.-L. Oppo, "Phase-dependent interaction in a four-level atomic configuration," Phys. Rev. A **66**, 053409 (2002).
19. S. Kajari-Schröder, G. Morigi, S. Franke-Arnold, and G.-L. Oppo, "Phase-dependent light propagation in atomic vapors," Phys. Rev. A **75**, 013816 (2007).
20. J. T. Schultz, S. Abend, D. Döring, J. E. Debs, P. A. Altin, J. D. White, N. P. Robins and J. D. Close, "Coherent 455nm beam production in cesium vapor," Opt. Lett. **34** 2321–2323 (2009).

Nonlinear optical processes can be greatly enhanced for quasi-resonant atomic and molecular systems, allowing phenomena like efficient frequency up-conversion, four-wave mixing, slow light or image storage to be studied at low light intensities. On resonance, absorption hinders the build-up of strong coherences; this can be counteracted by excitation via two-photon resonances and in particular by using electromagnetically induced transparency (EIT). Here we report the generation of 1.1 mW of 420 nm blue light by enhanced frequency up-conversion in a hot rubidium vapor. This is made possible by long lived two-photon coherences at frequencies that allow propagation under phase-matching conditions. Depending on the polarization of the pump lasers, up-conversion can be enhanced or almost completely suppressed.

Alkali metal vapors are versatile tools for spectroscopy and nonlinear optics in atomic physics and have long been used for studies of 2-photon spectroscopy [1, 2, 3], dispersion [4] and EIT [4, 5]. In both isotopes of rubidium, the $5S_{1/2} - 5P_{3/2}$ (780 nm) and $5P_{3/2} - 5D_{5/2}$ (776 nm) transitions (Fig. 1a) are easily accessible with simple diode laser systems [6]. The extremely strong dipole moment of the infrared $6P_{3/2} - 5D_{5/2}$ transition (Fig. 1b) means that two-photon pumping with 776 and 780 nm light facilitates three-photon coherence between ground state and the $6P_{3/2}$ level. Excitation and decay via other levels ($5P_{1/2}$, $6P_{1/2}$, $5D_{3/2}$) is excluded by large detuning and selection rules. Similar alkali metal transitions have proven ideal for studies of amplified spontaneous emission versus four-wave mixing [7, 8], superfluorescence [11], multi-photon ionization processes [8], and sensitive atomic imaging [9, 10].

Recent papers [12, 13, 14] have reported the generation of tens of μWatts of coherent 420 nm blue light by pumping the Rb 5S−5P−5D transition. In our experiment we obtained

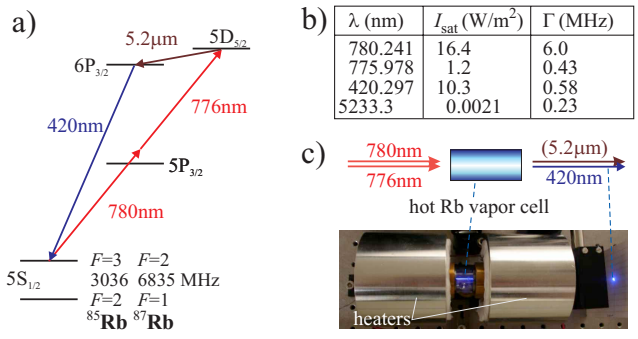

Fig. 1. a) The Rb energy level scheme. b) Relevant Rb transition parameters [15]. c) Experimental image showing how co-propagating focussed 780 and 776 nm laser beams create a coherent 420 nm (and invisible 5.2 μm) beam.

#128183 - $15.00 USD Received 10 May 2010; revised 11 Jun 2010; accepted 19 Jul 2010; published 27 Jul 2010

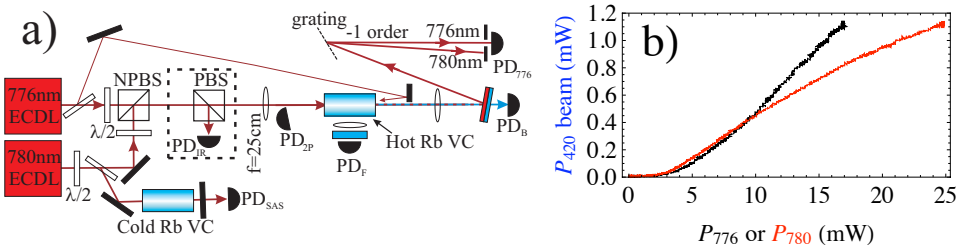

Fig. 2. a) Experimental schematic, abbreviations used are: PD (photodiode), VC (vapor cell) N/PBS (non/polarizing beamsplitter) and ECDL (external cavity diode laser). b) Power in the coherent 420 nm beam as a function of 780 nm (red) and 776 nm (black) input power. For each trace the power of the other input beam was maximal and detunings and polarization were optimized, see text.

up to 1.1 mW of coherent blue light for similar input pump powers. We have studied and optimized blue light generation for a variety of experimental parameters, namely input beam polarization and frequency, and Rb vapor pressure. In our system we have measured a maximum of 1.1 mW of coherent blue light close to two-photon resonance of the input lasers at $\Delta_{780} = -\Delta_{776} \cong 1.6$ GHz. Optimal conditions include a Rb vapor pressure of 10^{-3} mbar and co-circularly polarized input beams at maximum available powers of 17 mW at 776 nm and 25 mW at 780 nm. This corresponds to a conversion efficiency of $\eta = P_{420}/(P_{776}P_{780}) \sim 260\%/\mathrm{W}$.

The essence of the experimental setup is shown in Fig. 1c), with a more detailed view in Fig. 2a). Laser beams from Faraday-isolated 776 nm and 780 nm extended-cavity diode lasers are overlapped on a non-polarizing beamsplitter and focussed into a 75 mm long Rb vapor cell. The pump beams have maximum powers of 17 mW and 25 mW respectively which for elliptical beams with waists of 0.6 mm × 1.1 mm yield an estimated focal intensity of $\approx 2 \times 10^6$ W/m^2 each. Note that the 780 nm beam area after the cell varies with frequency, differing by more than an order of magnitude due to Kerr lensing.

We have measured the conversion efficiency as a function of the 776 and 780 nm input power (Fig. 2b), with all other parameters fixed at their optimum values stated above. We note that conversion efficiency depends on the Rabi frequencies and detunings of the pump beams, so that for low pump powers the chosen detunings are not ideal. The pump power was varied by rotating half wave plates in the individual input beams, and monitored via the polarizing beamsplitter (PBS) shown in the dashed region of Fig. 2a). Although the blue light begins to saturate with 780 nm input power, it is linear in 776 nm input power in the regions accessible by our diode lasers, promising a further increase in blue light power for stronger 776 nm pumping.

The atomic density and associated vapor temperature were measured to high resolution via absorption spectroscopy of a low power (5 μW) 780 nm probe beam [16]. This avoided any inaccuracy due to the inhomogeneity of the external cell temperature. For our setup optimal blue light generation occurs at a temperature of 120 ± 1°C, corresponding to a Rb vapor pressure of 9×10^{-4} mbar, nearly 4 orders of magnitude higher than at room temperature. While higher temperatures, and therefore atomic densities, facilitate the nonlinear up-conversion process, they also increase absorption of the pump and output beams. Overall, the system is fairly robust: more than half of the maximum blue beam efficiency could be achieved over a temperature range of $104 - 131$°C corresponding to a factor of 5 in Rb pressure, and focussing the near-infrared light from 0.4 to 4 times the optimal free-space focal intensity yielded similar ($> 75\%$ of optimal) conversion efficiency.

In order to investigate the up-conversion process we have measured fluorescent and coherent blue light generation over a wide range of input beam frequencies, see Fig. 3c)-f). Data was

#128183 - $15.00 USD Received 10 May 2010; revised 11 Jun 2010; accepted 19 Jul 2010; published 27 Jul 2010

taken for low and high Rb temperatures of 90°C and 120°C respectively, corresponding to vapor pressures of 1×10^{-4} mbar and 9×10^{-4} mbar. The frequency of the 780 nm beam was measured via saturated absorption spectroscopy in a room temperature Rb cell, and that of the 776 nm beam by monitoring the two-photon absorption of a weak 776 nm probe beam counter-propagating through the hot cell (Fig. 2a).

We have modeled fluorescence and coherent light generation (Fig. 3a) and b) from optical Bloch equations for the 5 atomic levels, using a similar model to Ref. [13], evaluated with Doppler broadening (FWHM$\sim$ 580 MHz for the 776 and 780 nm light at $\sim$ 100°C) and for Rabi frequencies ($\Omega_{780} = 1.4$ GHz, $\Omega_{776} = 0.4$ GHz, $\Omega_{IR} = 30$ MHz, $\Omega_{420} = 20$ MHz) similar to the estimated experimental focal values in the low pressure cell. The model does not explicitly include propagation, and neglects the hyperfine structure of the upper states. Nevertheless, numerical solutions for the steady state of the optical Bloch equations allowed us to interpret many of the observed features. Fluorescence (top row of Fig. 3) arises from a transfer of population to the 5D level and subsequent fast decay to the 6P level. Our model shows that this happens mainly when the system is pumped at two-photon resonance between the Stark-shifted atomic levels, and to a lesser extent, for resonant driving of the 776 nm transition. The model (Fig. 3a) describes the observed fluorescence well (Figs. 3c and e), even though it does not account for propagation effects or 780 nm pump Kerr lensing which increase at higher temperature.

The generation of coherent blue light requires coherences between the ground state 5S hy-

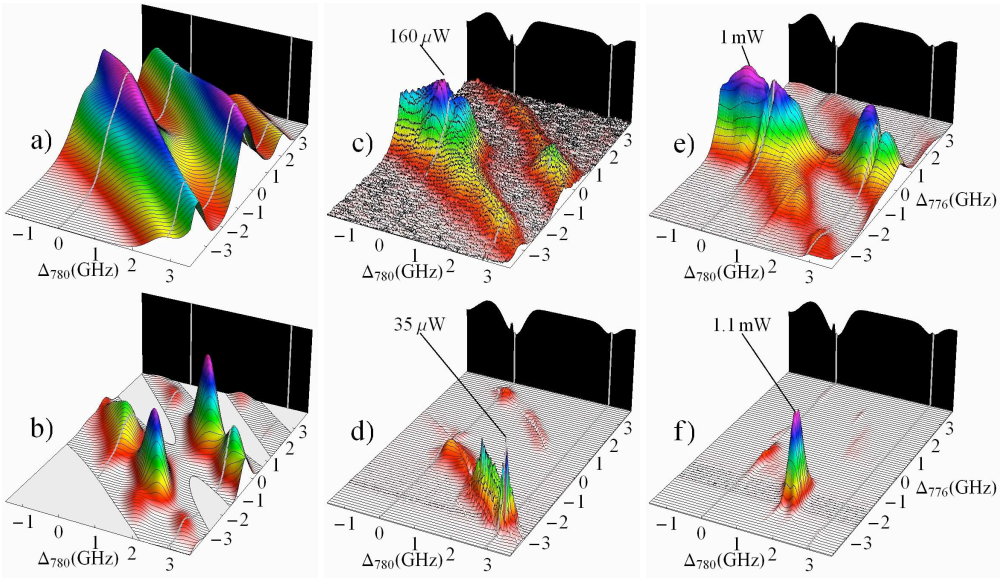

Fig. 3. Relative blue fluorescence (top row) and blue beam (bottom row) power as a function of 780 and 776 nm light detuning. Theoretical simulations of the 5-level Bloch equations are shown in a) and b). Graph a) shows the Doppler-broadened population in the 6P level corresponding to blue fluorescence. Fig. b) shows the Doppler-broadened coherences between ground and the 6P level, corresponding to coherent blue light generation. The blue coherences are adjusted to account for Kerr lensing and absorption of the 780 nm pump beam. Graphs c) and d) show measurements at a cell temperature of 90°C, and e) and f) at 120°C. At low pressure, coherent light is generated over a range of detunings at two-photon resonance. At high pressure Kerr-lensing of the pump beams and phase-matching become more pronounced, restricting blue light generation to a narrow frequency window. The backdrops show 780 nm saturated absorption in a cold cell.

#128183 - $15.00 USD Received 10 May 2010; revised 11 Jun 2010; accepted 19 Jul 2010; published 27 Jul 2010

perfine levels and the 6P level. While the detuning of the blue (and IR) light is experimentally unknown, our simulations suggest that coherent blue light conversion occurs at three-photon resonance. For the (relatively) small blue light and IR intensities in the experiment the 6P level is unshifted, so three-photon resonance coincides with two-photon resonance. Phase-matching is a prerequisite of efficient coherent light generation. Our model shows that phase-matching $\Delta k = n_{780}k_{780} + n_{776}k_{776} - n_{IR}k_{IR} - n_{420}k_{420} \approx 0$ is satisfied along most of the three-photon resonances. We model blue light generation (Fig. 3b) as Doppler-broadened coherences adjusted to account for Kerr lensing and absorption of the 780 nm pump beam. This is an approximation to a full analysis which would require the study of field and density matrix propagation for non-collinear beams. At lower vapor pressure, we observe coherent blue light over a range of detunings near two-photon resonance (Fig. 3d), reminiscent of observations in Ref. [13, 14]. Strikingly, when the Rb pressure in the cell is high, the experiment shows an increase of blue beam generation by 1.5 orders of magnitude, however only over a restricted range of input detunings (Fig. 3f), with highest conversion efficiency for two-photon (and three-photon) resonance at $\Delta_{780} = -\Delta_{776} = 1.6$ GHz. We attribute the suppression of blue light generation outside this region to Kerr-lensing of the 780 nm input beam. Furthermore, absorption of 780 nm light contributes to the absence of light generation from the ^{87}Rb isotope.

A scan (Fig. 4) of the 780 nm input frequency, keeping the 776 nm detuning constant at the optimized value of $\Delta_{776} = -1.6$ GHz, shows clearly the strong frequency dependence of fluorescence and blue light generation. The theoretical model (Fig. 4a) of blue fluorescence accompanied by 776 nm absorption agrees well with the experiment (Fig. 4c). Coherences on the 420 nm transition between the 5S level and 6P level are present at two-photon resonance for the two hyperfine ground levels of ^{85}Rb and ^{87}Rb, and mark out four frequency regions of potential blue light generation, Fig. 4b). Kerr-lensing depletes and deflects the 780 nm pump laser at three of these resonances, so that only the coherence at $\Delta_{780} = 1.6$ GHz survives. The same

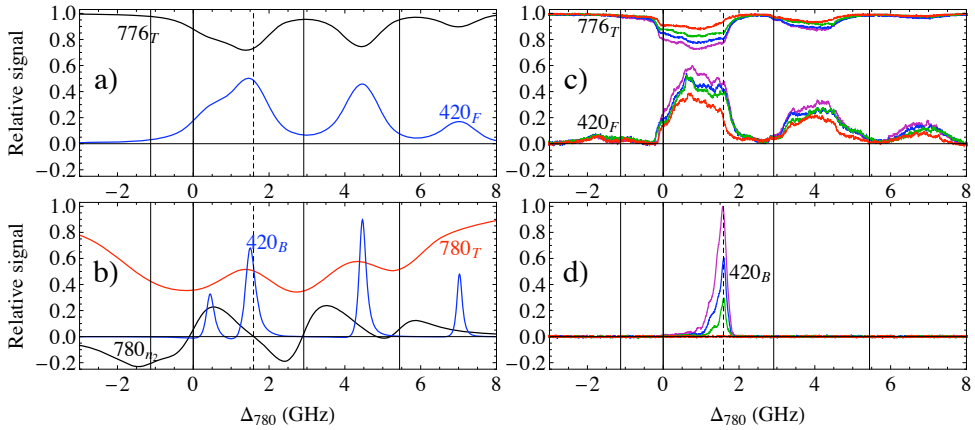

Fig. 4. Coherent and fluorescent blue light as a function of Δ_{780} for $\Delta_{776} = -1.6$ GHz. Graph a) shows theoretical blue fluorescence (420_{F}, blue) as well as transmission of the 776 nm (776_{T}, black) pump beam, including Doppler-broadening. Graph b) shows the blue beam coherences (420_{B}, blue), as well as the Doppler-broadened theoretical transmission (780_{T}, red) and Kerr-lensing ($780_{n_2} \propto \Delta n_{780}/\Delta I_{780}$ intensity-dependent refraction, black) of the 780 nm beam, which favors the coherence at 1.6 GHz. Measurements of blue fluorescence accompanied by 776 nm absorption c), and blue beam generation d) are shown for different input polarizations: counter-circular (red), crossed-linear (green), co-linear (blue) and co-circular (purple). Vertical lines indicate ^{85}Rb and ^{87}Rb 780 nm resonances.

#128183 - $15.00 USD Received 10 May 2010; revised 11 Jun 2010; accepted 19 Jul 2010; published 27 Jul 2010

detuning also exhibits a local minimum of absorption of the 780 nm input laser. We note that Kerr lensing will change beam direction and hence also modify the phase-matching condition. Increasing the atomic density and hence the optical path length, makes propagation effects and phase-matching more critical and adds further complexity as more 5 μm and 420 nm fields are generated. Experimentally, the strongest blue light generation was observed near a minimum of lensing for the 780 nm beam, Fig. 4d).

We finally report the crucial effect of input polarization on blue light generation, shown in Fig. 4c) and d). For these experiments the PBS in the dashed region of Fig. 2a) had to be removed. We simultaneously monitored the blue beam power (PD_B), the blue fluorescence in the cell (PD_F), absorption of the 776 nm beam (PD_{776}), and the detuning of the 780 nm laser (PD_{SAS}). Measurements were taken for four different relative input polarizations of the 776 nm and 780 nm input beams: co-linear, crossed-linear, co-circular and counter-circular. Care was taken to compensate for grating polarization-dependence in the 776 nm pump beam measured at PD_{776}. By analyzing the 776 nm laser absorption (Fig. 4c), we can estimate that it is possible to create a coherent 420 nm photon for every six 776 nm photons absorbed. Note that the blue beam generation is suppressed by a factor of 500 when counter-circular polarization is used, although there is still a similar amount of blue fluorescence and 776 nm beam absorption, indicating that the transfer of population to levels $5D_{5/2}$ and $6P_{3/2}$ is not forbidden by two- and three-photon absorption selection rules. This implies that the excitation of three-photon coherences between the $5S_{1/2}$ ground state and the $6P_{3/2}$ state depend crucially on polarization. Optical pumping favors blue light generation for the case of co-circularly polarized pump beams, however, the inhibition of blue light generation for counter-circular polarization suggests an interference effect. This may be attributed to a cancelation of the coherences due to the phase of the atomic dipoles. One can envisage that this property will be useful for applications in optical switching, where flipping 780 nm (or 776 nm)pump polarization would switch the blue beam power.

As our system is not saturating with pump power, increasing the pump power or using a build-up cavity could generate tens of mW of blue light. By accessing higher lying $D_{5/2}$ levels one should be able to generate similar powers at UV wavelengths by transitions via the corresponding $P_{3/2}$ levels. It is interesting to consider the application of such light sources for laser cooling where the narrower linewidth on these blue/UV transitions will lead to much lower Doppler temperatures [17]. In initial experiments we have observed 420 nm linewidths of less than 8 MHz, at the resolution limit of our etalon. The scheme should generalize to all alkali metals, and has recently been realized in cesium [20].

In conclusion, we have observed a polarization-dependent factor of 26 increase in blue light conversion efficiency under comparable conditions to previous experiments. Our observations of the frequency-dependent characteristics of the 776 nm beam absorption, blue fluorescence and blue beam power show good agreement with our theoretical framework, particularly for low experimental temperatures, indicating the importance of three-photon resonance coinciding with vanishing susceptibility on the 780 nm transition. In the low Rb pressure regime with the weaker blue beam afforded by crossed-linear polarizations we observe similar experimental behavior (frequency dependence and conversion efficiency) as observed in Refs. [12, 13] and we attribute our increased efficiency to polarization enhancement as well as a higher apparent Rb vapor pressure. It is clear that propagation must be included for proper modeling of the system at high temperatures due to the strong absorption/refraction processes at work in the cell. There are still many open questions in this surprisingly rich atomic vapor system. We envisage future experiments in isotopically enhanced vapor cells (to simplify the system's absorption-emission characteristics) and sapphire vapor cells which will allow us access to the 'missing link' of the closed loop structure [18, 19], the 5.2 μm light.

#128183 - $15.00 USD Received 10 May 2010; revised 11 Jun 2010; accepted 19 Jul 2010; published 27 Jul 2010

Acknowledgements

Thanks to N. Paterson, S. Clark and N. Houston for experimental contributions. We gratefully acknowledge discussions with P. Siddons and I. G. Hughes. SFA is a RCUK Research Fellow.

#128183 - $15.00 USD Received 10 May 2010; revised 11 Jun 2010; accepted 19 Jul 2010; published 27 Jul 2010

Mathematica programme for "Blue light" simulations

This appendix contains all the useful information to reproduce the numerical results shown in Chapter 6 of this thesis.

Constants and Functions

```
Remove[g12, g13, g23, g34, g54, g15, g25, δ1, δ2, δ3, δ4, δ5, γ12, γ21, γ31, γ32, γ43, γ45,
  γ52, γ51, ϕ1, ϕ2, H, G, L, T, T5, RS, LS, LF, ρ, λ13, λ23, λ34, λ54, λ15, λ25, s];
```

Definition of the Hamiltonian and decay matrix

```
H[g13_, g23_, g34_, g54_, g25_, g15_, δ1_, δ2_, δ3_, δ4_, δ5_, ϕ1_, ϕ2_] :=
  {{δ1, 0, g13 / 2, 0, g15 / 2 * Exp[i * ϕ1]},
   {0, δ2, g23 / 2, 0, g25 / 2 * Exp[i * ϕ2]},
   {g13 / 2, g23 / 2, δ3, g34 / 2 , 0},
   {0, 0, g34 / 2 , δ4, g54 / 2},
   {g15 / 2 * Exp[-i * ϕ1], g25 / 2 * Exp[-i * ϕ2], 0, g54 / 2, δ5}}; (* Hamiltonian,
gij: Rabi frequencies, ϕ1, ϕ2 phases associated to the two closed loops as described in Chapter *)

G[γ12_, γ21_, γ31_, γ32_, γ43_, γ45_, γ52_, γ51_] :=
  -DiagonalMatrix[{γ12, γ21, γ31 + γ32, γ43 + γ45, γ52 + γ51}] / 2; (* Decay *)


H[g13, g23, g34, g54, g25, g15, δ1, δ2, δ3, δ4, δ5, ϕ1, ϕ2] // MatrixForm
G[γ12, γ21, γ31, γ32, γ43, γ45, γ52, γ51] // MatrixForm
```

$$\begin{pmatrix} \delta 1 & 0 & \frac{g13}{2} & 0 & \frac{1}{2} e^{i \phi 1} g15 \\ 0 & \delta 2 & \frac{g23}{2} & 0 & \frac{1}{2} e^{i \phi 2} g25 \\ \frac{g13}{2} & \frac{g23}{2} & \delta 3 & \frac{g34}{2} & 0 \\ 0 & 0 & \frac{g34}{2} & \delta 4 & \frac{g54}{2} \\ \frac{1}{2} e^{-i \phi 1} g15 & \frac{1}{2} e^{-i \phi 2} g25 & 0 & \frac{g54}{2} & \delta 5 \end{pmatrix}$$

$$\begin{pmatrix} -\frac{\gamma 12}{2} & 0 & 0 & 0 & 0 \\ 0 & -\frac{\gamma 21}{2} & 0 & 0 & 0 \\ 0 & 0 & \frac{1}{2}(-\gamma 31 - \gamma 32) & 0 & 0 \\ 0 & 0 & 0 & \frac{1}{2}(-\gamma 43 - \gamma 45) & 0 \\ 0 & 0 & 0 & 0 & \frac{1}{2}(-\gamma 51 - \gamma 52) \end{pmatrix}$$

Convert $\frac{d\rho}{dt} = [H, \rho] + \mathcal{L}\rho$ into form $\frac{d\rho}{dt} = L\rho$ for evaluation with Mathematica

```
T = ReplacePart[Table[0, {25}], 1, {{1}, {7}, {13}, {19}, {25}}];  (* ρij *)
T5 = ReplacePart[Table[0, {25}], 1, {{25}}];   (* Conservation of Trace Σρjj=1 *)

L = Table[0, {25}, {25}];

Do[
  a = 5 (i - 1) + j;
  b = 5 (k - 1) + j;
  d = 5 (i - 1) + k;
  L[[a, a]] += (G[γ12, γ21, γ31, γ32, γ43, γ45, γ52, γ51][[i, i]] +
      G[γ12, γ21, γ31, γ32, γ43, γ45, γ52, γ51][[j, j]]) / 5;
  L[[a, b]] += -I H[g13, g23, g34, g54, g25, g15, δ1, δ2, δ3, δ4, δ5, ϕ1, ϕ2][[i, k]];
  L[[a, d]] += I H[g13, g23, g34, g54, g25, g15, δ1, δ2, δ3, δ4, δ5, ϕ1, ϕ2][[k, j]],
  {j, 5}, {i, 5}, {k, 5}]; (*Generate L matrix from Hamiltonian and decay matrix*)

L[[7, 1]] += γ12; L[[1, 7]] += γ21;
L[[1, 13]] += γ31;                                   (* Manual input of decays *)
L[[7, 13]] += γ32; L[[13, 19]] += γ43; L[[25, 19]] += γ45; L[[7, 25]] += γ52; L[[1, 25]] += γ51;

LF[g13_, g23_, g34_, g54_, g25_, g15_, δ1_, δ2_, δ3_, δ4_, δ5_,
   γ12_, γ21_, γ31_, γ32_, γ43_, γ45_, γ52_, γ51_, ϕ1_, ϕ2_] := Evaluate[L];
```

Constants and useful functions

```
h = 6.62606896 * 10^-34;
c = 299 792 458;
ħ = 6.63 10^-34; ϵ = 8.85 10^-12;
Sat[λ_, Γ_] := 2 π^2 h c Γ / (3 λ^3); (*Saturation Intensity*)
Rabi[s_, Γ_] := Sqrt[2 s (Γ^2 / 4)] ; (*Rabi Frequency*)
```

Physical variables and parameter values

```
Clear[S, P780, P776, γ31, γ32, γ43, γ42, γ41, λ13, λ23, λ34, i13, i23, i34, s13, s23,
 s34, ω13, ω23, ω34, f, Γ31, Γ32, Γ43, Γ42, Γ41, Ω13, Ω23, Ω34]; S = π (60 * 10^-6)^2;
(*area of beam @ focus, compare with intensity at focus 2 10^6 W/m^2 for P=20mW*)
P780 = 20 * 10^-3; (*power of 780 beam, SI*)
P776 = 20 * 10^-3;(*power of 776 beam, SI*)
Pblue = 10^-3; (*measured power of blue light*)

γ12 = 10^7; γ21 = 10^7;
γ31 = 5.976 * 10^6;(*Decays, 780 5.976MHz, 776: 431kHz, 1-5: 583kHz, 5mu: 233kHz ?*)
γ32 = 5.976 * 10^6;
γ43 = 4.315 * 10^5;
γ45 = 2.33 * 10^5;
γ51 = 5.83 * 10^5;
γ52 = 5.83 * 10^5;

λ13 = 780.2414 * 10^-9;(*transition wavelengths*)
λ23 = 780.2414 * 10^-9;
λ34 = 775.97855 * 10^-9;
λ45 = 5.233 * 10^-6;
λ51 = 420.2976 * 10^-9;
λ52 = 420.2976 * 10^-9;

{i13 = P780/S, i23 = P780/S, i34 = P776/S, i45 = λ51/λ45 Pblue/S, i51 = Pblue/S, i52 = Pblue/S};
(*intensities*)
{s13 = i13/Sat[λ13, γ31], s23 = i23/Sat[λ23, γ32], s34 = i34/Sat[λ34, γ43], s45 = i45/Sat[λ45, γ45],
  s51 = i51/Sat[λ51, γ51], s52 = i52/Sat[λ52, γ52]}; (*saturation parameters*)
{ω13 = Rabi[s13, γ31], ω23 = Rabi[s23, γ32], ω34 = Rabi[s34, γ43], ω45 = Rabi[s45, γ45],
  ω51 = Rabi[s51, γ51], ω52 = Rabi[s52, γ52]};(*Rabi frequencies*)
f = 10^9;                          (*Conversion of frequencies to GHz*)
Γ12 = γ12/f; Γ21 = γ21/f; Γ31 = γ31/f; Γ32 = γ32/f; Γ43 = γ43/f;
Γ45 = γ45/f; Γ52 = γ52/f; Γ51 = γ51/f; Γ12 = γ12/f; (*Decays in GHz*)
{Ω13 = ω13/f, Ω23 = ω23/f, Ω34 = ω34/f, Ω54 = ω45/f, Ω25 = ω52/f, Ω15 = ω51/f};
(*Rabi frequencies in GHz*)
Cl = 1/Sqrt[(10+35+81)/81] {Sqrt[(27 + 35 + 28)/81], Sqrt[(10 + 35 + 81)/81], Sqrt[(2 + 5 + 5)/18], Sqrt[(1 + 5 + 14)/18]};

(*85Rb lower ground,85Rb upper ground,87Rb lower ground,87
Rb upper ground Clebsch-Gordan coefficients*)
```

1 D Figures

Evaluation of density matrix

```
(*Evaluate this cell*)
Clear[LS85, LS87, RSteady87, RSteady85,
  RSteady, δ780, δ776, δIR, v, LS87, RSteady87, LS85, RSteady85];
ab87 = .28; ab85 = 1 - ab87;
LS85[δ780_, δ776_, δIR_, f1_, f2_, f3_, ϕ_] :=
  Transpose[Append[Transpose[ReplacePart[LF[Cl[[1]] f1 Ω13, Cl[[2]] f1 Ω23 ,
       f2 Ω34, f3 Ω54, Cl[[1]] f3 Ω15, Cl[[2]] f3 Ω25, -2.915, 0, -δ780, -δ776 - δ780,
       (-δ776 - δ780 + δIR), Γ12, Γ21, Γ31, Γ32, Γ43, Γ45, Γ52, Γ51, 0, ϕ], T, {25}]], T5]];
LS87[δ780_, δ776_, δIR_, f1_, f2_, f3_, ϕ_] :=
  Transpose[
   Append[Transpose[ReplacePart[LF[Cl[[3]] f1 Ω13, Cl[[4]] f1 Ω23 , f2 Ω34, f3 Ω54, Cl[[3]] f3 Ω15,
       Cl[[4]] f3 Ω25, -5.44, 1.1, -δ780, -δ776 - δ780, -δ776 - δ780 + δIR,
       Γ12, Γ21, Γ31, Γ32, Γ43, Γ45, Γ52, Γ51, 0, ϕ], T, {25}]], T5]];
RSteady85[δ780_, δ776_, v_] := RowReduce[LS85[δ780, δ776, v[[1]], v[[2]], v[[3]], v[[4]], v[[5]]][[
   Range[1, 25], 26]];
RSteady87[δ780_, δ776_, v_] := RowReduce[LS87[δ780, δ776, v[[1]], v[[2]], v[[3]], v[[4]], v[[5]]][[
   Range[1, 25], 26]];
RSteady[δ780_, δ776_, v_] := ab85 RSteady85[δ780, δ776, v] + ab87 RSteady87[δ780, δ776, v]
(*v is vector for δIR, f1,f2,f3,ϕ*)
v = {0, .4, .4, .001, 0};(*v is a function of : IR detuning,
780 strength, 776 strength and Blue/IR strength*)


steps = 500; dd780min = -3; dd780max = 8; fnn = 1; scll = 3;
f780 = (dd780max - dd780min)/(steps - 1);
v780 = Table[{Round[(i - dd780min) / f780 + 1], i}, {i, Ceiling[dd780min], Floor[dd780max]}];

δ776 = -1.7;
tab851D = Transpose[
   Table[RSteady85[i, δ776, v], {i, dd780min, dd780max, (dd780max - dd780min)/(steps - 1)}], {2, 1}];
tab871D = Transpose[Table[RSteady87[i, δ776, v],
    {i, dd780min, dd780max, (dd780max - dd780min)/(steps - 1)}], {2, 1}];
```

- **Phase - Matching : See Equation (5.5)**
  atomic density : $.3\ 10^{-13}$ atoms / cm^3

```
PM851D = .3 10^13 10^6 10^-4 (Re[(ħ v[[2]] Ω13 10^9)/(ϵ i13) (2 π)/λ13 (Cl[[1]] tab851D[[3]] + Cl[[2]] tab851D[[8]]) +
    (ħ Ω34 v[[3]] 10^9)/(ϵ i34) (2 π)/λ34 tab851D[[14]] - (ħ v[[4]] Ω15 10^9)/(ϵ i51) (2 π)/λ51
     (Cl[[1]] tab851D[[5]] + Cl[[2]] tab851D[[10]]) - (ħ v[[4]] Ω54 10^9)/(ϵ i45) (2 π)/λ45 tab851D[[24]]]);
PM871D = .3 10^13 10^6 10^-4 (Re[(ħ v[[2]] Ω13 10^9)/(ϵ i13) (2 π)/λ13 (Cl[[1]] tab871D[[3]] + Cl[[2]] tab871D[[8]]) +
    (ħ Ω34 v[[3]] 10^9)/(ϵ i34) (2 π)/λ34 tab871D[[14]] - (ħ v[[4]] Ω15 10^9)/(ϵ i51) (2 π)/λ51
     (Cl[[1]] tab871D[[5]] + Cl[[2]] tab871D[[10]]) - (ħ v[[4]] Ω54 10^9)/(ϵ i45) (2 π)/λ45 tab871D[[24]]]);
```

Including Doppler

- **Doppler averaging routine**

```
νD = 1/780 Sqrt[(1.38 10^-23 373)/(85 × 1.66 10^-27)] ; (*Doppler width*)
steps780 = steps; d780min1 = dd780min; d780max1 = dd780max;
f780 = (d780max1 - d780min1)/(steps - 1) // N;
ssep = Round[3 νD / f780]; {f780, νD, ssep, Exp[-(ssep f780)^2 / (2 νD^2)], ssep f780};
Dopp1D[M_] := Sum[Exp[-(i f780)^2/(2 νD^2)] RotateLeft[M, i], {i, -ssep, ssep}];
(*Doppler averaging*)
par1D[M_] := M[[Range[ssep + 1, steps780 + ssep]]](*For removing extra Doppler
 part (incorrect on edges due to Rotate matrix commands) when plotting*)
νν780 = Table[i, {i, d780min1, d780max1, f780}];

Dopptaba = Table[Dopp1D[tab851D[[dim]]], {dim, 1, 25}];
Dopptab2a = Table[Dopp1D[tab871D[[dim]]], {dim, 1, 25}];
norm1D = Max[Re[Dopptaba[[1]] + Dopptaba[[7]] + Dopptaba[[13]] + Dopptaba[[19]] + Dopptaba[[25]]]];
```

■ Phase - matching

```
DoppPM851D =
  .3 10^13 10^6 10^-4 / norm1D (Re[ħ v[[2]] Ω13 10^9 / (ϵ i13) 2π/λ13 (Cl[[1]] Dopptaba[[3]] + Cl[[2]] Dopptaba[[8]]) + ħ Ω34 v[[3]] 10^9 / (ϵ i34)
    2π/λ34 Dopptaba[[14]] - ħ v[[4]] Ω15 10^9 / (ϵ i51) 2π/λ51 (Cl[[1]] Dopptaba[[5]] + Cl[[2]] Dopptaba[[10]]) -
    ħ v[[4]] Ω54 10^9 / (ϵ i45) 2π/λ45 Dopptaba[[24]]]);(*Phase-Matching on first loop*)
DoppPM871D = .3 10^13 10^6 10^-4 / norm1D (Re[ħ v[[2]] Ω13 10^9 / (ϵ i13) 2π/λ13 (Cl[[1]] Dopptab2a[[3]] + Cl[[2]] Dopptab2a[[8]]) +
    ħ Ω34 v[[3]] 10^9 / (ϵ i34) 2π/λ34 Dopptab2a[[14]] -
    ħ v[[4]] Ω15 10^9 / (ϵ i51) 2π/λ51 (Cl[[1]] Dopptab2a[[5]] + Cl[[2]] Dopptab2a[[10]]) -
    ħ v[[4]] Ω54 10^9 / (ϵ i45) 2π/λ45 Dopptab2a[[24]]]); (*Phase-matching on second loop*)

DoppPMT1D85 = Im[Dopptaba[[5]] + Dopptaba[[10]]]^2 ab85 Sinc[DoppPM851D]^2;
DoppPMT1D87 = Im[Dopptab2a[[5]] + Dopptab2a[[10]]]^2 ab87 Sinc[DoppPM871D]^2;
DoppPMT1DT = DoppPMT1D85 + DoppPMT1D87;
```

■ Plotting options and plots

```
scll = 1.8
SetOptions[ListPlot, Joined → True, AspectRatio → 1 / 2.5,
  Frame → True, BaseStyle → {FontFamily → Times, FontSize → scll 10},
  FrameLabel → {"Detuning (GHz)", "Relative signal"},
  FrameTicks → Automatic, ImageSize → scll 300, Axes → True];
fv = Table[i, {i, dd780min, dd780max, (dd780max - dd780min)/(steps - 1)}];
gg[v1_] := Transpose[{fv, v1}]; M = Max[DoppPMT1DT];
DoppFiga = ListPlot[gg /@ {DoppPMT1DT/M}, PlotStyle → Map[{Thick, #} &,
    {Darker[Blue], Black, Green, Blue, Red, Orange, GrayLevel[0.5], Yellow}],
  Joined → True,  PlotRange → {All, {-.2, 1.1}},
  Epilog → {Inset[Style["Blue light generation", scll 10, Darker[Blue]], {0, 0.1}]}]
DoppFigb = ListPlot[gg /@ {10/norm1D Chop[Dopptaba[[25]] + Dopptab2a[[25]],
    1 - 25 Im[Dopptaba[[14]] + Dopptab2a[[14]]]},
  PlotStyle → Map[{Thick, #} &, {Darker[Blue], Darker[Darker[Green]], Green, Blue,
    Red, Orange, GrayLevel[0.5], Yellow}], Joined → True,  PlotRange → {All, {-.2, 1}},
  Epilog → {Inset[Style["Absorption", scll 10, Darker[Darker[Green]]], {0, 0.7}],
    Inset[Style["Fluorescence", scll 10, Darker[Darker[Blue]]], {0, 0.2}]}]
```

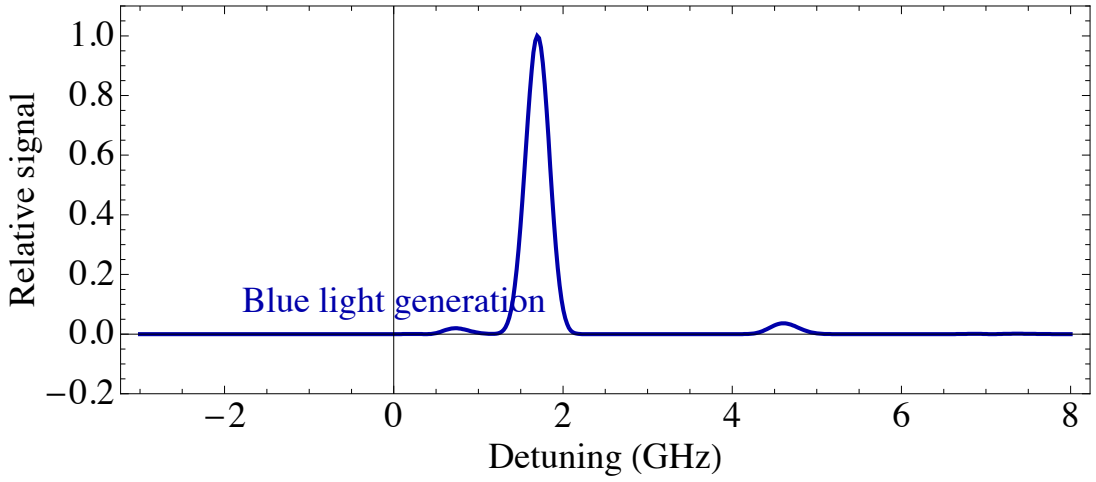

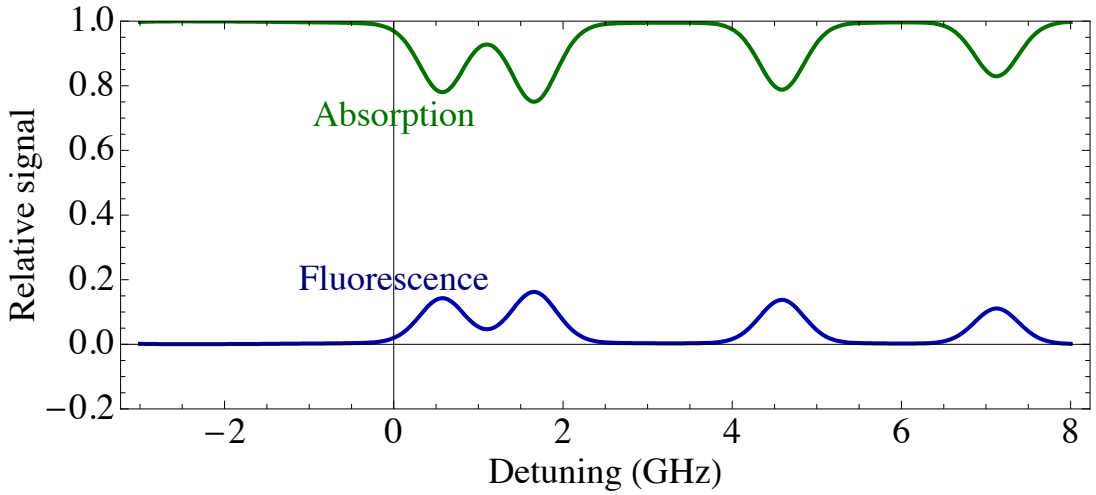

2 D Figures

■ Evaluation of density matrix

```
Clear[LS85, LS87, RSteady87, RSteady85, RSteady, δ780, δ776, δIR, v, tab,
  asp, scl776, steps780, steps776, d776max1, d776min1, d780max1, d780min1];
ab87 = .28; ab85 = 1 - ab87;
Clear[LS87, RSteady87, LS85, RSteady85];
LS85[δ780_, δ776_, δIR_, f1_, f2_, f3_, ϕ_] :=
  Transpose[Append[Transpose[ReplacePart[LF[Cl[[1]] f1 Ω13, Cl[[2]] f1 Ω23 ,
       f2 Ω34, f3 Ω54, Cl[[1]] f3 Ω15, Cl[[2]] f3 Ω25, -2.915, 0, -δ780, -δ776 - δ780,
       (-δ776 - δ780 + δIR), Γ12, Γ21, Γ31, Γ32, Γ43, Γ45, Γ52, Γ51, 0, ϕ], T, {25}]], T5]];
LS87[δ780_, δ776_, δIR_, f1_, f2_, f3_, ϕ_] :=
  Transpose[
   Append[Transpose[ReplacePart[LF[Cl[[3]] f1 Ω13, Cl[[4]] f1 Ω23 , f2 Ω34, f3 Ω54, Cl[[3]] f3 Ω15,
       Cl[[4]] f3 Ω25, -5.44, 1.1, -δ780, -δ776 - δ780, -δ776 - δ780 + δIR,
       Γ12, Γ21, Γ31, Γ32, Γ43, Γ45, Γ52, Γ51, 0, ϕ], T, {25}]], T5]];
RSteady85[δ780_, δ776_, v_] := RowReduce[LS85[δ780, δ776, v[[1]], v[[2]], v[[3]], v[[4]], v[[5]]][[
   Range[1, 25], 26]];
RSteady87[δ780_, δ776_, v_] := RowReduce[LS87[δ780, δ776, v[[1]], v[[2]], v[[3]], v[[4]], v[[5]]][[
   Range[1, 25], 26]];
RSteady[δ780_, δ776_, v_] := ab85 RSteady85[δ780, δ776, v] + ab87 RSteady87[δ780, δ776, v]
(*v is vector for δIR, f1,f2,f3,ϕ*)
```

■ Doppler averaging

```
νD = 1/780 Sqrt[1.38 10^-23 373 / (85 × 1.66 10^-27)];
asp = 75 / (.051 × 976);
scl776 = 4; steps776 = scl776 75; steps780 = Round[steps776 / asp]; {steps780, steps776};
d780min1 = -1.5; d780max1 = 3.5; (*Region of interest*)
d776min1 = -3.9; d776max1 = 3.9;
f780 = (d780max1 - d780min1)/(steps780 - 1); f776 = (d776max1 - d776min1)/(steps776 - 1);
ssep = Round[3 νD / f780]; {f780, f776, νD, ssep, Exp[-(ssep f780)^2 / (2 νD^2)], ssep f780};
d780min = -1.5 - ssep f780; d780max = 3.5 + ssep f780; (*Increase extra
 rows/columns (number of steps ssep) around the matrix for Doppler averaging*)
d776min = -3.9 - ssep f776; d776max = 3.9 + ssep f776;
cmin = .1; g[x_] := If[x < cmin, RGBColor[1, 1 - x/cmin, 1 - x/cmin], Hue[.9 (x - cmin)/(1 - cmin)]];
SetOptions[ListDensityPlot, AspectRatio → (d776max1 - d776min1)/(d780max1 - d780min1),
  BaseStyle → {FontSize → 20, FontFamily → "Times"},
  Mesh → False, DisplayFunction → Identity, ColorFunction → g,
  FrameLabel → {"Δ780 (GHz)", "Δ776 (GHz)"}, FrameTicks → Automatic, PlotLabel → None];
SetOptions[ListPlot3D, BoxRatios → {2, 2 (d776max - d776min)/(d780max - d780min), 1},
  BaseStyle → {FontSize → 20, FontFamily → "Times"},
  Mesh → False, DisplayFunction → Identity, ColorFunction → g,
  AxesLabel → {"Δ780 (GHz)", "Δ776 (GHz)", ""}, Ticks → Automatic, PlotLabel → None];
νν776 = Table[i, {i, d776min1, d776max1, f776}];
νν780 = Table[i, {i, d780min1, d780max1, f780}];
M780 = Table[νν780, {i, d776min1, d776max1, f776}];
M776 = Transpose[Table[νν776, {i, d780min1, d780max1, f780}]];


jm = 1;
Doppav =
  Sum[Exp[-((i - j) f780)^2 - (i f776)^2 / (2 νD^2)], {i, -(ssep - jm), (ssep - jm)}, {j, -jm, 0, jm}];
DoppR[M_] := Sum[Exp[-((i - j) f780)^2 - (i f776)^2 / (2 νD^2)]
    Transpose[RotateLeft[Transpose[RotateLeft[M, i - j]], i]],
   {i, -(ssep - jm), (ssep - jm)}, {j, -jm, 0, jm}] / Doppav; (*Doppler averaging*)
par[M_] := M[[Range[ssep + 1, steps776 + ssep], Range[ssep + 1, steps780 + ssep]]];
(*For removing extra Doppler part
 (incorrect on edges due to Rotate matrix commands) when plotting*)
Lp[M_] := ListDensityPlot[Flatten[Transpose[{M780, M776, par[M]}, {3, 1, 2}], 1],
   PlotRange → {{d780min1, d780max1}, {d776min1, d776max1}, {0, Max[par[M]]}},
   Mesh → {{0, 1.6, 2.915}, {0, -1.8, -2.915}}];
Lp3[M_] := ListPlot3D[Flatten[Transpose[{M780, M776, par[M]}, {3, 1, 2}], 1],
   PlotRange → {{d780min1, d780max1}, {d776min1, d776max1}, {0, Max[par[M]]}}];
(*Note that for the plots the Flatten command Matrix →
 vector is used. This unfortunately makes the plots twice as slow,
but has the advantage that you can give x, y and z coordinates,
rather than just using z with row and column numbers*)
```

```
Clear[tab85, tab87, tabDopp85, tabDopp87,
  PM85, PM87, PM185, PM187, PM287, PM285, PM1, PM2, PMNew2, PM];

v = {0, .25, .25, .01, 0};
tab85 = Transpose[Table[RSteady85[i, j, v],
    {i, d780min, d780max, f780}, {j, d776min, d776max, f776}], {3, 2, 1}];
 (*Generate the full matrix, including the extra for Doppler*)
tab87 = Transpose[Table[RSteady87[i, j, v],
    {i, d780min, d780max, f780}, {j, d776min, d776max, f776}], {3, 2, 1}];
tabDopp85 = Table[DoppR[tab85[[dim]]], {dim, 1, 25}];
tabDopp87 = Table[DoppR[tab85[[dim]]], {dim, 1, 25}];
```

■ Phase - Matching : See Equation (5.5)

atomic density : $.3\ 10^{13}$ atoms / cm^3

conversion length : 2×10^{-4}

```
dens = 3 10^18 ; clength = 2 10^-4; (*Atomic density, conversion length*)

PM85 = dens clength (Re[ħ v[[2]] Ω13 10^9 / (ϵ i13 (Cl[[1]] + Cl[[2]])) 2π/λ13 (Cl[[1]] tabDopp85[[3]] + Cl[[2]] tabDopp85[[8]]) +
      ħ Ω34 v[[3]] 10^9 / (ϵ i34) 2π/λ34 tabDopp85[[14]] - ħ v[[4]] Ω15 10^9 / (ϵ i51 (Cl[[1]] + Cl[[2]])) 2π/λ51
       (Cl[[1]] tabDopp85[[5]] + Cl[[2]] tabDopp85[[10]]) - ħ v[[4]] Ω54 10^9 / (ϵ i45) 2π/λ45 tabDopp85[[24]]]);

PM87 = dens clength (Re[ħ v[[2]] Ω13 10^9 / (ϵ i13 (Cl[[3]] + Cl[[4]])) 2π/λ13 (Cl[[3]] tabDopp85[[3]] + Cl[[4]] tabDopp85[[8]]) +
      ħ Ω34 v[[3]] 10^9 / (ϵ i34) 2π/λ34 tabDopp85[[14]] - ħ v[[4]] Ω15 10^9 / (ϵ i51 (Cl[[3]] + Cl[[4]])) 2π/λ51
       (Cl[[3]] tabDopp85[[5]] + Cl[[4]] tabDopp85[[10]]) - ħ v[[4]] Ω54 10^9 / (ϵ i45) 2π/λ45 tabDopp85[[24]]]);

PM85T = Sinc[PM85]^2;
PM87T = Sinc[PM87]^2;
```

```
PMNew2 = GraphicsRow[{Lp[-PM85T ab85 Im[(tabDopp85[[5]] + tabDopp85[[10]])] -
      PM87T ab87 Im[(tabDopp87[[5]] + tabDopp87[[10]])]]}, ImageSize → 300]
```